

AD _____

Award Number: W81XWH-05-1-0041

TITLE: Prostate Dose Escalation by Innovative Inverse Planning-Driven IMRT

PRINCIPAL INVESTIGATOR: Lei Xing, Ph.D.

CONTRACTING ORGANIZATION: Stanford University
Stanford, CA 94305-5401

REPORT DATE: November 2005

TYPE OF REPORT: Annual

PREPARED FOR: U.S. Army Medical Research and Materiel Command
Fort Detrick, Maryland 21702-5012

DISTRIBUTION STATEMENT: Approved for Public Release;
Distribution Unlimited

The views, opinions and/or findings contained in this report are those of the author(s) and should not be construed as an official Department of the Army position, policy or decision unless so designated by other documentation.

20060503057

REPORT DOCUMENTATION PAGE

Form Approved
OMB No. 0704-0188

Public reporting burden for this collection of information is estimated to average 1 hour per response, including the time for reviewing instructions, searching existing data sources, gathering and maintaining the data needed, and completing and reviewing this collection of information. Send comments regarding this burden estimate or any other aspect of this collection of information, including suggestions for reducing this burden to Department of Defense, Washington Headquarters Services, Directorate for Information Operations and Reports (0704-0188), 1215 Jefferson Davis Highway, Suite 1204, Arlington, VA 22202-4302. Respondents should be aware that notwithstanding any other provision of law, no person shall be subject to any penalty for failing to comply with a collection of information if it does not display a currently valid OMB control number. **PLEASE DO NOT RETURN YOUR FORM TO THE ABOVE ADDRESS.**

1. REPORT DATE 01-11-2005		2. REPORT TYPE Annual		3. DATES COVERED 1 Nov 2004 – 31 Oct 2005	
4. TITLE AND SUBTITLE Prostate Dose Escalation by Innovative Inverse Planning-Driven IMRT				5a. CONTRACT NUMBER	
				5b. GRANT NUMBER W81XWH-05-1-0041	
				5c. PROGRAM ELEMENT NUMBER	
6. AUTHOR(S) Lei Xing, Ph.D.				5d. PROJECT NUMBER	
				5e. TASK NUMBER	
				5f. WORK UNIT NUMBER	
7. PERFORMING ORGANIZATION NAME(S) AND ADDRESS(ES) Stanford University Stanford, CA 94305-5401				8. PERFORMING ORGANIZATION REPORT NUMBER	
9. SPONSORING / MONITORING AGENCY NAME(S) AND ADDRESS(ES) U.S. Army Medical Research and Materiel Command Fort Detrick, Maryland 21702-5012				10. SPONSOR/MONITOR'S ACRONYM(S)	
				11. SPONSOR/MONITOR'S REPORT NUMBER(S)	
12. DISTRIBUTION / AVAILABILITY STATEMENT Approved for Public Release; Distribution Unlimited					
13. SUPPLEMENTARY NOTES					
14. ABSTRACT With the development of computer controlled MLC, IMRT now provides unprecedented means to deliver 3D-dose distributions with sub-centimeter resolution. Inverse planning is at the foundation of IMRT and critically determines its success. As practiced now, however, the capacity of IMRT is greatly underutilized because of the inferior performance of the inverse planning systems. Because of the tacit ignorance of intra-structural tradeoff, the IMRT plans generated by these systems for prostate treatment are, at best, sub-optimal and our endeavor of providing the best possible patient care is compromised. We have carried out a systematic study on this unexplored issue and developed innovative techniques to improve prostate IMRT. A number of important milestones have been accomplished, which include (i) established a theoretical infrastructure of spatially non-uniform penalty scheme for inverse planning; (ii) developed method for incorporating existing clinical knowledge into inverse planning; (iii) proposed an electron density mapping technique to improve the quality of cone-beam CT (CBCT) images; (iv) established a robust technique for using onboard CBCT for on-treatment IMRT dose validation; (v) improved prostate IMRT beam orientation selection by integrating organ specific EUD. It is expected these tools will greatly facilitate the imaging, planning, delivery, and quality assurance of prostate IMRT.					
15. SUBJECT TERMS Prostate Cancer					
16. SECURITY CLASSIFICATION OF:			17. LIMITATION OF ABSTRACT UU	18. NUMBER OF PAGES 114	19a. NAME OF RESPONSIBLE PERSON USAMRMC
a. REPORT U	b. ABSTRACT U	c. THIS PAGE U			19b. TELEPHONE NUMBER (include area code)

Table of Contents

Cover page	1
SF 298	2
Table of Contents	3
Introduction.....	4
Body	4
Key Research Accomplishments	7
Reportable Outcomes.....	8
References.....	8
Conclusions.....	9
Appendices.....	10

I. INTRODUCTION

This Idea Award (PC040282, entitled "Prostate Dose Escalation by Innovative Inverse Planning-Driven IMRT") was awarded to the principal investigator (PI) for the period of Nov 1, 2004—Oct. 31, 2007. This is the annual report for the first funding period (Nov. 1, 2004 – Oct. 31, 2005). The goal of this project is to improve current prostate IMRT by establishing a novel inverse planning framework with non-uniform intra-structural penalty distribution. The specific aims of this project are (1) To establish an effective inverse planning algorithm with spatially non-uniform importance factors for prostate IMRT; and (2) To demonstrate the impact of the novel inverse planning formalism for prostate irradiation by using 15 previously treated prostate cases. Under the generous support from the U.S. Army Medical Research and Materiel Command (AMRMC), the PI has assembled a rigorous research team and setup a necessary infrastructure needed for the proposed research. We have contributed significantly to prostate cancer research by applying physics and engineering knowledge to prostate cancer research. A number of significant conference abstracts and refereed papers have been resulted from the support. The preliminary data obtained under the support of the grant has also enabled the PI to start new research initiatives and significantly advanced the prostate radiation therapy. In this report, the past year's research activities of the PI are highlighted.

II. RESEARCH AND ACCOMPLISHMENTS

The success of prostate Intensity modulated radiation therapy (IMRT) depends critically on the performance of inverse planning system. As it is practiced now, however, the capacity of IMRT is greatly underutilized because of the inferior performance of the inverse planning algorithms. While many techniques exist for inverse planning and, in all cases, optimizations are claimed to be successful, the plans computed by these so-called optimization systems are often out of the expectation of the physicians and multiple trial-and-errors are required. On a more fundamental level, we recently found that the existing inverse planning suffers seriously from the tacit ignorance of intra-structural tradeoff. As a result of this deficiency, the IMRT plans generated by these systems for prostate treatment are, at best, sub-optimal and our endeavor of providing the best possible patient care is compromised. We are systematically investigating the role of this unexplored issue in inverse planning and develop innovative techniques to incorporate the intra-structural tradeoff into prostate IMRT inverse planning. By adequately modeling the effect, it is anticipated that the dose to the prostate tumor volume can be escalated by more than 10% while maintaining the radiation toxicity at the current level of IMRT prostate treatment (conversely, the dose to the rectum and/or bladder can be reduced greatly if the target dose is kept at the present level). If successful, the conformality of IMRT prostate

treatment will no longer be set by the non-optimal performance of the dose optimization algorithms, but by the physical limit of IMRT. Toward the general goal of improving IMRT inverse planning and treatment of prostate cancer, we have done substantial work in the past year. The research is sorted into four categories and summarized below.

Using *a priori* clinical outcome data to improve inverse planning. IMRT plan ranking is, to a certain degree, subjective and the solution depends strongly the selection of models for inverse planning. Voxels within a target or a sensitive structure volume are generally not equivalent in achieving their dosimetric goals in IMRT planning. Inverse planning objective function should not only balance the competing objectives of different structures but also that of the individual voxels in various structures. While it is permissible for each voxel to have its own importance value, a challenging problem is how to obtain a sensible set of importance factors with a manageable amount of computing. One of the most effective ways to accomplish a spatially non-uniform penalty scheme is to incorporate existing clinical knowledge into inverse planning process. We have developed a formalism to integrate clinical endpoint data to better guide the inverse planning optimization process. In this work, we have developed a new formalism that is biologically more sensible yet clinically practical for IMRT inverse planning. In this formalism the dose-volume status of a structure is characterized by using the concept of effective volume in the voxel domain and an objective function with incorporation of the volumetric information is then constructed. The new planning tool was applied to study a hypothetical phantom case and a prostate case. Compared with the conventional inverse planning technique, we found that, for the same target dose coverage, the critical structure sparing was substantially improved for all testing prostate cases. This work was reported as an oral presentation in 2005 Annual Meeting of American Association of Physicists in Medicine (AAPM) at Seattle, WA, and a manuscript reporting the details of the work is in progress.

Evaluation of prostate IMRT dose delivery using Kilovolt (kV) onboard cone beam computed tomography (CBCT): kV CBCT based on flat-panel technology integrated with linear accelerator has recently become available from linac vendors for therapy guidance. Currently, the system is primarily utilized to guide the patient alignment. As an advanced tool of obtaining a patient's 3D representation, CBCT also affords an effective means for us to examine the actual dose distribution to be delivered or already delivered to the patient on a daily basis. We have recently evaluated the accuracy of kV CBCT-based dose calculation and addressed some logistic issues related to the application for prostate IMRT. In reality, image quality of current CBCT is not as good as conventional diagnostic CT due to the scatter and

reconstruction artifacts, which may lead to significant dosimetric inaccuracy. We investigated the feasibility and accuracy of CBCT-based dose calculation and to proposed a deformable electron density mapping (DEDM) method that is potentially useful to facilitate CBCT-based dose calculation. In the proposed DEDM technique, the CBCT and planning CT are first registered by using a deformable image registration model. The electron density distribution is then mapped from the planning CT to the CBCT. For prostate IMRT, our results agree with the planned dose distributions to within 3%. The use of DEDM reduces the dosimetric inconsistency between the CBCT-based and CT-based dose calculation down to less than 1% in both phantom and patient studies. Our technique provides an effective way to ensure that the planned IMRT dose distribution can be realized in a clinical setting and should have significant impact on clinical prostate IMRT. It also lay the foundation for future adaptive radiation therapy. This work has been submitted to *Medical Physics* for publication (preprint is attached).

Equivalent-uniform dose (EUD)-based IMRT Beam Placement: Beam orientation optimization in IMRT is computationally intensive and various single beam ranking techniques have been proposed to reduce the search space. Up to this point, none of the existing ranking techniques considers the clinically important dose-volume effects of the involved structures, which may lead to clinically irrelevant angular ranking. We have developed a clinically sensible angular ranking model with incorporation of dose-volume effects and to show its utility for IMRT beam placement. The general consideration in constructing an angular ranking function is that a beamlet/beam is more preferable if it can deliver a higher dose to the target without exceeding the tolerance of the sensitive structures located on the path of the beamlet/beam. In the previously proposed dose-based approach, the beamlets are treated independently and, to compute the maximally deliverable dose to the target volume, the intensity of each beamlet is pushed to its maximum intensity without considering the values of other beamlets. When volumetric structures are involved (such as the rectum in prostate radiotherapy), the complication arises from the fact that there are numerous dose distributions corresponding to the same dose-volume tolerance. In this situation, the beamlets are no longer independent and an optimization algorithm is required to find the intensity profile that delivers the maximum target dose while satisfying the volumetric constraint(s). In our study, the behavior of a volumetric organ was modeled by using the EUD. A constrained sequential quadratic programming algorithm (CFSQP) was used to find the beam profile that delivers the maximum dose to the target volume without violating the EUD constraint(s). It is shown that the previously reported dose-based angular ranking represents a special case of the general formalism proposed here. We also showed that the proposed technique is capable of producing clinically sensible angular ranking for a

variety of prostate cases. The IMRT plans obtained under the guidance of EUD-based angular ranking were improved in comparison with that obtained using the conventional uniformly spaced beams. The EUD-based function is a general approach for angular ranking and allows us to identify the potentially good and bad angles for clinically complicated cases. The ranking can be used either as a guidance to facilitate the manual beam placement or as prior information to speed up the computer search for the optimal beam configuration. Given its simplicity and robustness, the proposed technique should have positive clinical impact in facilitating the IMRT planning process. This work was reported as an oral presentation in 2005 Annual Meeting of American Association of Physicists in Medicine (AAPM) at Seattle, WA. We are currently refining the technique and applying it to generate class-solution for IMRT prostate treatment planning.

In addition to the above three projects, we are extending the inverse planning infrastructure for biologically conformal IMRT. Currently, an inverse planning system that allows us to utilize the spatial biology distribution does not exist. A theoretical framework to quantitatively incorporate the spatial biology data into IMRT inverse planning⁵ has been established. Biologically conformal radiation therapy (BCRT) incorporating patient specific biological information provides an outstanding opportunity for us to truly individualize radiation treatment. The techniques developed in this proposal will find natural application in the next generation BCRT treatment. Finally, the Idea Award for Prostate Cancer Research from US Army Medical Research and Materiel Command also provides a unique educational opportunity for training junior researcher through the participation of research activities.

III. KEY RESEARCH ACCOMPLISHMENTS

- Established a theoretical infrastructure for using spatially non-uniform penalty scheme to improve current IMRT inverse planning.
- Developed method for incorporating existing clinical knowledge into inverse planning system.
- Proposed an electron density mapping technique based on deformable image registration to improve the quality of cone-beam CT images.
- Established a robust technique for using onboard cone-beam CT for on-treatment dose validation for prostate IMRT.
- Improved prostate IMRT beam orientation selection procedure by integrating organ specific EUD data.

- Implemented a biological model-based BCRT inverse planning algorithm that lays the technical foundation for next generation BCRT treatment.

IV. REPORTABLE OUTCOMES

The following is a list of publications resulted from the grant support in the last funding period.

Refereed publications:

1. Yang Y, Schreibmann E., Li T., King C., and Xing L: "Dosimetric Evaluation of kV Cone-Beam CT-based Dose Calculation". *Medical Physics*, submitted, 2005.
2. Xing, L, Thorndyke B, Schreibmann E, Li T, Yang Y, Kim G., Luxton G, Koong, A, Overview of image guided radiation therapy (IGRT), *Medical Dosimetry* (invited review), to appear in March, 2006.
3. Xia P, Yu N, Xing L, Syn X, Verhey, L: "Investigation o a new objective function for inverse planning optimization". *Medical Physics* 32, 920-927, 2005.
4. Schreibmann E and Xing L: "Image registration with auto-mapped control volumes". *Medical Physics*. Submitted.
5. Xing L, Levy, D. and Yang Y., Incorporating clinical outcome data into inverse treatment planning, *Medical Physics*, manuscript in preparation.
6. Levy D, Paquin D., Schreibmann E., Xing L, Multiscale registration of medical imaging, *IEEE Transactions on Medical Imaging*, to be submitted.

Book Chapter:

1. Xing L., Yang Y., Spielman D., Molecular/Functional Image-Guided Radiation Therapy, T. Bortfeld, R. Schmidt-Ullrich, W. de Neve (editors), Springer-Verlag Heidelberg, Berlin.
2. Xing L, Wu Q, Yong Y and Boyer AL: Physics of IMRT and Inverse Treatment Planning, in Intensity Modulated Radiation Therapy: *A Clinical Perspective*, Mundt AF and Roeske JC. (editors), page 20-51, BC Decker Inc. Publisher, Hamilton, Canada, 2005.
3. Wu QW, Xing L, Ezzel G and Mohan R, Inverse Treatment Planning." *In Modern Technology of Radiation Oncology:II*. Van Dyk J (editor), Medical Physics Publishing, Madison, WI, 2005.
4. Song Y, Boyer A, Ma C, Jiang S., Xing L, Modulated Electron Beam Therapy, in Intensity Modulated Radiation Therapy: *A Clinical Perspective*, Mundt AF and Roeske JC. (editors), page 327-336, BC Decker Inc. Publisher, Hamilton, Canada, 2005.
5. Li J and Xing L, Radiation Dose Planning, Computer-Aided, in Encyclopedia of Medical Devices and Instrumentation, John G. Webster (editor), John Wiley & Sons, in press.

Conference abstract:

1. Xing, L. and Spielman D, MRI/MRSI and Radiation Therapy Treatment Planning, 2005 AAPM Annual Meeting, Seattle, WA (invited talk).
2. Schreibmann E. and Xing L., EUD-based beam orientation optimization, oral presentation in 2005 AAPM Annual Meeting, Seattle, WA.
3. Xing L, Levy, D. and Yang Y., Incorporating clinical outcome data into inverse treatment planning, oral presentation in 2005 AAPM Annual Meeting, Seattle, WA.
4. Yang Y, Schreibmann E., Li T., King C., and Xing L: "Dosimetric Evaluation of kV Cone-Beam CT-based Dose Calculation". oral presentation in 2005 AAPM Annual Meeting, Seattle, WA.
5. Yang Y. and Xing L, Prescription for biologically conformal radiation therapy, poster presentation in 2005 AAPM Annual Meeting, Seattle, WA.

6. Schreibmann E, and Xing L: "Image registration with auto-mapped control volumes". Poster presentation in 2005ASTRO annual meeting, Denver.
7. Yang Y and Xing L: "Optimization of radiation dose-time-fractionation scheme with consideration of tumor specific biology". poster presentation in 2005ASTRO annual meeting, Denver, CO.

V. CONCLUSIONS

An infrastructure has been established to execute the proposed research. Novel IMRT inverse planning and validation techniques are being developed for the treatment of prostate cancer. A few important milestones have been achieved toward the general goal of the project. These include (i) established a theoretical infrastructure of spatially non-uniform penalty scheme for inverse planning; (ii) developed method for incorporating existing clinical knowledge into inverse planning; (iii) proposed an electron density mapping technique to improve the quality of cone-beam CT (CBCT) images; (iv) established a robust technique for using onboard CBCT for on-treatment IMRT dose validation; (v) improved prostate IMRT beam orientation selection by integrating organ specific EUD. We have also implemented a biological model-based BCRT inverse planning algorithm that lays the technical foundation for next generation BCRT treatment. Integration and further refinement of the above tools are underway. It is expected these tools will substantially improve the current prostate IMRT treatment.

Appendices -- manuscripts submitted (or to be submitted) for publication

Dosimetric Evaluation of kV Cone-Beam CT (CBCT)- Based Dose Calculation[†]

Yong Yang, Eduard Schreibmann, Tianfang Li, Christopher
King, and Lei Xing^{a)}

Department of Radiation Oncology, Stanford University School of Medicine,
Stanford, CA 94305-5847

Short title: Mapping electron density distribution from planning CT to CBCT

^{a)} Author to whom correspondence should be addressed:

Department of Radiation Oncology
Stanford University School of Medicine,
Clinical Cancer Center
875 Blake Wilbur Drive, Rm G-204
Stanford, CA 94305-5847
Telephone: (650) 498-7896
Fax: (650) 498-4015
Email: lei@reyes.stanford.edu

Submitted to: *Medical Physics*

[†] Part of this work was presented in 2005 Annual Meeting of American Association of
Physicists in Medicine, Seattle, WA.

Abstract

Kilovolt (kV) CBCT based on flat-panel technology integrated with linear accelerator has recently become available from linac vendors for therapy guidance. Currently, the system is primarily utilized to guide the patient alignment. As an advanced tool of obtaining a patient's 3D representation, CBCT also affords an effective means for us to examine the actual dose distribution to be delivered or already delivered to the patient on a daily basis. Before this can be implemented clinically, the accuracy of kV CBCT-based dose calculation must be evaluated and some logistic issues related to the application need to be addressed. Indeed, image quality of current CBCT is not as good as conventional diagnostic due to the scatter and organ motion artifacts, which lead to significant dosimetric inaccuracy. This work is aimed to investigate the feasibility and accuracy of CBCT-based dose calculation and to propose a deformable electron density mapping (DEDM) method that is potentially useful to facilitate CBCT-based dose calculation. In the proposed DEDM technique, the CBCT and planning CT are first registered by using a deformable image registration model. The electron density distribution is then mapped from the planning CT to the CBCT. The CBCT with the mapped electron density information serves as the backbone for more accurate CBCT-based dose calculation. For disease sites where intra-fractional organ motion is not an issue, this study indicates that CBCT can be employed directly for dose calculation without relying on the DEDM and the results agree with the planned dose distributions to within 3%. On the other hand, in the presence of motion artifacts, the Hounsfield number distribution can be altered substantially and, as a result, it is found that the dosimetric inaccuracy can be more than 5% when the bare CBCT is used. The use of DEDM reduces the dosimetric inconsistency between the CBCT-based and CT-based dose calculation down to less than 1% in both phantom and patient studies. While the true solution to the hurdle lies in the effective removal of motion artifacts in CBCT, the DEDM approach seems to afford a useful interim technique for improved CBCT-based dose calculation.

Key word: CBCT, IGRT, Dose verification, Deformable registration

I. Introduction

Modern radiation therapy techniques, such as 3D conformal radiotherapy (3DCRT) and intensity-modulated radiation therapy (IMRT), provide unprecedented means for producing exquisitely shaped radiation doses that closely conform to the tumor dimensions while sparing sensitive structures. As a result of greatly enhanced dose conformality, more accurate beam targeting becomes an urgent issue in radiation therapy. In current practice, large uncertainties exist in tumor target localization due to intra- and inter-organ motions during the course of radiation treatment. As thus, large safety margins around the tumor targets and sensitive structures are introduced to cope with the otherwise insoluble patient localization problem. The use of non-optimal margins compromises the patient care and adversely affects the treatment outcome¹⁻⁶. The need to improve targeting in high precision radiation therapy has recently spurred a flood of research activities in image-guided radiation therapy (IGRT)⁷⁻¹¹.

CBCT based upon flat-panel technology integrated with a medical linear accelerator has recently become available from Linac vendors for therapy guidance. The volumetric images may be used to verify and correct the planning patient setup in the linac coordinates by comparing with the patient position defined in treatment plan. Both kV and MV beams^{12, 13} have been utilized for this application. The former typically consists of a kV-source and flat-panel combination mounted on the drum of a medical accelerator⁷⁻¹¹, with the kV imaging axis orthogonal to that of MV therapy beam. In addition to guide the patient setup process, CBCT data acquired prior to the treatment can, in principle, be used to recalculate or verify the treatment plan for the patient anatomy of the treatment day. The recalculation starts with the intended fluence maps from the patient's treatment plan, whereas the verification is done by using the fluence maps measured at the exiting sides of the incident beams. If CBCT-based dose calculation is accurate enough (say, with an accuracy within 3%), this will provide a valuable option for us to predict/assess the patient dose on a daily basis. In reality, because of the presence of organ movement/deformation, it is conceivable that the dose distributions delivered to the patient are usually different from fraction to fraction. It is paramount to be able to monitor the actual patient dose for each fraction as well as the accumulated doses to the target and sensitive structures while the fractional treatment

proceeding. This will not only give physician more confidence about the treatment but may, in future, afford us an effective means to adaptively modify the patient's treatment plan during the course of a radiation therapy based on the dose that has already been delivered.

The accuracy of MV fan-beam and cone-beam CT has recently been assessed by Langen et al¹⁴ and Poulliot et al¹³. The potential of its counterpart, the kV CBCT, for dosimetric calculation has, on the other hand, not been examined systematically. The purpose of this work is two-fold: to evaluate the dosimetric accuracy of kV CBCT-based dose calculation and to explore a deformable electron density mapping strategy for improving the performance of the calculation. For disease sites where intra-fractional organ motion is not an issue, the general reference drawn from this study is that it is adequate to directly use current CBCT for dose calculation because the dosimetric inaccuracy is generally less than 3% as compared with that based upon the conventional CT. On the other hand, when dealing with regions in the thorax or upper abdomen, the motion artifacts in CBCT are found quite severe and significant dosimetric errors (~5%) are observed. In this situation, the deformable electron density mapping method seems to be valuable for more accurate CBCT-based dose recalculation.

II. Method and Materials

A. Data acquisition

The on-board imager (OBI) integrated in a Trilogy™ medical linear accelerator (Varian Medical Systems, Palo Alto, CA) is used in this work to acquire CBCT images. The kV OBI system is capable of obtaining low-dose, high-resolution radiography, fluoroscopy and CBCT. The system is mounted on the treatment machine via robotically controlled arms, which operate along three axes of motion. It can be automatically positioned using the robotic technology and control software, making OBI clinically very practical. A 150 kV X-ray tube with maximum 32 ms pulse length for continuous irradiation and maximum 320 ms pulse length for single pulse is designed for generating high-resolution images from a moving gantry. The spot of the tube is located at 90° to the MV source and

100cm from the radiation axis of the accelerator. A 39.7cm X 29.8 cm amorphous silicon flat-panel X-ray image detector (Varian PortalVision™ aS1000) mounted opposite the kV tube is used to acquire digital images with a pixel matrix of 2048 X 1536. Using the OBI system, the CBCT data can be acquired in two modes: full fan mode and half fan mode. In the full fan mode, 675 projections are taken during the whole 364° gantry rotation with a field of view (FOV) about 26.6 cm in diameter and 17cm in length. The data acquisition time is about 45 second and the reconstruction time for 340 slices of 512X512 CBCT images with a voxel size of 0.5mm³ is also about 1 minute on a PC. The half fan mode is designed to obtain larger FOV. In this mode, about 965 projections are taken during the 364° gantry rotation and a FOV of 45 cm diameter X 15cm can be achieved. The data acquisition and reconstruction time for 512X512 CBCT images with a voxel size of 0.95mm³ using this mode is about double compared with the full fan mode.

B. Calibration of relative electron density

To use CT or CBCT for radiation dose calculation, it is required to relate the Hounsfield Unit (HU) of the scanner with the actual electron density. A CT-phantom, Catphan-600 module CTP404 (Phantom Laboratory, NY), was used for the calibration of planning CT (GE Discovery-ST PET/CT scanner, Milwaukee, WI) and CBCT. The CTP404 has a diameter of 150 mm and contains 17 different sizes of inserts with seven different tissue substitute materials, air, PMP, LDPE, Polystyrene, Acrylic, Delrin and Teflon, respectively. Their relative electron densities ranged from 0 to 1.866. A cross section of the phantom is shown in figure 2. The calibration of a CT scanner involves acquiring CT images, obtaining average HUs for each inserting materials, and plot the HU as a function of the relative electron density. For CBCT, it is necessary to calibrate separately for full and half fan modes because the beam geometry and characteristics of the two types of scanning modes are different. More details on the calibration procedure can be found in the manual of Trilogy.

In order to test the stability of the CBCT calibration curve with time, the phantom was repeatedly scanned every week for two months. The obtained HU vs relative electron density curves were compared to assess the HU fluctuations with time.

C. Phantom study

CT and CBCT images of the Catphan-600 phantom were acquired using the procedure outlined in Sec. II.A. The phantom was placed on a platform that can be set to one-dimensional cyclic motion with a number of speeds. The axis of the cylindrically shaped phantom, along which the phantom moves cyclically, was angled from the central axis of the couch plane by about 15° in order for the on-board imager to “see” or “realize” the motion when the cylindrical phantom moves. The movement of the phantom produces motion artifacts in the images and allows us to evaluate the performance of CBCT-based dose calculation in the presence of organ motion. The full fan mode was used to scan the phantom. CT and CBCT images of the phantom were acquired with and without motion. In the former case, the peak-to-peak amplitude of the motion was 0.5 cm and the period was 4s, which mimics the situation of a patient’s breathing motion.

To quantify the difference in the image quality of the CT and CBCT images, we first analyzed the HU distribution for the four sets of CT images, corresponding to planning CT and CBCT with and without motion. The influence of phantom motion on the HU distribution was investigated. The CT and CBCT images were imported to a Varian Eclipse treatment planning system for dosimetric comparison study. For planning and evaluation purpose, a hypothetical spherical target with a diameter of 5cm was created at the center of the phantom and a single $5 \times 5\text{cm}^2$ 6MV photon beam was used to irradiate the target. A simple beam configuration was used here because, in this way, the results are more intuitively interpretable. Four plans, corresponding to the four different sets of CT images, were generated using the same target and beam configuration. The pencil beam convolution dose calculation algorithm implemented in Varian Eclipse treatment planning system was adopted for dose calculation. The resultant isodose curves, dose profiles and DVHs were compared.

D. Patient study

A prostate cancer patient and a lung cancer patient were selected for the evaluation study of CBCT-based dose calculation and to demonstrate the feasibility of the proposed deformable electron density mapping (DEDM) technique (see next sub-section) for improved dose calculation accuracy. For the prostate case, the targets included the PTV,

consisting of the prostate gland with a margin of 6mm and the seminal vesicles. The critical structures were rectum, bladder and femoral heads. An IMRT plan using five 15MV photon beams with gantry angles of 35°, 110°, 180°, 250°, and 325° (in IEC convention) was adopted for the prostate case. The plan was normalized to deliver a prescription dose of 78Gy to 99% the prostate PTV and no less than 50Gy to the 98% of seminal vesicles in 39 fractions. For the lung cancer case, the PTV consisted of the CTV with a margin of 10mm. The critical structures involved were the right lung and the spinal cord. A conventional 3D conformal plan with three 15MV photon beams (45°, 180° and 288° in IEC convention) was generated for this case. In this plan, the field shape of each beam was determined by conforming the PTV projection in the corresponding beam direction. The plan was normalized to deliver a prescription dose of 70Gy to 100% of the target volume in 35 fractions. The CBCT images of the patients were obtained using the half fan mode. The CT and CBCT images were registered using a rigid image registration package provided in the Eclipse treatment planning system. For each case, the IMRT or 3D CRT planning parameters, which include beam configuration, MU settings, and MLC files, used for treatment were employed to recalculate the dose based on the CBCT data. The CT and CBCT-based treatment plans were then compared.

E. Deformable electron density mapping

The dosimetric inaccuracy of CBCT-based dose calculation in thorax and abdomen arises from the inability of the CBCT technique to provide accurate HU or relative electron density distribution, primarily due to organ motion induced artifacts. The genuine solution to the problem lies in the improvement of the CBCT acquisition technology so that artifact-free images can be acquired. While this endeavor is still on-going, here we propose an interim solution for dealing with the problem. Under the assumptions that the HU or relative electron density distribution is known from planning CT and an acceptable geometric registration between CT and CBCT is achievable by a deformable registration, we propose to map the electron density in the planning CT onto the daily setup CBCT and then carry out the dose calculation. The CBCT with mapped electron density, referred to as modified CBCT, possesses the anatomical information of CBCT and yet the electron density information of the planning CT. Dose calculation based on the modified

CBCT allows us to compute more accurately the delivered dose with the patient in his/her setup position. The mapping process is described as follows.

A free form spline (BSpline) deformable model ^{15, 16} was employed to register the planning CT and CBCT and map the deformed electron density from planning CT to CBCT. The method was used for several IGRT related projects in our group and others and its simplicity and accuracy have been demonstrated ^{17, 18}. Briefly, in the BSpline model, a lattice of user-defined nodes is overlaid on the image. Each node contains a deformation vector, whose components are to be determined by optimizing a metric function that characterizes the goodness of the registration. The variables of the metric function consisted of the coordinates of the BSpline nodes. In this work, a voxel-based normal cross correlation (NCC) metric was used. A suitable set of node deformations was determined using the gradient-based algorithm L-BFGS ^{16, 19}, which is known for its superior performance in large-scale optimization problems. The optimizer iteratively varies the nodal displacements to optimize the metric. The deformation at any point of the image is calculated by spline interpolation of closest nodes values. Unlike other spline models, the BSplines are locally controlled, such that the displacement of an interpolation point is influenced only by the closest grid points and changing a lattice node only affects the transformation regionally, making it efficient in describing local deformations. After the deformable registration, the HU in each voxel in planning CT was mapped to the corresponding point in the reference CBCT to produce the modified CBCT images.

The feasibility of DEDM technique was evaluated by using the two patients mentioned above. For this purpose, the CT and CBCT images were registered using the BSpline model. The targets and sensitive structures contoured on the planning CT were copied to the CBCT using the deformable model. For each patient, the treatment plan parameters were employed to recompute the dose distribution based on the patient's modified CBCT. The resultant isodose curves and DVHs were evaluated and the level of improvement in dosimetry due to the use of DEDM was assessed.

III. Results

A. Calibration of CT and CBCT

The relation between kV HU distribution of CBCT and relative electron dosimetry was established by using a Catphan-600 CT phantom following the procedure described in Sec. II.B. The calibration curves for planning CT, half fan and full fan CBCT modes are shown in figure 1a. Figure 1b compares the calibration curves obtained with an interval of 1 week during continuous two months for full fan CBCT. No significant fluctuations were found in the calibration data, which is similar to what have been observed for MV¹⁴. The stability of the kV CBCT and electron density calibration is good indicator of the HU number integrity and the overall performance of the CBCT system.

B. Phantom study

Figures 2a to 2d show the same transverse slices of the CT and CBCT images of the Catphan-600 phantom with and without motion. The first two panels are the CT and CBCT images of the phantom in the absence of motion, and the second two show the same with the phantom motion “switched on”. It is seen that the quality of CBCT images is worse than that of the conventional planning CT, especially in the presence of motion. The HU profiles of the four images along the two orthogonal lines (lines A-A and B-B as marked in figure 2) are plotted in figure 3. It is found that the HU profiles of the planning CT and CBCT normally agree to within 10% in the static situation. On the other hand, when the motion is “switched on”, CBCT shows a much greater level of artifacts (figure 2d) and the HU difference between the conventional CT and CBCT is aggravated, with the maximum difference reaching several hundred HUs.

Figures 4, 5 and 6 present the dosimetric results calculated using a single 6 MV 5 X 5cm² photon beam. Figures 4a to 4d depict the dose distributions in a transverse slice calculated based on the four sets of images given in figure 2. Figures 5a and 5b compare the dose profiles along the two orthogonal lines (lines A-A and B-B in figure 2), and figure 6 compares the DVHs of the target for the four different situations. From these results we find that the dose calculated using planning CT agrees with that of CBCT-based calculation to within 1.0%, indicating that it is acceptable to use kV CBCT for dose calculation if no organ motion presents. However, when phantom motion is involved, the motion induced artifacts significantly influence the HU distribution and thus the accuracy

of CBCT-based dose calculation. For this simple phantom case, we find that the discrepancy between the planning CT- and CBCT-based calculations is about 3%, which is clinically significant. The motion artifacts existing in current CBCT limit the direct use of CBCT for dose calculation when intra-fractional organ motion is not negligible.

C. Patient study

Figures 7a to 7c show the same transverse slices of the planning CT, CBCT, and checkerboard image resulting from the deformable registration of the two sets of images for the prostate case. The modified CBCT obtained by mapping the HUs from the planning CT to CBCT is shown in figure 7d. Our previous studies have indicated that a registration accuracy better than 2mm is achievable by using the BSpline deformable registration technique¹⁶ described in the last section. As can be seen from the checkerboard overlay, a good registration between CT and CBCT is obtained. Figure 8 shows the isodose distributions for the three types of calculations based on planning CT, CBCT, and modified CBCT. A comparison of DVHs of PTV, prostate, seminal vesicles, bladder and rectum is presented in figure 9. The results demonstrate that, while there is significant dosimetric discrepancy between the results obtained based on the planning CT and modified CBCT, the results obtained using the CBCT and modified CBCT is similar, except for the seminal vesicles, in which the DVH difference is somewhat large due to its relatively small volume and more deformation. Similar phenomenon was also observed by the MD Anderson group using their daily CT on-rail^{9, 20}. In general, the difference between the planned dose distribution and that computed based on CBCT arises from two factors: (i) patient positioning error and organ deformation/displacement; and (ii) relative electron density difference between the two sets of CT images. The small discrepancy between the doses computed using CBCT and modified CBCT suggests that, in the prostate case, the second factor is small and it is acceptable to directly use CBCT for dose calculation. The dosimetry is predominantly determined by the accuracy of patient setup and the level of interfractional deformation /displacement of the prostate, rectum and bladder.

Figure 10a to 10d show the same transverse slice from the planning CT, CBCT, checkerboard overlay of the planning CT and the modified CBCT for the lung cancer

case. Figures 11 and 12 compare the isodose distributions and the DVHs of the target and sensitive structures calculated based on the three sets of images for the three-beam 3D conformal treatment plan. In this case, the dosimetric discrepancy between the CBCT- and modified CBCT-based calculations is much larger than that in the prostate case, especially for the right lung and PTV. The maximum dose difference is about 5%. However, the discrepancy between the results obtained using planning CT and modified CBCT becomes much less. This study exemplifies that, unlike the prostate case, the dosimetric inaccuracy arising from the inferior image quality of CBCT in the dose verification calculation. The motion artifacts not only make it difficult to see the extent of the tumor, but also limit the direct use of CBCT for dose calculation.

IV. Discussion

The feasibility and accuracy of using kV CBCT to calculate dose have been investigated with a phantom and two clinical cases. In the absence of motion artifacts, it seems to be acceptable to directly use CBCT for dose verification calculation. Otherwise, extra caution is required to avoid significant dosimetric inaccuracy. To cope with the problem of deteriorated imaging quality of CBCT in the presence of organ motion, a DEDM method has been proposed to map the electron density information from the patient's planning CT to the setup CBCT with a deformable image registration. In IGRT, since the registration has to be done for the purpose of patient setup, the computational overhead of introducing DEDM is minimal. Before an effective CBCT motion artifacts removal technique is in place, DEDM provides a useful interim solution to the problem.

Dose distributions computed based on CBCT and modified CBCT represent the dose to be delivered to the patient because the CBCT was acquired prior to the patients' treatments after the patients were repositioned/shifted using the patient setup procedure in current practice. In the prostate IMRT plan, the inherent dosimetric error resulted from the use of CBCT images is small. However, the dosimetric error caused by the inter-fractional organ motion/deformation is not insignificant, as revealed by using dose recalculation results given in the last section. A few groups are working on deformable model based segmentation and patient setup procedures^{16, 9, 21, 22}. When deformable

registration is used, there are a few options to achieve the registration depending on whether the primary aim is to match soft-tissue, or to align 3D bony structures. The multiple choices resulting from the fact that the dimensionality of the patient data is much greater than that in the patient setup procedure and suggest that deformable registration is not the ultimate solution to volumetric image-guided radiation therapy. The technique improves the current body-structure-based patient alignment method since it partially takes into account organ deformation by achieving the closest overlay match possible between the planning and CBCT data sets according to our clinical objective, and provide an improved patient positioning technique. We should emphasize that, even when 3D volumetric based deformable registration is available in the future, the problem of patient positioning will not disappear as relative organ deformations/displacements may well persist. A possible solution to accommodate various factors mentioned above is for us to re-optimize or tweak the IMRT plan based on the patient's setup CBCT. Indeed, in order to fully utilize the CBCT volumetric data, a new paradigm with seamlessly integrated simulation, planning, verification, and delivery procedure is urgently needed. Until this is realized clinically, the volumetric imaging is nothing but an expensive extension of the existing planar verification approach.

For the lung 3D conformal plan, we found that the dosimetric error for the target from the organ interfractional motion/deformation and intrafractional motion is small. The main reasons are that the organ interfractional motion/deformation is not as significant as that in the prostate case and enough margins are given in the 3D conformal plan. Furthermore, the dose distribution in the target is more uniform in this case. However, the dosimetric error from the lower quality of the CBCT images becomes larger since the influence of the intrafractional motion on the CBCT image quality. In this situation, it is suggested that, in order to accurately evaluate the delivered dose distributions, the deformed CT images generated using the proposed deformable electron density mapping technique are required to replace the original CBCT images for the task of dose verification calculation.

V. Conclusion

On-board CBCT provides useful volumetric anatomy information for patient positioning verification. When used for dose verification calculation, it is required to have a reliable HU to electron density curve. Our phantom and patient study have indicated that, in the absence of motion artifacts, the dosimetric inaccuracy is generally less than 1% as compared with the calculation of the treatment planning system. The dosimetric errors are much more pronounced when intra-fractional organ motion is present. In this situation, a direct use of CBCT for dose calculation is not recommended. The use of a deformable registration permits us to incorporate the electron density distribution from the planning CT and to calculate the dose more accurately. The proposed DEDM approach affords a practical solution to estimate the dose to be delivered or already delivered to the patient based on the setup CBCT.

Acknowledgement

The supports from Department of Defense (PC040282) and National Cancer Institute (1 R01 CA98523-01) are gratefully acknowledged.

Figure Captions

Fig. 1. (a) The calibration curves (Hounsfield number vs relative electron density) for planning CT, half fan and full fan mode CBCT; (b) the variation of calibration curves with time for the full fan CBCT.

Fig. 2. The CT and CBCT images with and without motion for the Catphan-600: (a) planning CT in the absence of phantom motion; (b) CBCT in the absence of phantom motion; (c) planning CT with moving phantom; and (d) CBCT with moving phantom.

Fig. 3. HU profiles of planning CT and CBCT images (see figure 2) along the A-A line (panel a) and B-B line (panel b).

Fig. 4. Dose distributions in a transverse slice calculated based on the four sets of CT data shown in figure 2: (a) planning CT; (b) CBCT; (c) planning CT with a motion; and (d) CBCT with a motion. In all four situations, a $5 \times 5\text{cm}^2$ single field plan was used to irradiate a spherical hypothetical target with a diameter of 5cm located at the phantom center.

Fig. 5. Comparison of the dose profiles along the two orthogonal lines shown in figure 2 for the Catphan-600 phantom: (a) profile along the A-A line; (a) profile along the B-B line.

Fig. 6. Comparison of the target DVHs calculated based on the four sets of CT data shown in figure 2 for the phantom case.

Fig. 7. CT, CBCT and modified CBCT images for the prostate case: (a) planning CT; (b) daily CBCT; (c) checkerboard overlay of CT and CBCT after the deformation registration; and (d) modified CT.

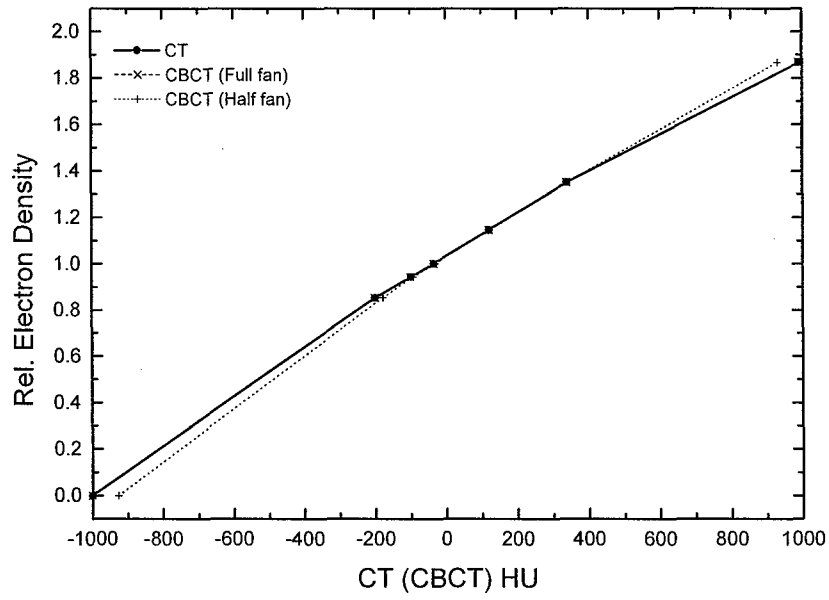
Fig. 8. Dose distributions in a transverse slice calculated based on the: (a) planning CT; (b) CBCT; and (c) modified CB CT for the prostate case.

Fig. 9. DVHs of the prostate, PTV, rectum and bladder obtained based on the planning CT, CBCT and modified CBCT images for the prostate case.

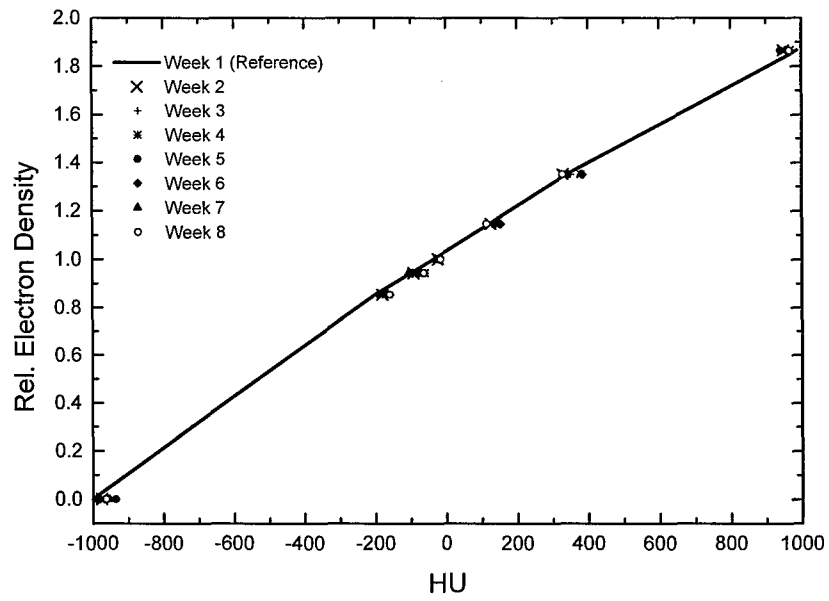
Fig. 10. CT, CBCT and modified CT images for the lung case: (a) planning CT; (b) CBCT; (c) checkerboard image after the deformation registration; and (d) modified CBCT.

Fig. 11. Dose distribution in a transverse slice calculated based on: (a) planning CT; (b) CBCT; and (c) modified CBCT for the lung case.

Fig. 12. Comparison of the DVHs of GTV, PTV, right lung and spinal cord obtained based on planning CT, CBCT and the modified CBCT images.



(a)



(b)

Figure 1

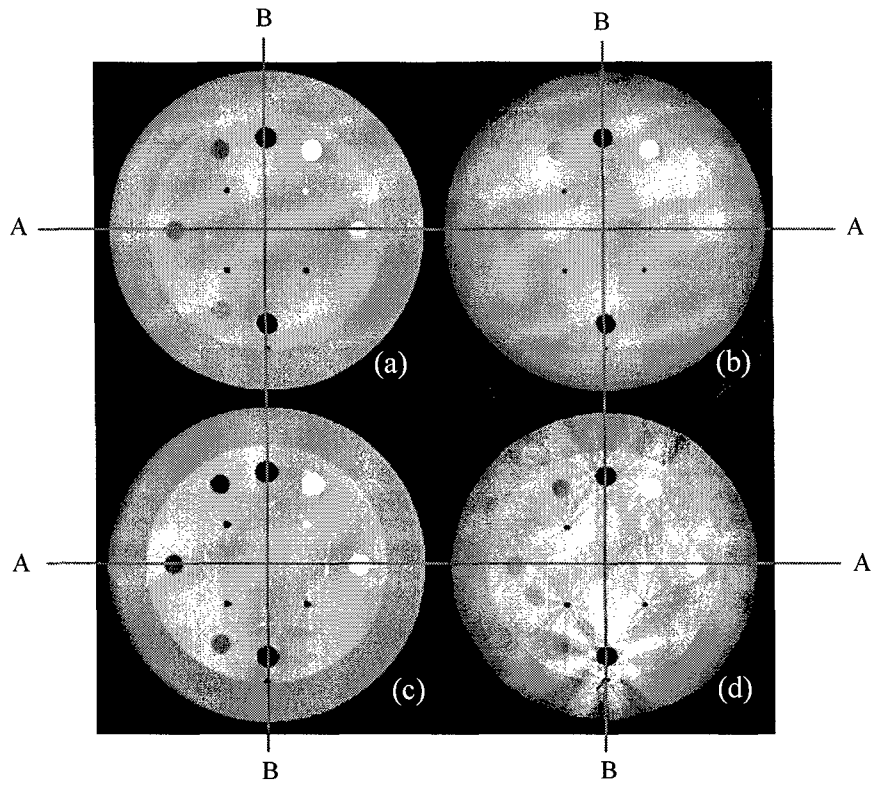
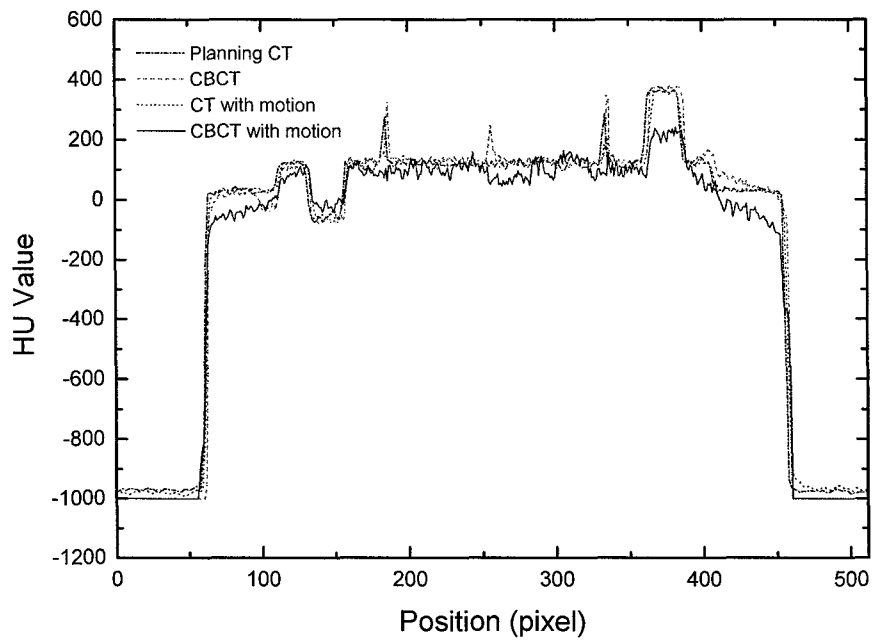
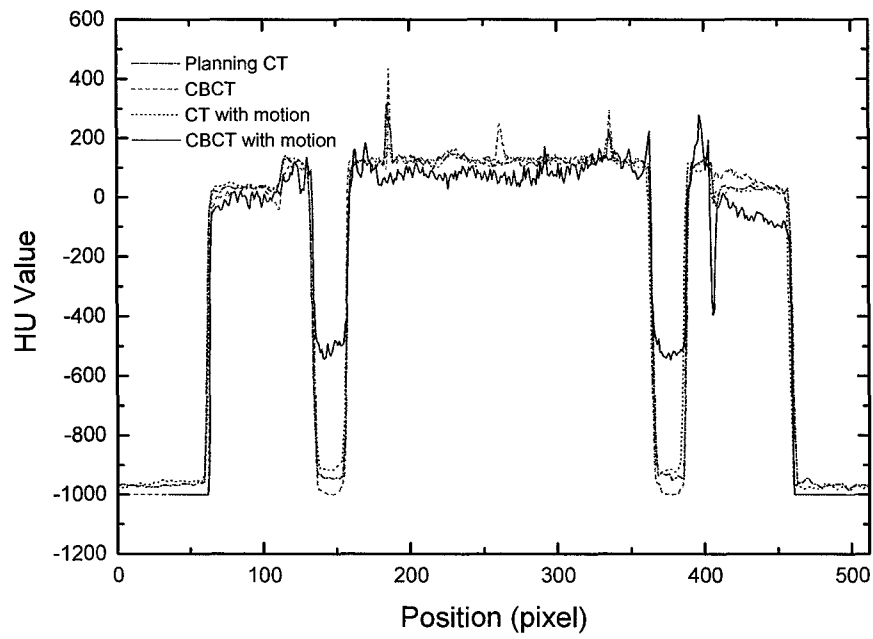


Figure 2



(a)



(b)

Figure 3

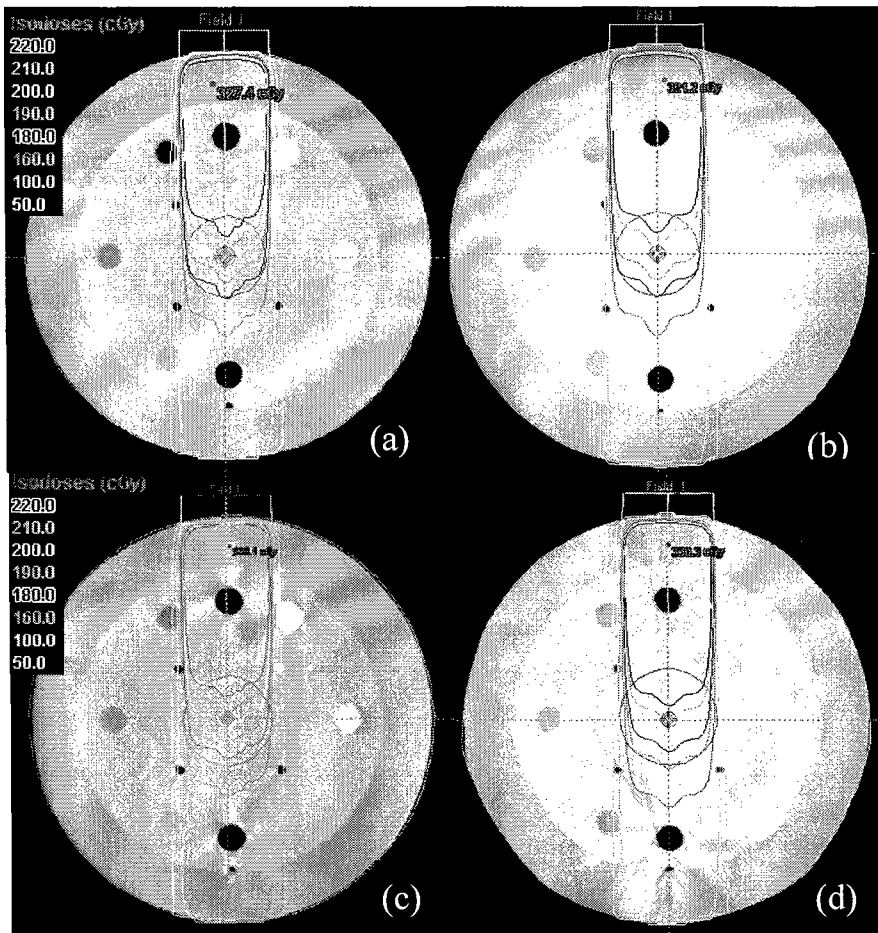
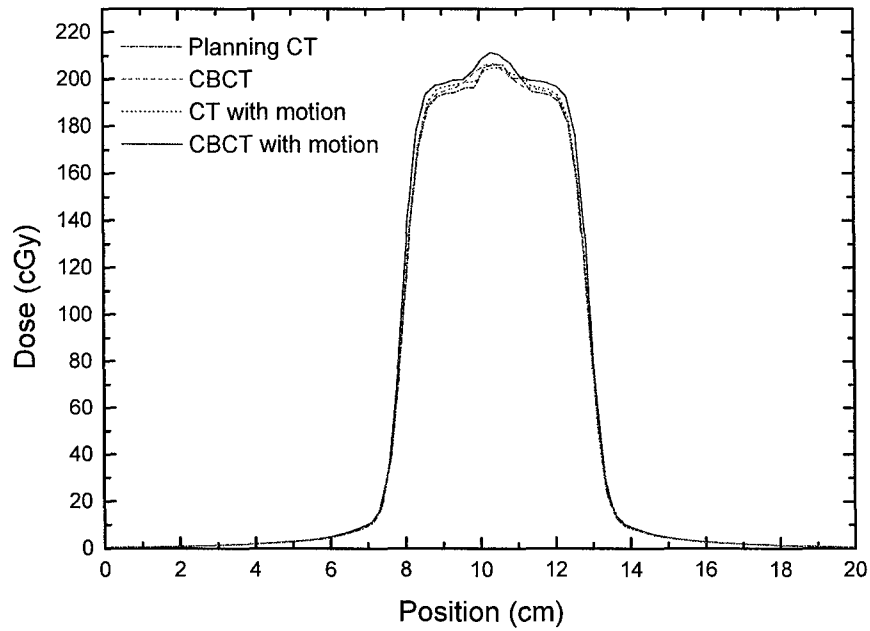
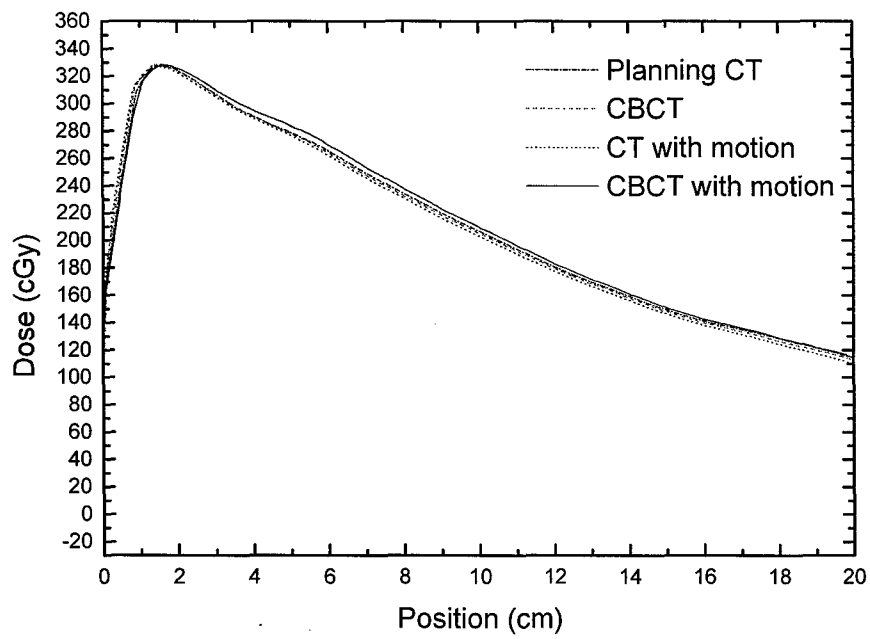


Figure 4



(a)



(b)

Figure 5

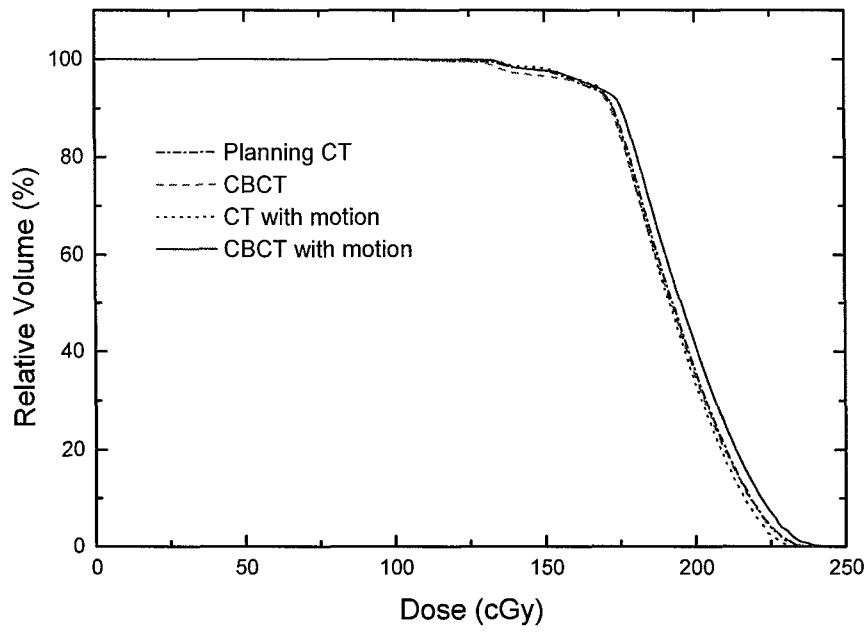


Figure 6

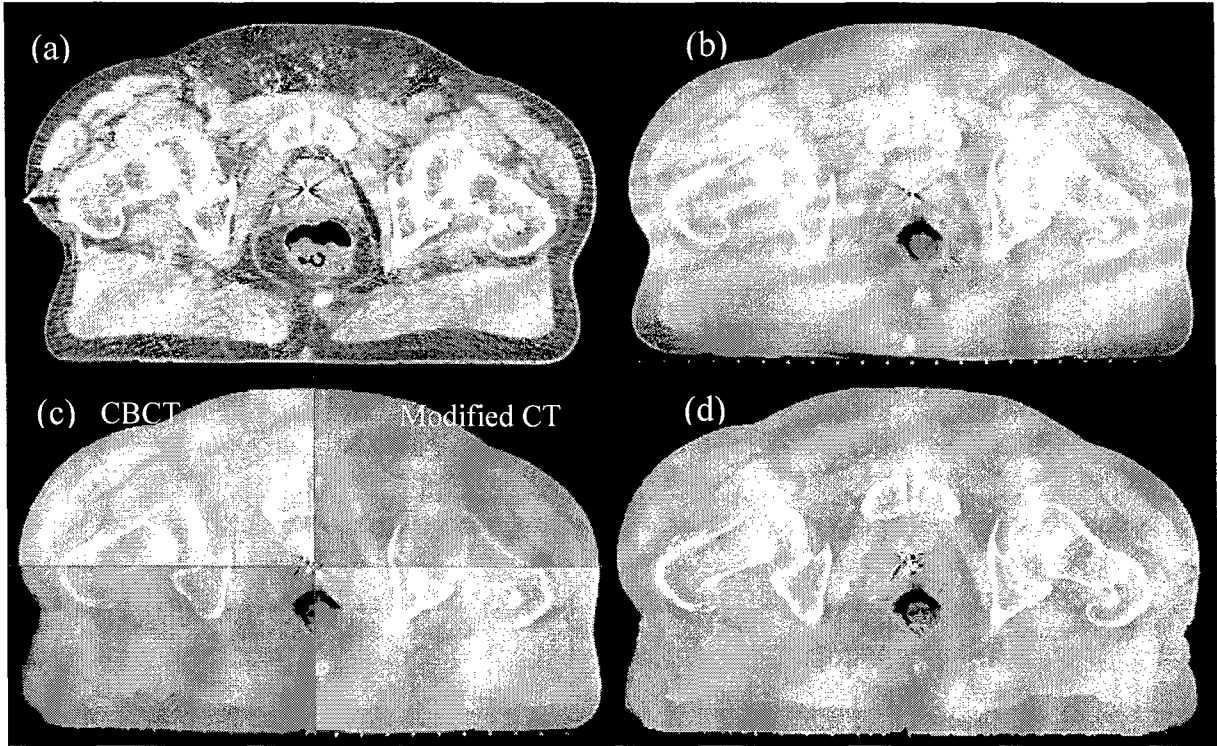


Figure 7

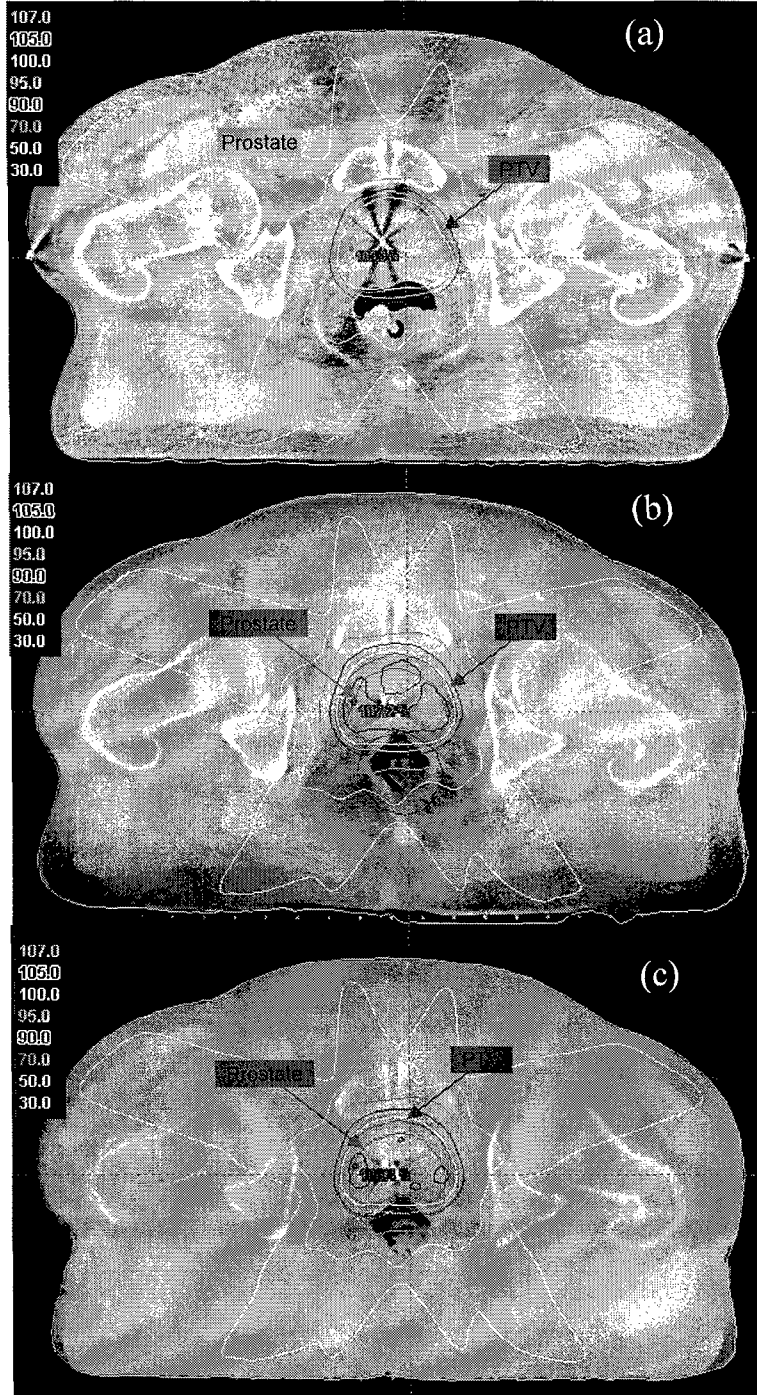


Figure 8

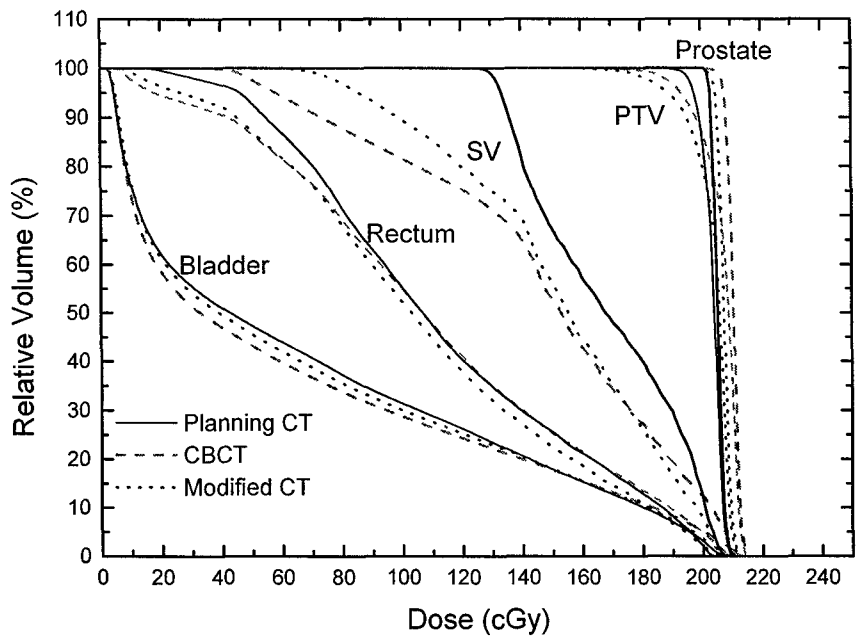


Figure 9

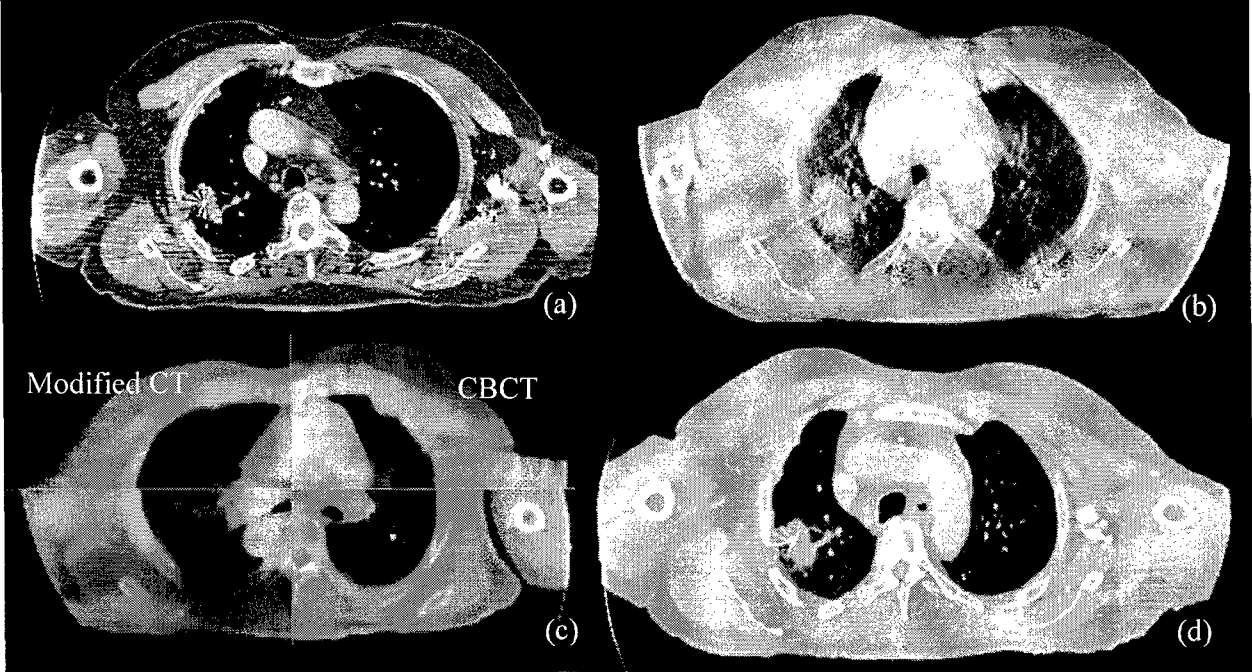


Figure 10

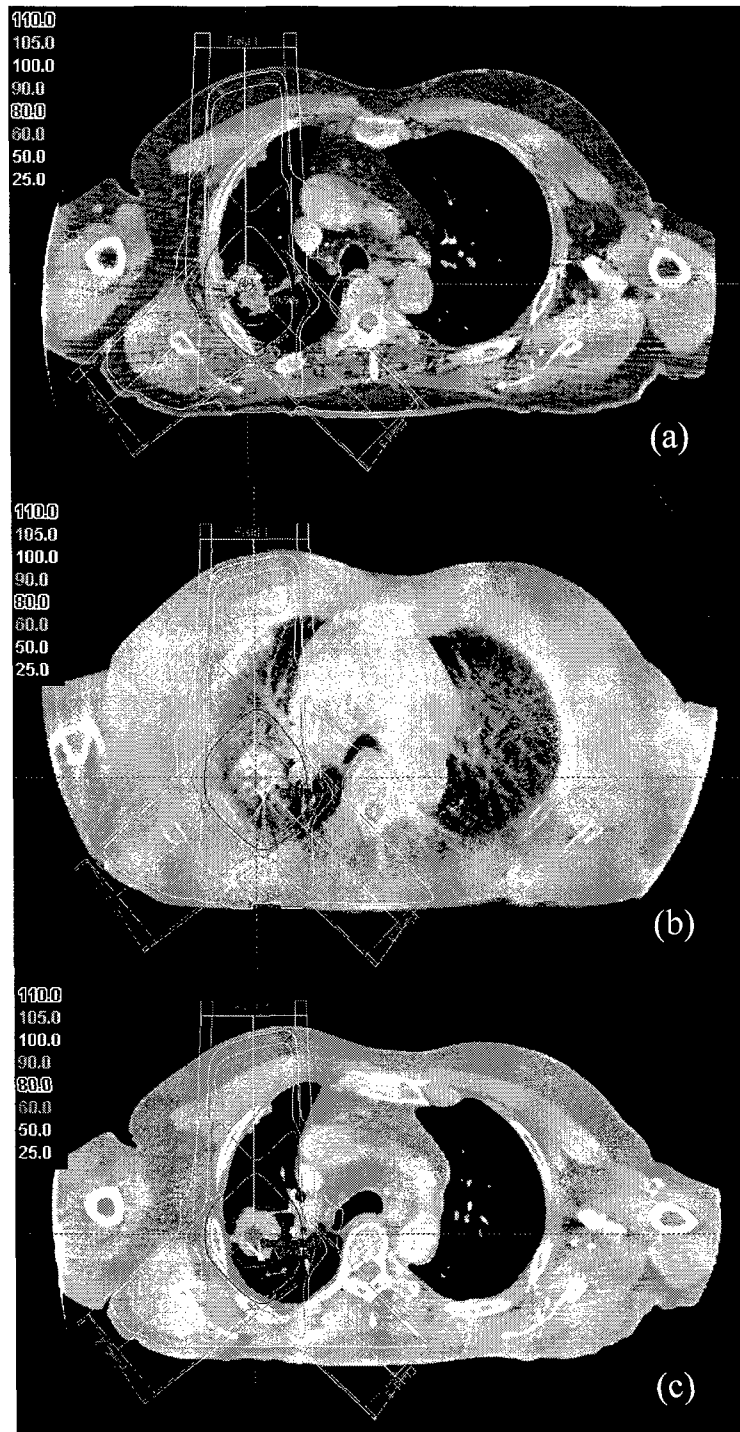


Figure 11

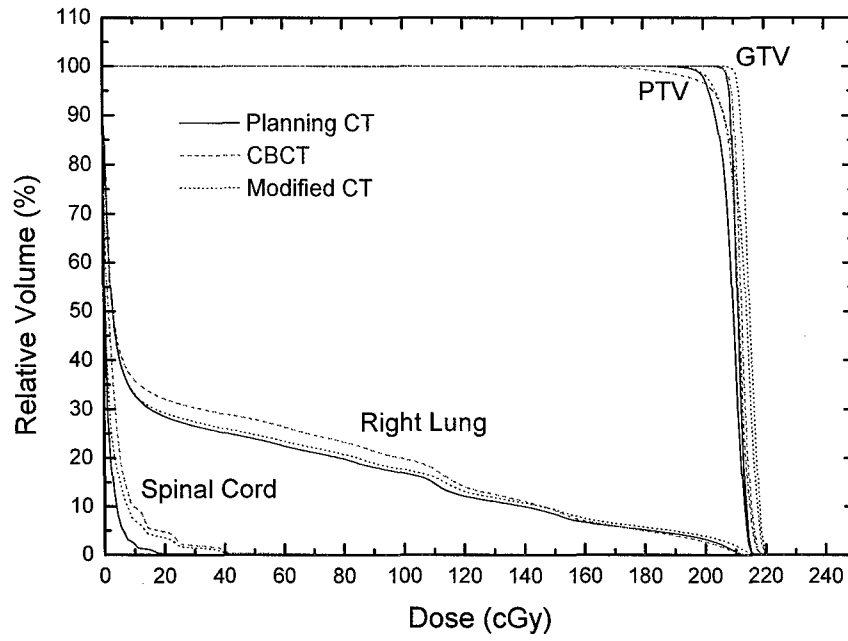


Figure 12

References

- 1 K. M. Langen and D. T. Jones, "Organ motion and its management," *Int J Radiat Oncol Biol Phys* 50, 265-278 (2001).
- 2 T. Bortfeld, S. B. Jiang and E. Rietzel, "Effects of motion on the total dose distribution," *Semin Radiat Oncol* 14, 41-51 (2004).
- 3 D. Yan and D. Lockman, "Organ/patient geometric variation in external beam radiotherapy and its effects," *Med Phys* 28, 593-602 (2001).
- 4 G. D. Hugo, N. Agazaryan and T. D. Solberg, "The effects of tumor motion on planning and delivery of respiratory-gated IMRT," *Med Phys* 30, 1052-1066 (2003).
- 5 D. S. Mohan, P. A. Kupelian and T. R. Willoughby, "Short-course intensity-modulated radiotherapy for localized prostate cancer with daily transabdominal ultrasound localization of the prostate gland," *Int J Radiat Oncol Biol Phys* 46, 575-580 (2000).
- 6 D. Yan, B. Xu, D. Lockman, K. Kota, D. S. Brabbins, J. Wong and A. A. Martinez, "The influence of interpatient and inpatient rectum variation on external beam treatment of prostate cancer," *Int J Radiat Oncol Biol Phys* 51, 1111-1119 (2001).
- 7 R. I. Berbeco, S. B. Jiang, G. C. Sharp, G. T. Chen, H. Mostafavi and H. Shirato, "Integrated radiotherapy imaging system (IRIS): design considerations of tumour tracking with linac gantry-mounted diagnostic x-ray systems with flat-panel detectors," *Phys Med Biol* 49, 243-255 (2004).
- 8 M. J. Ghilezan, D. A. Jaffray, J. H. Siewerdsen, M. Van Herk, A. Shetty, M. B. Sharpe, S. Zafar Jafri, F. A. Vicini, R. C. Matter, D. S. Brabbins and A. A. Martinez, "Prostate gland motion assessed with cine-magnetic resonance imaging (cine-MRI)," *Int J Radiat Oncol Biol Phys* 62, 406-417 (2005).
- 9 R. Mohan, X. Zhang, H. Wang, Y. Kang, X. Wang, H. Liu, K. K. Ang, D. Kuban and L. Dong, "Use of deformed intensity distributions for on-line modification of image-guided IMRT to account for interfractional anatomic changes," *Int J Radiat Oncol Biol Phys* 61, 1258-1266 (2005).

- 10 D. Letourneau, A. A. Martinez, D. Lockman, D. Yan, C. Vargas, G. Ivaldi and J. Wong, "Assessment of residual error for online cone-beam CT-guided treatment of prostate cancer patients," *Int J Radiat Oncol Biol Phys* 62, 1239-1246 (2005).
- 11 T. R. Mackie, J. Kapatoes, K. Ruchala, W. Lu, C. Wu, G. Olivera, L. Forrest, W. Tome, J. Welsh, R. Jeraj, P. Harari, P. Reckwerdt, B. Paliwal, M. Ritter, H. Keller, J. Fowler and M. Mehta, "Image guidance for precise conformal radiotherapy," *Int J Radiat Oncol Biol Phys* 56, 89-105 (2003).
- 12 S. Meeks, J. J. Harmon, K. M. Langen, T. H. Wagner and P. Kupelian, "Performance characterization of megavoltage computed tomography imaging on a helical tomotherapy unit," *Medical Physics* 32, 2673-2681 (2005).
- 13 J. Pouliot, A. Bani-Hashemi, J. Chen, M. Svatos, F. Ghelmansarai, M. Mitschke, M. Aubin, P. Xia, O. Morin, K. Bucci, M. Roach, 3rd, P. Hernandez, Z. Zheng, D. Hristov and L. Verhey, "Low-dose megavoltage cone-beam CT for radiation therapy," *Int J Radiat Oncol Biol Phys* 61, 552-560 (2005).
- 14 K. M. Langen, S. L. Meeks, D. O. Poole, T. H. Wagner, T. R. Willoughby, P. A. Kupelian, K. J. Ruchala, J. Haimerl and G. H. Olivera, "The use of megavoltage CT (MVCT) images for dose recomputations," *Phys Med Biol* 50, 4259-4276 (2005).
- 15 J. Lian, L. Xing, S. Hunjan, C. Dumoulin, J. Levin, A. Lo, R. Watkins, K. Rohling, R. Giaquinto, D. Kim, D. Spielman and B. Daniel, "Mapping of the prostate in endorectal coil-based MRI/MRSI and CT: a deformable registration and validation study," *Med Phys* 31, 3087-3094 (2004).
- 16 E. Schreibmann and L. Xing, "Narrow band deformable registration of prostate magnetic resonance imaging, magnetic resonance spectroscopic imaging, and computed tomography studies," *Int J Radiat Oncol Biol Phys* 62, 595-605 (2005).
- 17 D. Mattes, D. R. Haynor, H. Vesselle, T. K. Lewellen and W. Eubank, "PET-CT image registration in the chest using free-form deformations," *IEEE Trans Med Imaging* 22, 120-128 (2003).
- 18 D. Loeckx, F. Maes, D. Vandermeulen and P. Suetens, "Non-rigid image registration using a statistical spline deformation model," *Inf Process Med Imaging* 18, 463-474 (2003).

- 19 H. H. Liu, T. R. Mackie and E. C. McCullough, "A dual source photon beam model used in convolution/superposition dose calculations for clinical megavoltage x-ray beams," *Medical Physics* 24, 1960-1974 (1997).
- 20 L. E. Court, L. Dong, A. K. Lee, R. Cheung, M. D. Bonnen, J. O'Daniel, H. Wang, R. Mohan and D. Kuban, "An automatic CT-guided adaptive radiation therapy technique by online modification of multileaf collimator leaf positions for prostate cancer," *Int J Radiat Oncol Biol Phys* 62, 154-163 (2005).
- 21 M. Oldham, D. Letourneau, L. Watt, G. Hugo, D. Yan, D. Lockman, L. H. Kim, P. Y. Chen, A. Martinez and J. W. Wong, "Cone-beam-CT guided radiation therapy: A model for on-line application," *Radiother Oncol* (2005).
- 22 T. Li, Y. Yang, E. schreibmann and L. Xing, "A new cone-beam CT reposition technique through deformable registration," *Annual Meeting of American Association of Physicists in Medicine, Seattle, WA, (2005).*

Multiscale registration of medical images

Doron Levy, Dana Paquin, Eduard Schreibmann, and Lei Xing

28th November 2005

Abstract

A multiscale image registration technique is presented for the registration of medical images that contain significant levels of noise. Registration is achieved by obtaining a hierarchical multiscale decomposition of the noisy images and registering the resulting components. This approach enables successful registration of images that contain noise levels well beyond the amount at which ordinary registration fails. Experiments are presented that use mean squares, normalized correlation, and mutual information to demonstrate the accuracy and efficiency of the multiscale registration technique.

1 Introduction

Often in image processing, images must be spatially aligned in order to perform quantitative analyses of the images. The process of aligning images taken, for example, at different times, from different imaging devices, or from different perspectives, is called image registration. More precisely, image registration is the process of determining the optimal spatial transform that maps one image to another. Typically, two images are taken as input, and the registration process is then the optimization problem which determines the geometric mapping that brings one image into spatial alignment with the other image. In practice, the particular type of transformation as well as the notion of optimal will depend on the specific application.

Examples of applications in which image registration is particularly important include astro- and geophysics, computer vision, remote sensing, and medicine. In this paper, we will focus on medical image registration. Image registration plays an important role in the analysis of medical images. For example, images taken from different sensors often contain complementary information. By bringing the two images into alignment so that anatomical features of one modality can be detected in the other modality, the information from the different modalities can be combined. In neurosurgery, for example, tumors are typically identified and diagnosed using magnetic resonance images (MRI), but stereotaxy technology (the use of surgical instruments to reach specified points) generally uses computed tomography (CT) images. Registration of these modalities allows the transfer of coordinates of tumors from the MRI images to the CT images. See [13] for a discussion of the applications of multi-modality imaging to problems in neurosurgery. As another example, medical image data acquired prior to diagnosis can be compared with data acquired during or after treatment to determine the effectiveness of the treatment. To compare images taken at different times, however, the images must first be brought into spatial alignment with one another so that actual differences in the data can be distinguished from differences that result from the image acquisition process.

In the context of medical imaging, the goal of the registration process is to remove artificial differences in the images introduced by patient movement, differences in imaging devices, etc., but at the same time, to retain real differences due to actual variations of the objects. Medical images, however, often contain significant levels of noise due to instrumentation imperfections, data acquisition techniques, image

reconstruction methods, transmission and/or compression errors, and other factors. Although numerous successful image registration techniques have been published, we will see that ordinary image registration algorithms can fail to produce meaningful results when one or both of the images to be registered contains significant levels of noise.

Since noise is generally present in digital images, image denoising is a fundamental problem in image processing. Indeed, numerous approaches to image denoising have been presented. Thus a simple solution to the problem of image registration in the presence of noise would be to first apply a denoising algorithm to the noisy image(s), and then use existing image registration techniques to register the denoised images. However, common denoising algorithms, most notably spatial filtering algorithms, have the disadvantage that while they are successful in removing noise, they often remove edges as well. Additionally, most denoising procedures require a priori knowledge of the noise level, variance, and/or model, while this information is typically not known in practice. For these and other reasons, we will demonstrate that ordinary image registration of noisy images fails to produce acceptable results even when classical denoising algorithms are applied to the noisy images prior to registration (for significantly high levels of noise). Thus we seek a technique that enables successful image registration when one or both of the images to be registered contains noise.

In practice, we can consider an image f of consisting of *coarse* and *fine* scales. The general shape and main features of an image are considered the coarse scales, and details and textures, such as noise, are the fine scales of the image. Separating the coarse and fine scales of an image, therefore, is an effective tool in denoising. Indeed, several denoising algorithms have been proposed using separation of the coarse and fine scales of an image, most notably [18], [17], [10], and [19]. The method presented in [19] presents a multiscale technique in which an image f is decomposed in a hierarchical expansion $f \sim \sum_j u_j$, where the u_j 's (called the components of f relative to the decomposition) resolve edges of f with increasing scales. More precisely, for small k , the sum $\sum_j^k u_j$ is a coarse representation of the image f , and as k increases, the sum captures more and more detail (and hence, noise) of the image.

In this paper, we present a multiscale image registration technique based on the multiscale decomposition of [19] that is particularly effective when one or both of the images to be registered contains significant levels of noise. Since the hierarchical expansion $f \sim \sum_j u_j$ decomposes the image f into components which contain increasingly fine scales, we expect a component-wise registration algorithm to produce accurate results for noisy images. That is, given a noisy image f , for small values of k , the component $\sum_j^k u_j$ retains the general shape of the image f while removing the details and noise of the image. Thus if we wish to register the image f with another image, say g we expect that registration of the components $\sum_j^k u_j$ with g will provide an accurate estimation of the actual transformation that brings the two images into spatial alignment with one another, for sufficiently small values of k . Similarly, if both f and g are noisy, we expect decomposing both images and performing component-wise registrations should accurately estimate the optimal transformation. We will demonstrate that multiscale image registration enables successful image registration for images that contain levels of noise significantly higher than the levels at which ordinary registration fails.

This paper is organized in the following way. In Section 3, we discuss the image registration problem and review standard image registration techniques. In Section 4, we present the problem of image registration in the presence of noise, and illustrate the failure of current techniques when one or both of the images to be registered contains high levels of noise. We also briefly discuss classical denoising techniques, and illustrate the failure of ordinary image registration of noisy images even when the images are denoised prior to registration. In Section 6, we review the multiscale image decomposition of [19], and illustrate the results of the hierarchical multiscale decomposition obtained upon applying the algorithm to noisy images. In Section 7, we present image registration techniques based upon the multiscale decomposition described in Section 6, and in Section 8, we present our registration results. Finally, in Section 9, we discuss computational aspects of our registration algorithm.

2 Acknowledgments

3 The registration problem

Given a *fixed* and *moving* image, the registration problem is the process of finding an *optimal transformation* that brings the moving image into spatial alignment with the fixed image. While this problem is easy to state, it is difficult to solve. The main source of difficulty is that the problem is ill-posed, which means, for example, that the problem may not have a unique solution. Additionally, the notion of optimality may vary for each application: for example, some applications may require consideration only of rigid transformations, while other applications require non-rigid transformations. Finally, computation time and data storage constraints place limitations on the complexity of models that can be used for describing the problem.

3.1 The mathematical setting

A two-dimensional gray-scale image f is a mapping which assigns to every point $x \in \Omega \subset \mathbb{R}^2$ a gray value $f(x)$ (called the intensity value of the image at the point x). We will consider images as elements of the space $L^2(\mathbb{R}^2)$. Color images can be defined, for example, in terms of vector-valued functions $\mathbf{f} = (f_1, f_2, f_3)$ representing the RGB-color scales. For the medical imaging applications that we are interested in, images are in fact given in terms of discrete data, and the function f must be obtained via interpolation. We will not discuss this construction here, but assume that an interpolation method has been chosen and fixed.

Image registration is typically necessary when two images are essentially of the same object, but the images are not spatially aligned. This occurs, for example, when the images are taken at different times, from different perspectives, or from different imaging devices. The basic input data to the registration process are two images: one is defined as the fixed image $f(x)$ and the other as the moving image $m(x)$. The goal is then to find a transformation ϕ such that the fixed image $f(x)$ and the deformed moving image $m_\phi(x) := m(\phi(x))$ are similar. To solve this problem in a mathematical way, the term similar needs to be defined in an appropriate fashion. For example, if the images to be registered are taken from different devices, there may not be a correspondence between the intensities $f(x)$ and $m_\phi(x)$ for an optimal ϕ . Additionally, we may consider measures of similarity between the images which are not related to the intensities. Thus the registration problem necessarily involves a discussion of the distance measures, or metrics, used to compare images. The general problem can then be stated as follows:

Given a distance measure $D : (L^2(\mathbb{R}^2))^2 \rightarrow \mathbb{R}$ and two images $f(x), m(x) \in L^2(\mathbb{R}^2)$, the solution ϕ of the registration problem is given by the following minimization problem:

$$\phi = \underset{\psi: \mathbb{R}^2 \rightarrow \mathbb{R}^2}{\operatorname{argmin}} D(f, m_\psi) \quad (3.1)$$

In many applications, the set of allowable transformations to be considered in the minimization problem (3.1) is restricted to a strict subset of the set of all maps $\psi : \mathbb{R}^2 \rightarrow \mathbb{R}^2$. For example, we may require the transformation ϕ to be smooth, or we may impose specific parametric requirements, such as requiring the transformation to be rigid, affine, polynomial, or spline.

3.2 Landmark-based registration

Landmark-based registration is an image registration technique which is based on a finite set of image features. The problem is then to determine the transformation such that for a finite set of features, any feature of the moving image is mapped onto the corresponding features of the fixed image. More precisely,

let $F(f, j)$ and $F(m, j)$, $j = 1, \dots, m$ be given features of the fixed and moving images, respectively. The solution ϕ of the registration problem is then a map $\phi : \mathbb{R}^2 \rightarrow \mathbb{R}^2$ such that

$$F(f, j) = \phi(F(m, j)), \quad j = 1, \dots, m. \quad (3.2)$$

For a more general notion of landmark-based registration, we define the following distance measure:

$$D^{\text{LM}}(\phi) := \sum_{j=1}^m \|F(f, j) - \phi(F(m, j))\|_l^2, \quad (3.3)$$

where $\|\cdot\|_l$ denotes a norm on the landmark, or feature, space. For example, if the features are locations of points, then $\|\cdot\|_l = \|\cdot\|_{\mathbb{R}^2}$. We can then restate (3.2) as the minimization problem in which the solution $\phi : \mathbb{R}^2 \rightarrow \mathbb{R}^2$ of the registration problem is given by:

$$\phi = \underset{\psi: \mathbb{R}^2 \rightarrow \mathbb{R}^2}{\operatorname{argmin}} D^{\text{LM}}(\psi). \quad (3.4)$$

To solve this minimization problem, the transformation is chosen to either be an element of an n -dimensional space spanned, for example, by polynomials, splines, or wavelets, or it is required to be smooth in some sense. In the first case, the features to be mapped are the locations of a number of user-supplied landmarks. Let χ_k , $k = 1, \dots, n$ be the basis functions of the space. Then the minimization of

$$D^{\text{LM}}(\phi) := \sum_{j=1}^m \|F(f, j) - \phi(F(m, j))\|_l^2 = D^{\text{LM}}(\phi) := \sum_{j=1}^m \|F(f, j) - \phi(F(m, j))\|_{\mathbb{R}^2}^2$$

can be obtained upon expanding $\phi = (\phi_1, \phi_2)$ in terms of the basis functions and solving the resulting least squares problems.

In the case in which we require the transformation ϕ to be smooth, we introduce a functional which imposes smoothness restrictions on the transformation. That is, we look for a transformation ϕ which interpolates the features $F(f, j)$ and $F(m, j)$, and which is smooth in some sense. Such a transformation is called a minimal norm solution, and it turns out (see [8]) that the solution can be expressed in terms of radial basis functions.

Landmark-based registration is simple to implement and the numerical solution requires only the solution of a linear system of equations. However, the main drawback of the landmark-based approach is that the registration process depends on the location of the landmarks. As the detection and mathematical characterization of landmarks (for example, anatomical landmarks in medical images) is not fully automated, the landmarks must be user-supplied, and this can be a time-consuming and difficult process, even for a medical expert; see, for example, [16]. Additionally, landmark-based registration does not always result in a physically meaningful registration. See [11], pp. 44, for a simple example of a situation in which landmark-based registration fails to produce meaningful results.

3.3 Principal axes-based registration

Principal-axes image registration is based on the idea of landmark-based registration, but it uses features that can be automatically detected. These features are constructed as follows. For an image $f : \mathbb{R}^2 \rightarrow \mathbb{R}$, and a function $g : \mathbb{R}^2 \rightarrow \mathbb{R}$, we define the expectation value of g with respect to f by

$$\mathbb{E}_f(g) := \frac{\int_{\mathbb{R}^2} g(x) f(x) dx}{\int_{\mathbb{R}^2} g(x) dx} \quad (3.5)$$

If $u : \mathbb{R}^2 \rightarrow \mathbb{R}^{m \times n}$, we set $\mathbb{E}_f(u) := (\mathbb{E}_f[u_{j,k}] \in \mathbb{R}^{m \times n}$.

The center of an image f is defined by

$$C_f := \mathbb{E}_f[x] \in \mathbb{R}^2 \quad (3.6)$$

and the covariance by

$$\text{Cov}_f := \mathbb{E}_f[(x - C_f)(x - C_f)^T] \in \mathbb{R}^{2 \times 2} \quad (3.7)$$

Given fixed and moving images $f(x)$ and $m(x)$, the centers c_f and c_m and eigendecompositions of the covariance matrices Cov_f and Cov_m are used as the features F_i , and the registration problem is to compute $\phi: \mathbb{R}^2 \rightarrow \mathbb{R}^2$ such that $F_i(m(\phi)) = F_i(f)$ for the features F_i .

This method is described in detail in [1]. The principal-axes method of image registration has the advantages that it is computationally fast and simple and requires few registration parameters, but has the disadvantages that it is not suitable for images of multiple modalities and that the solutions may be ambiguous. In particular, the principal-axes based method cannot distinguish between images with the same center and covariance, even though images with very different structure and orientation may have the same center and/or covariance.

3.4 Optimal parametric registration

In this section, we present methods of registration which are based on the minimization (or maximization) of some distance measure, or metric, D . The transformation ϕ is restricted to some parameterized space, and the registration can be obtained by minimizing (or maximizing) the distance D over the space. In particular, we will discuss metrics based on intensity, correlation, and mutual information. Given a metric D , a fixed image f , and a moving image m , optimal parametric registration is the problem of finding a transformation ϕ in some pre-specified parameterizable space such that $D(f, m(\phi))$ is minimized (or maximized in certain cases). Examples of commonly used parameterizable spaces in image registration are polynomial and spline spaces. We will primarily be interested in rigid and affine linear transformations. An affine linear map is a map of the form $\phi(x) = Ax + b$, $A \in \mathbb{R}^{2 \times 2}$, $\det A > 0$, $b \in \mathbb{R}^2$. Such a map allows rotations, translations, scales, and shears of the coordinates. A translation (or rigid) transformation is a special case of an affine transformation which allows only rotations and translations of the coordinates, and in this case, the matrix A is required to be orthogonal with determinant 1. Optimal parametric registration is probably the most commonly used image registration technique.

3.4.1 Choosing an optimizer

To minimize $D(f, m(\phi))$, we must choose an optimization technique. That is, an optimal parametric registration technique is described by a metric to be minimized (or maximized) and an optimizer which controls the minimization (or maximization). The implementation of the registration algorithm works in the following way. At each iteration, the distance D between the two images is computed. An affine transformation is then applied to the moving image, and the distance between the images is recomputed. This process continues until the distance is minimized (or maximized).

The optimizer controls this algorithm. At each stage, the optimizer determines the parameters of the transformation that will be applied to the moving image. Examples of commonly used optimizers include gradient descent and regular step gradient descent. Gradient descent optimization advances the parameters of the transformation in the direction of the gradient, where the step size is governed by a user-specified learning rate. Regular step gradient descent optimization advances the parameters of the transformation in the direction of the gradient where a bipartition scheme is used to compute the step size.

3.4.2 Mean squares metric

The mean squares metric computes the mean-squared pixel-wise difference in intensity between two images f and m :

$$\text{MS}(f, m) := \frac{1}{N} \sum_{i=1}^N (f_i - m_i)^2, \quad (3.8)$$

where N is the total number of pixels considered, f_i is the i^{th} pixel of image f , and m_i is the i^{th} pixel of image m . Note that the optimum value of the mean squares metric is 0, and poor matches between the images f and m results in large values of $\text{MS}(f, m)$. This metric has the advantage that it is computationally simple, but it is based on the assumption that pixels in one image should have the same intensity as (spatially) corresponding pixels in the second image. Thus, the mean squares metric is restricted to images of the same modality.

3.4.3 Normalized correlation metric

The normalized correlation metric computes pixel-wise cross-correlation and normalizes it by the square root of the autocorrelation function:

$$\text{NC}(f, m) := -1 \times \frac{\sum_{i=1}^N (f_i \cdot m_i)}{\sqrt{\sum_{i=1}^N f_i^2 \cdot \sum_{i=1}^N m_i^2}}, \quad (3.9)$$

where N , f_i , and m_i are as defined for the mean squares metric. The -1 factor in (3.9) causes the optimum value of the metric to occur when the minimum is reached. Thus the optimal value of the normalized correlation metric is -1. As with the mean squares metric, the normalized correlation metric is restricted to images of the same modality.

3.4.4 Viola-Wells mutual information metric

Mutual information is an information-theoretic approach to image registration that was proposed independently by Viola and Wells [21] and Collignon et al [4] in 1995. The idea is that mutual information computes the amount of information that one random variable (here, image intensity) gives about another random variable (here, intensity values of another image). More precisely, given a fixed image $f(x)$ and a moving image $m(x)$, we wish to compute the transformation ϕ which *maximizes* the mutual information

$$\phi = \arg \max_{\psi} I(f(x), m(\phi(x))). \quad (3.10)$$

The maximization of mutual information criterion assumes that the statistical dependence between corresponding image intensity values is maximized when the images are geometrically aligned.

The mutual information $I(f(x), m(\phi(x)))$ is defined in terms of entropy, where we consider x as a random variable over coordinate locations in the coordinate system of the fixed image. Let $h(\cdot)$ denote the entropy of a random variable: $h(x) := -\int p(x) \ln p(x) dx$, where $p(x)$ is the probability density function of the random variable x . Note that it is not clear how to construct $p(x)$; we will discuss methods for estimating the probability densities. The joint entropy of two random variables x and y is given by $h(x, y) = -\int p(x, y) \ln p(x, y) dx dy$, where $p(x, y)$ is the joint probability density function of the random variables x and y . Entropy can be considered as a measure of the uncertainty or complexity of a random variable.

If x and y are independent, then $p(x, y) = p(x)p(y)$, so $h(x, y) = h(x) + h(y)$. However, if there is any dependency (as would be the case if x and y are intensity values of images of the same object), then $h(x, y) < h(x) + h(y)$. The difference is defined to be mutual information:

$$I(f(x), m(\phi(x))) = h(f(x)) + h(m(\phi(x))) - h(f(x), m(\phi(x))). \quad (3.11)$$

The terms in (3.11) can be interpreted in the following way. The first term $h(f(x))$ is the entropy of the fixed image and is independent of the transformation ϕ . The second term $h(m(\phi(x)))$ is the entropy of $m(\phi(x))$, so maximization of mutual information encourages transformations ϕ for which $m(\phi(x))$ has a high level of complexity or uncertainty. The third term $-h(f(x), m(\phi(x)))$ is the negative joint entropy of $f(x)$ and $m(\phi(x))$, so maximization of mutual information is related to minimization of the joint entropy of $f(x)$ and $m(\phi(x))$. Taken together, the second and third terms identify transformations ϕ that find complexity in the images and explain it well. In [15], the authors present a detailed overview of mutual information based registration.

Mutual information has the following properties. Let $u(x)$ and $v(x)$ denote two images.

1. $I(u(x), v(x)) = I(v(x), u(x))$ Mutual information is symmetric. Although this is true theoretically, in practice, it is not always the case that we obtain the same transformation upon registering $u(x)$ with $v(x)$ and $v(x)$ with $u(x)$. This is a consequence of numerical implementation methods.
2. $I(u(x), u(x)) = h(u(x))$. The information an image contains about itself is equal to the entropy of the image.
3. $I(u(x), v(x)) \leq h(u(x))$ $I(u(x), v(x)) \leq h(v(x))$ The information that the images contain about each other can not be greater than the information contained in the individual images.
4. $I(u(x), v(x)) \geq 0$
5. $I(u(x), v(x)) = 0$ if and only if $u(x)$ and $v(x)$ are independent. That is, if the images $u(x)$ and $v(x)$ are independent, no information about one image is gained when the other image is known.

The entropies in Equation (3.11) are defined in terms of integrals over the probability densities associated with the images $f(x)$ and $m(x)$. However, in a typical medical image registration problem, the probability densities are not directly accessible, and thus must be estimated from the image data. Parzen windowing, described in [5], is a commonly used technique for estimating the densities, and it is the one used by Viola and Wells in [21]. In this method, continuous density functions are constructed by a super-position of kernel functions $K(\cdot)$ centered the elements of a sample of intensities taken from the image. That is, the estimation of the probability density $p(z)$ is given by:

$$p(x) \cong P^*(z) = \frac{1}{N_S} \sum_{z_j \in S} K(z - z_j), \quad (3.12)$$

where N_S is the number of spatial samples in S and K is an appropriately chosen kernel function. The kernel function K must be smooth, symmetric, have zero mean, and integrate to 1. Examples of suitable candidates for K include the Gaussian density and the Cauchy density. In [21], Viola and Wells use a Gaussian density function with standard deviation σ to estimate the probability density functions. The optimal value of σ depends on the particular images to be registered.

Upon estimating the probability densities using the Parzen windowing technique, the entropy integral $h(z) = -\int p(z) \ln(p(z)) dz$ must be evaluated. This integral is difficult, or impossible, to evaluate analytically, so it must be approximated as a sample mean:

$$h(z) \cong -\frac{1}{N_R} \sum_{z_j \in R} \ln(P^*(z_j)), \quad (3.13)$$

where R is a second sample of intensities taken from the image. That is, two separate intensity samples S and R are taken from the image. The first is used to estimate the probability density, and the second is used to approximate the entropy.

The main advantage of the mutual information measure is that it is generally applicable for multi-modality registration, whereas intensity-based measures are typically not applicable for multi-modality registration. Mutual information registration has been used successfully for a number of difficult applications. Most notable, mutual information has been shown to be highly accurate for MRI-CT registration. See, for example, [9], [14], and [20], for a discussion of these applications.

3.5 Non-parametric image registration

All of the image registration techniques that we have discussed so far have been based on certain parameters. For example, either the transformation ϕ can be expanded in terms of basis functions that span a specified finite-dimensional space, or the registration is controlled by a specified set of external features. Non-parametric techniques do not restrict the transformation to a parameterizable set. Given two images, a fixed image $f(x)$ and a moving image $m(x)$, we seek a transformation ϕ such that $m(\phi(x))$ is similar to $f(x)$ in a certain sense. Upon defining a suitable distance measure D , the registration problem is then to minimize the distance between $m(\phi(x))$ and $f(x)$. However, a direct minimization is often not possible in the non-parametric case. For example, the problem is ill-posed: small changes in the input data may lead to large changes in the output. Additionally, the solution is not unique. Given these constraints, a stable numerical implementation is often not possible. To circumvent these problems, a regularizing, or smoothing, term S is introduced, and the registration problem becomes the minimization of the distance between $m(\phi(x))$ and $f(x)$ plus a smoothing term $S(\phi)$. That is, the registration is based on a regularized minimization of the distance between the images.

In the discussion of non-parametric image registration, the transformation $\phi : \mathbb{R}^2 \rightarrow \mathbb{R}^2$ is split into the trivial identity part and the deformation or displacement part u , i.e.

$$\phi(x) = x - u(x). \quad (3.14)$$

Upon decomposing ϕ in this way, we have $m(\phi(x)) = m(x - u(x)) := m_u(x)$. Given a distance D and a smoother S , the elastic registration problem is then the minimization of $D(f(x), m_u(x)) + \alpha S(u)$, where $\alpha \in \mathbb{R}$ is a positive regularizing parameter.

The choice of smoother S typically depends on the particular application. Examples of non-parametric image registration techniques include elastic registration [3], fluid registration [2], and diffusion registration [7]. Elastic registration uses linear elasticity theory to model the deformation of an elastic body. In this case, the regularizing term $S(u)$ is the linearized elastic potential of the displacement u . In fluid registration, the regularization is based on the linearized elastic potential of the time derivative of u . Finally, diffusion registration uses regularization based on spatial derivatives of the displacement.

3.6 Remarks

In this section, we presented a brief overview of the major image registration techniques currently used in medical image registration. In practice, the best registration method for a given set of images will depend on the particular features of the images themselves. However, numerous comparison studies which compare the accuracy and performance of different image registration techniques for various applications

have been presented. The most extensive of these is [22], which originally consisted of a comparison of 16 different methods, but has since been substantially expanded.

4 Registration in the presence of noise

In this section, we study the effect of noise on image registration, and we determine the approximate noise level at which registration fails. Consider the brain proton density slice images shown in the figure below. The image on the right is the result of translating the image on the left by 13 mm in X and 17 mm in Y. Let I denote the original image, and let T denote the translated image.

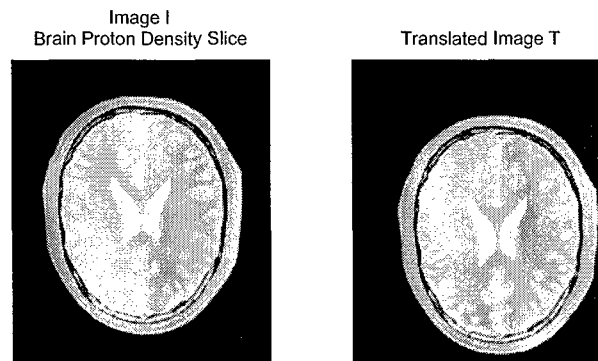


Figure 1: Original image I and translated image T

Initially, we will consider the registration problem in which one of the images (here, the fixed image) is noisy. We will add increasing levels of noise to the image I and register the non-noisy translated image T with the noisy images. Our goal is to determine the approximate noise levels at which various image registration techniques fail, and to develop an algorithm that will enable registration beyond these levels. Eventually, we will also apply our techniques to the case in which both the fixed and moving images contain significant levels of noise. Before we present these results, we discuss the notion of noise in more mathematical detail.

4.1 Noise

Digital images are often degraded by random noise. In imaging, the term noise refers to random fluctuations in intensity values that occur during image capture, transmission, or processing, and that may distort the information given by the image. Image noise is not part of the ideal signal and may be caused by a wide range of sources, such as detector sensitivity, environmental radiation, transmission errors, discretization effects, etc. Noise is generally classified as either independent noise, or noise which is dependent on the image data.

Independent noise can often be described by an additive noise model, in which the observed image f is the sum of the true image s and the noise n :

$$f(x) = s(x) + n(x). \quad (4.1)$$

Within this framework of additive noise, the noise $n(x)$ is commonly modeled by Gaussian noise of mean m and variance v .

A multiplicative noise model describes noise that is dependent on the image data. This is often referred to as speckle noise.

$$f(x) = s(x) + s(x)n(x) = s(x)(1 + n(x)) \quad (4.2)$$

In this case, $n(x)$ is uniformly distributed random noise with mean m and variance v .

Impulse noise, or salt and pepper noise, is noise that resembles salt and pepper granules randomly distributed over the image. Impulse noise is typically defined by the following model. Again we let $s(x)$ denote the actual image, and $f(x)$ denote the observed image.

$$f(x) = \begin{cases} s(x) & \text{with probability } 1 - \delta \\ \eta(x) & \text{with probability } \delta, \end{cases} \quad (4.3)$$

where $\eta(x)$ is an identically distributed, independent random process. With this model, an arbitrary pixel $x \in \Omega \subset \mathbb{R}^2$ is affected by noise with probability δ , and not affected with probability $1 - \delta$. We will refer to δ as the impulse noise density, as adding impulse noise of density δ to an image $f(x)$ affects approximately $\delta \cdot \text{size}(f)$ pixels. The random process $\eta(x)$ is typically such that the corrupted pixels are either set to the maximum value, have single bits flipped over, or are set alternatively to zero or to the maximum value. This last case results in a "salt and pepper" appearance. Note that unaffected pixels always remain unchanged.

In Figure 2, we add additive Gaussian noise of mean 0 and variance 0.2, multiplicative speckle noise of mean 0 and variance 0.2, and impulse noise of density 0.2 to the brain proton density slice image I.

In this paper, we will study the problem of image registration in the presence of high levels of impulse noise, although we believe that our solution is applicable to registration in the presence of other forms of noise, as well. We add impulse noise of increasing densities δ to the brain proton density slice image I, and register the (non-noisy) translated image T with the noisy images. Let I_δ denote the image I with added impulse noise of density δ . In 3, we illustrate the noisy images for increasing values of δ .

4.2 Registration results

For each δ in 3, we register T with I_δ using various registration methods. Recall that the image T is the result of translating the original image I 13 units in X and 17 units in Y, and that I_δ is the result of adding uniform impulse noise of density δ to the image I. Since T is a rigid transformation of I, we will restrict the registration process to linear transformations, i.e. we will consider optimal linear registrations. The optimal transformation ϕ produced by the optimal linear registration process will consist of two parameters, namely X- and Y-translation values. We will let ϕ_X and ϕ_Y denote the X- and Y-translation parameters, respectively, of the optimal transformation ϕ . For comparison purposes, we will perform the optimal linear registration using the mean squares metric, normalized correlation metric, and mutual information metric.

We use the following parameters for the registration algorithms. For the mean squares and normalized correlation registration algorithms, we use the regular step gradient descent optimizer. Due to the stochastic nature of the metric computation in the mutual information algorithm, the regular step gradient descent optimizer does not work well in the case of mutual information. Instead, we use the gradient

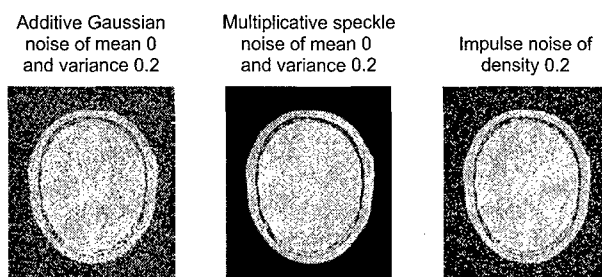


Figure 2: In this figure, we illustrate the addition of various types of noise to the image I.

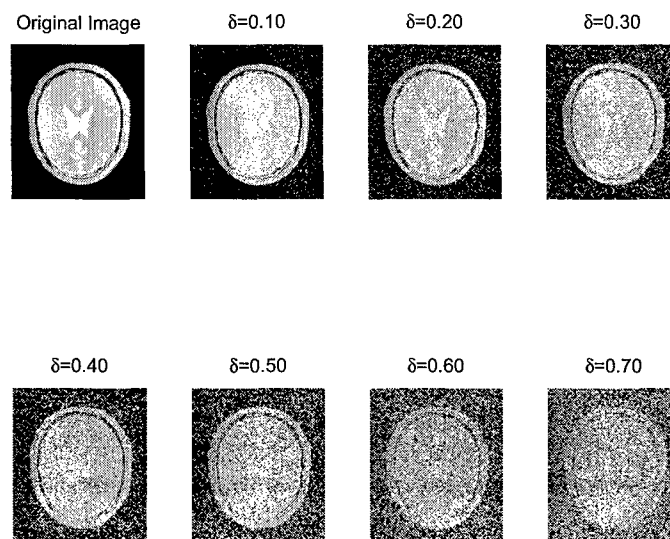


Figure 3: In this figure, we illustrate the addition of impulse noise of increasing densities δ to the image I.

δ	Mean squares			Normalized correlation			Mutual information		
	ϕ_X	ϕ_Y	n	ϕ_X	ϕ_Y	n	ϕ_X	ϕ_Y	n
0	12.99	17.00	18	13.01	17.00	18	12.75	17.03	200
0.10	12.99	17.01	28	12.99	17.01	20	12.83	16.88	200
0.20	13.03	16.98	17	13.04	16.98	19	12.98	16.64	200
0.30	12.97	17.03	28	13.02	17.02	11	13.02	17.02	200
0.40	18.89	7.16	15	8.05	1.30	13	11.08	9.72	200
0.50	2.16	7.06	19	9.09	2.18	8	9.72	7.12	200
0.60	29.81	3.19	40	4.08	0.24	7	4.57	5.17	200
0.70	2.08	1.14	13	3.11	2.13	12	3.08	2.86	200

Table 1: In this table, we present the results obtained upon registering the translated image T with the noisy image I_δ , where δ is the impulse noise density. We let ϕ_X and ϕ_Y denote the X- and Y-translation values of the optimal transformation ϕ produced by the registration algorithm, and we denote by n the number of iterations until convergence. Recall that the actual translation values are 13 units in X and 17 units in Y.

descent optimizer with a user-specified learning rate of 20.0. Finally, we set the maximum number of iterations for each algorithm to 200. As we will see, mean squares and normalized correlation registrations typically converge very quickly to the optimum value. Mutual information, on the other hand, often does not ever actually reach the true optimal solution, but instead oscillates within one or two pixels of the optimal solution (generally after 100-150 iterations). By reducing the learning rate, we can increase the likelihood of convergence, but this increases the computation time significantly without improving the accuracy of the solution.

For each of these three registration algorithms, and for each δ we record the X- and Y-translation parameters, denoted ϕ_X and ϕ_Y , respectively, of the optimal transformation ϕ produced by the registration process. We also record the number of iterations n until convergence. The results are illustrated in Table 1. Recall that the actual translation values are 13 units in X and 17 units in Y. We also record the number of iterations until convergence, which we denote by n .

The results presented in Table 1 indicate that optimal linear registration in the presence of impulse noise fails when the impulse noise density in the fixed image reaches approximately 0.40.

5 Denoising

5.1 Denoising techniques

In this section, we discuss various denoising techniques. Image denoising is a fundamental problem in image processing, and there has been much research and progress on the subject. As our primary interest in this paper is the problem of image registration of noisy images, and not denoising, we do not focus on the general problem of image denoising, but instead present a few of the most common and computationally simple denoising techniques. We will then apply these techniques to one of our noisy images, and study the effect of denoising on the image registration techniques. In particular, in Section 4, we saw that ordinary optimal linear registration of noisy images failed when the impulse noise density was greater than 0.40. In this section, we determine whether or not denoising prior to registration enables successful registration of noisy images for which registration failed previously.

Spatial filtering is the traditional approach to removing noise from images. Spatial filters use the

assumption that noise occupies the higher regions of the frequency spectrum, and thus attenuate high spatial frequencies. Filtering is a neighborhood process, in which the value of a given pixel in the filtered image is computed by applying some algorithm to the pixel values in a neighborhood of the given pixel. Typical implementations of spatial filters include mean filtering, median filtering, and Gaussian smoothing. Mean filtering computes the value of each output pixel by computing the statistical mean of the neighborhood of the corresponding input pixel. Thus, applying a mean filter to a noisy image reduces the amount of variation in gray-level intensity between pixels. Although this filter is computationally easy to implement, it is sensitive to the presence of outliers. Median filtering, which computes the value of each output pixel by computing the statistical median of the neighborhood of the corresponding input pixel, is more robust to the presence of outliers, and is thus commonly used for removing impulse noise from images. Convolution with a Gaussian kernel is another commonly used spatial filtering technique.

In Figure 4, we illustrate the effect of applying a mean, median, and Gaussian convolution filter to the noisy image $I_{0.70}$, the brain proton density slice image with impulse noise of density 0.70.

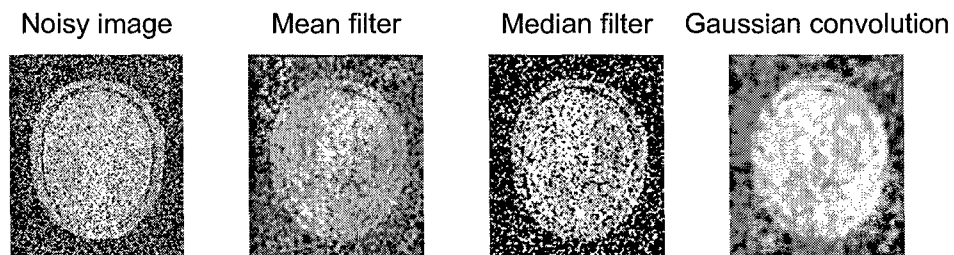


Figure 4: In this figure, we illustrate the results of applying three different denoising filters to the brain proton density slice image with impulse noise of density 0.70.

Denoising Technique	Mean squares			Normalized correlation			Mutual information		
	ϕ_X	ϕ_Y	n	ϕ_X	ϕ_Y	n	ϕ_X	ϕ_Y	n
Mean filtering	31.83	1.15	46	16.88	1.11	29	5.39	5.30	200
Median filtering	18.87	1.26	31	2.38	6.90	34	4.39	4.06	200
Gaussian convolution	18.86	-0.76	31	2.19	0.25	11	7.38	7.37	200

Table 2: In this table, we present the results obtained upon registering the translated image T with the denoised images obtained upon applying median, mean, and Gaussian convolution filters to the noisy image $I_{0.70}$. We let ϕ_X and ϕ_Y denote the X- and Y-translation values of the optimal transformation ϕ produced by the registration algorithm, and we denote by n the number of iterations until convergence. Recall that the actual translation values are 13 units in X and 17 units in Y.

5.2 Registration results after denoising

In this section, we register the translated image T with the denoised images illustrated in Figure 4. As in Section 4, we use mean squares, normalized correlation, and mutual information optimal linear registration. For each registration method, we let ϕ denote the optimal transformation produced by the registration algorithm, and we let ϕ_X and ϕ_Y the X- and Y-translation parameters of the optimal transformation ϕ . We denote by n the number of iterations of each registration algorithm until convergence. We record the results in Table 2. The moving image in each case is the translated image T; recall that the actual translation values are 13 in X and 17 in Y.

The results presented in Table 2 indicate that the application of common denoising techniques prior to registration does not enable successful registration of the noisy image $I_{0.70}$ with the translated image T. While the denoising algorithms presented here are reasonably successful in removing noise, they also remove a significant amount of detail from the images and blur edges. Since denoising prior to registration fails to give successful results, we present an image registration technique based on a multiscale decomposition of the image(s) to be registered.

6 Multiscale decomposition

6.1 The hierarchical decomposition

In this section, we present the multiscale image representation using hierarchical (BV, L^2) decompositions of [19]. Consider an image $f \in L^2(\Omega)$. Define the J-functional $J(f, \lambda)$ as follows:

$$J(f, \lambda) := \inf_{u+v=f} \{\lambda \|v\|_{L^2}^2 + \|u\|_{BV}\},$$

where $\lambda > 0$ is a scaling parameter that separates the L^2 and BV terms. This functional $J(f, \lambda)$ was introduced in the context of image processing by Rudin, Osher, and Fatemi [18]. They suggest the following. Let $[u_\lambda, v_\lambda]$ denote the minimizer of $J(f, \lambda)$. The BV component, u_λ captures the coarse features of the image f , while the L^2 component, v_λ captures the finer features of f such as noise. This model is effective in denoising images while preserving edges, though it requires prior knowledge on the noise scaling λ .

Tadmor, Nezzar, and Vese propose an alternative point of view in which the minimization of $J(f, \lambda)$ is interpreted as a decomposition $f = u_\lambda + v_\lambda$, where u_λ extracts the edges of f and v_λ extracts the textures of f . This interpretation depends on the scale λ , since "texture" at scale λ consists of edges when viewed under a refined scale (2^λ , for example). Then we decompose v_λ as follows:

$$v_\lambda = u_{2\lambda} + v_{2\lambda}, \text{ where } [u_{2\lambda}, v_{2\lambda}] = \underset{u+v=v_\lambda}{\operatorname{arginf}} J(v_\lambda, 2\lambda).$$

Thus we obtain a two-scale representation of f given by $f \cong u_\lambda + u_{2\lambda}$. Continuing this process, we obtain a hierarchical multiscale decomposition of f , as follows. Starting with an initial scale $\lambda = \lambda_0$, we obtain an initial decomposition of the image f :

$$f = u_0 + v_0, [u_0, v_0] = \underset{u+v=f}{\operatorname{arginf}} J(f, \lambda_0).$$

We then refine this decomposition to obtain

$$v_j = u_{j+1} + v_{j+1}, [u_{j+1}, v_{j+1}] = \underset{u+v=v_j}{\operatorname{arginf}} J(v_j, \lambda_0 2^{j+1}), j = 0, 1, \dots$$

After k steps of this process, we have the following hierarchical decomposition of f :

$$\begin{aligned} f &= u_0 + v_0 \\ &= u_0 + u_1 + v_1 \\ &= u_0 + u_1 + u_2 + v_2 \\ &= \dots \\ &= u_0 + u_1 + \dots + u_k + v_k \end{aligned}$$

Thus we obtain a multiscale image decomposition $f \sim u_0 + u_1 + \dots + u_k$, with a residual v_k . As k increases, the u_k components resolve edges with increasing scales $\lambda_k = \lambda_0 2^k$.

6.2 Implementation

6.2.1 Initialization

As described in [], the initial scale λ_0 should capture the smallest oscillatory scale in f , given by

$$\frac{1}{2\lambda_0} \leq \|f\|_{W^{-1,\infty}} \leq \frac{1}{\lambda_0}.$$

However, in practice, we may not be able to determine the size of $\|f\|_{W^{-1,\infty}}$, so we determine the initial choice of λ_0 experimentally. For the applications presented in this paper, we will use $\lambda_0 = 0.01$ and $\lambda_j = \lambda_0 2^j$.

6.2.2 Numerical discretization

We follow the numerical algorithm of Tadmor, Nezzar, and Vese for the construction of our hierarchical decomposition. In each step, we use finite-difference discretization of the Euler-Lagrange equations associated with the $J(v_j, \lambda_{j+1})$ to obtain the next term, u_{j+1} , in the decomposition of the image f . The Euler-Lagrange equation associated with the minimization of $J(f, \lambda)$ is

$$u_\lambda - \frac{1}{2\lambda} \operatorname{div}\left(\frac{\nabla u_\lambda}{|\nabla u_\lambda|}\right) = f,$$

with Neumann boundary conditions.

We thus obtain an expansion $f \sim \sum_{j=0}^k u_j$, where the u_j are constructed as approximate solutions of the recursive relation given by the following elliptic PDE:

$$u_{j+1} - \frac{1}{2\lambda_{j+1}} \operatorname{div}\left(\frac{\nabla u_{j+1}}{|\nabla u_{j+1}|}\right) = -\frac{1}{2\lambda_j} \operatorname{div}\left(\frac{\nabla u_j}{|\nabla u_j|}\right).$$

Note that $J(f, \lambda)$ contains a singularity when $|\nabla u_\lambda| = 0$. To remove this singularity, we replace $J(f, \lambda)$ by the regularized functional

$$J^\epsilon(f, \lambda) := \inf_{u+v=f} \{\lambda \|v\|_{L^2}^2 + \int_\Omega \sqrt{\epsilon^2 + |\nabla u|^2} dx dy\},$$

and at each step, we find the minimizer u_λ of J^ϵ . The Euler-Lagrange equation for the regularized J^ϵ functional is

$$u_\lambda - \frac{1}{2\lambda} \operatorname{div} \left(\frac{\nabla u_\lambda}{\sqrt{\epsilon^2 + |\nabla u_\lambda|^2}} \right) = f \text{ in } \Omega,$$

with Neumann boundary conditions.

To numerically implement the method, we cover the domain Ω with a grid ($x_i := ih, y_j := jh$), and discretize the elliptic PDE given above using the forward, backward, and centered divided differences. Let D_+ , D_- , and D_0 denote the forward, backward, and centered divided differences, respectively. The discretized PDE is as follows:

$$\begin{aligned} u_{i,j} &= f_{i,j} + \frac{1}{2\lambda} D_{-x} \left[\frac{1}{\sqrt{\epsilon^2 + (D_{+x} u_{i,j})^2 + (D_{0y} u_{i,j})^2}} D_{+x} u_{i,j} \right] \\ &\quad + \frac{1}{2\lambda} D_{-y} \left[\frac{1}{\sqrt{\epsilon^2 + (D_{0x} u_{i,j})^2 + (D_{+y} u_{i,j})^2}} D_{+y} u_{i,j} \right] \\ &= f_{i,j} + \frac{1}{2h^2} \left[\frac{u_{i+1,j} - u_{i,j}}{\sqrt{\epsilon^2 + (D_{+x} u_{i,j})^2 + (D_{0y} u_{i,j})^2}} - \frac{u_{i,j} - u_{i-1,j}}{\sqrt{\epsilon^2 + (D_{-x} u_{i,j})^2 + (D_{0y} u_{i-1,j})^2}} \right] \\ &\quad + \frac{1}{2h^2} \left[\frac{u_{i,j+1} - u_{i,j}}{\sqrt{\epsilon^2 + (D_{0x} u_{i,j})^2 + (D_{+y} u_{i,j})^2}} - \frac{u_{i,j} - u_{i,j-1}}{\sqrt{\epsilon^2 + (D_{0x} u_{i,j-1})^2 + (D_{-y} u_{i,j})^2}} \right] \end{aligned}$$

To solve the discrete regularized Euler-Lagrange equations, we use the Gauss-Siedel iterative method to obtain:

$$\begin{aligned} u_{i,j}^{n+1} &= f_{i,j} + \frac{1}{2h^2} \left[\frac{u_{i+1,j}^{n+1} - u_{i,j}^{n+1}}{\sqrt{\epsilon^2 + (D_{+x} u_{i,j}^n)^2 + (D_{0y} u_{i,j}^n)^2}} - \frac{u_{i,j}^{n+1} - u_{i-1,j}^n}{\sqrt{\epsilon^2 + (D_{-x} u_{i,j}^n)^2 + (D_{0y} u_{i-1,j}^n)^2}} \right] \\ &\quad + \frac{1}{2h^2} \left[\frac{u_{i,j+1}^{n+1} - u_{i,j}^{n+1}}{\sqrt{\epsilon^2 + (D_{0x} u_{i,j}^n)^2 + (D_{+y} u_{i,j}^n)^2}} - \frac{u_{i,j}^{n+1} - u_{i,j-1}^n}{\sqrt{\epsilon^2 + (D_{0x} u_{i,j-1}^n)^2 + (D_{-y} u_{i,j}^n)^2}} \right] \end{aligned}$$

To satisfy the Neumann boundary conditions, we first reflect f outside Ω by adding grid lines on all sides of Ω . As the initial condition, we set $u_{i,j}^0 = f_{i,j}$. We iterate this numerical scheme for $n = 0, 1, \dots, N$ until $\|u^{n\infty} - u^{n\infty-1}\|$ is less than some preassigned value so that $u_{i,j}^{n\infty}$ is an accurate approximation of the fixed point steady solution u_λ .

Finally, we denote the final solution $u_\lambda := \{u_{i,j}^{n\infty}\}_{i,j}$. To obtain the hierarchical multiscale decomposition, we reiterate this process, each time updating f and λ in the following way:

$$\begin{aligned} f_{\text{new}} &\leftarrow f_{\text{current}} - u_\lambda, \\ \lambda_{\text{new}} &\leftarrow 2\lambda_{\text{current}}. \end{aligned}$$

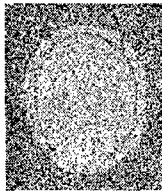
That is, at each step, we apply the $J(f_{\text{current}} - u_\lambda, 2\lambda)$ minimization to the residual $f_{\text{current}} - u_{\text{lambda}}$ of the previous step. Taking $\lambda_j = \lambda_0 2^j$, we obtain after k steps a hierarchical multiscale decomposition $f = u_{\lambda_0} + u_{\text{lambda}_1} + \dots + u_{\lambda_k} + v_{\lambda_k}$, where we write $u_{\lambda_j} = u_j$. We call the u_j , $j = 1, 2, \dots, k$ the components of f and the v_k the residuals.

6.3 Decomposition of a noisy image

Consider the image $I_{0.70}$ shown below. This is the brain proton density slice image I with impulse noise of density 0.70.

We apply the hierarchical multiscale decomposition to this noisy image, using the following parameters:

- $k = 12$ hierarchical steps
- $\lambda_0 = 0.01$

Figure 5: Noisy Image $I_{0.70}$

- $\lambda_j = \lambda_0 2^j$
- $\epsilon = 0.001$
- $n = 10$
- $h = 1$

The figures below illustrate the components u_{λ_j} and the residuals v_{λ_j} for this decomposition. Note that in each hierarchical step, an additional amount of texture is seen in the components. Further, the noise is not seen in the first few components, while most of the texture is kept, and the noise only reappears as the refined scales reach the same scales as the noise itself. Eventually, we will use this multiscale decomposition to register the noisy image $I_{0.70}$ with the translated image T.

7 Multiscale Registration

Consider the brain proton density slice I with added impulse noise of density δ . Recall that registration of the the translated image T with the noisy image failed when $\delta \geq 0.40$ using the mean squares, normalized correlation, and mutual information registration methods. Moreover, registration using these classical methods failed even after denoising the noisy image using various standard denoising techniques. In this section, we present new methods for image registration that enable successful registration of the translated image T with the noisy images I_δ for values of the noise density δ significantly greater than the levels at which classical registration and registration after denoising fails. These registration techniques will be based on the hierarchical multiscale decomposition described in Section 6.

Consider two images A and B, and suppose that we want to register image B with image A. Suppose that one or both of the images contains a significant amount of noise. If only one of the images is noisy, call the noisy image A. We propose the following multiscale registration method. First, we apply the multiscale hierarchical decomposition to both images. Let m denote the number of hierarchical steps used for the multiscale decompositions. For ease of notation, given an image f , we let $C_k(f) := \sum_{i=0}^k u_{\lambda_i}$ denote the k^{th} component of the image f , $k = 0, 1, \dots, m - 1$ obtained as in Section 6. Thus $C_k(A)$ will denote the k^{th} component of the image A, and $C_k(B)$ will denote the k^{th} component of image B.

We will present two separate algorithms; in the first, we consider registration of image B with components of image A, and in the second, we consider registration of components of image B with components of image A.

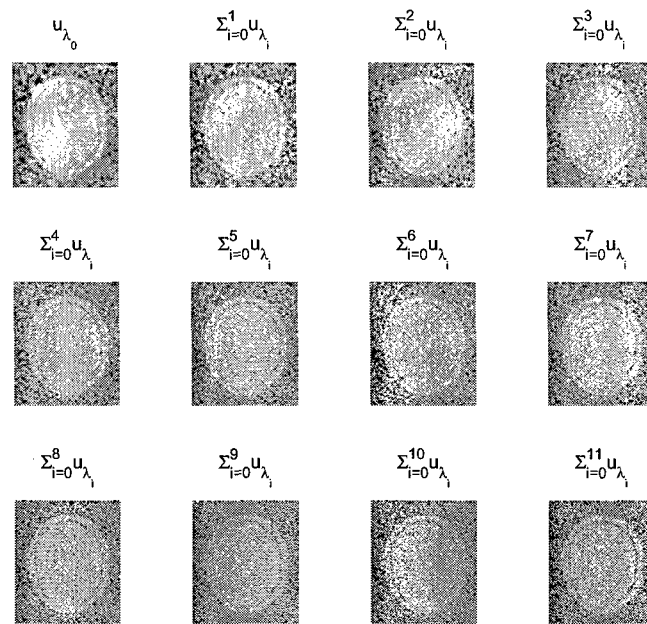


Figure 6: Multiscale decomposition of the noisy image $I_{0.70}$

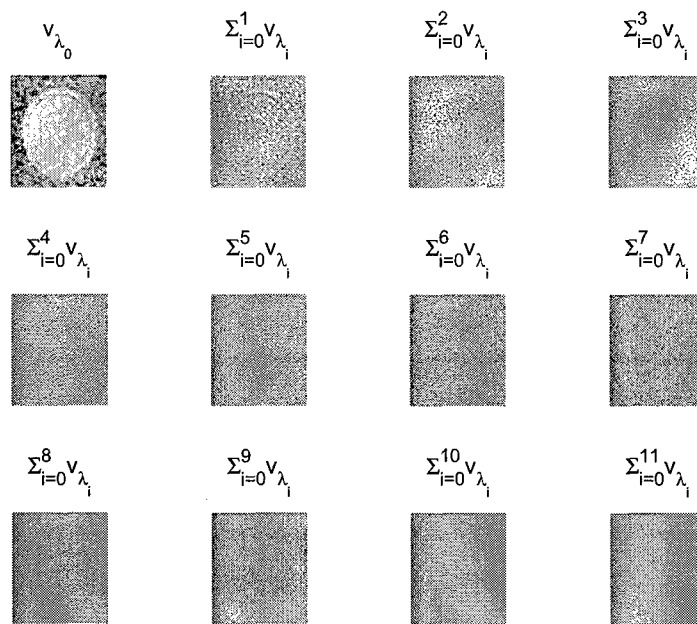


Figure 7: Residuals

7.1

In our first multiscale registration algorithm, we register image B with the k^{th} component of A, for $k = 0, 1, \dots, m-1$. This is illustrated by the following schematic:

Let ϕ_k denote the optimal transformation produced by the registration algorithm upon registering B with $C_k(A)$, $k = 0, 1, \dots, m-1$. Recall that $C_0(A)$ contains only the coarsest scales of the image A, and as k increases, $C_k(A)$ contains increasing levels of detail (and hence, noise) of the image A. Thus we expect that registration of image B with $C_k(A)$ should give an improvement compared to ordinary registration for the first few values of k . As k increases, however, we expect that eventually the component $C_k(A)$ will become too noisy to give successful registration.

Upon determining the transformations ϕ_k via a suitable registration algorithm, we have several options for defining the optimal transformation Φ that should bring the image B into spatial alignment with the image A. The first option would be to define Φ as an ordinary average of the ϕ_k :

$$\Phi := \frac{1}{m} \sum_{k=0}^{m-1} \phi_k. \quad (7.1)$$

However, as we mentioned above, we do not expect the transformation ϕ_k to be an accurate estimation of the actual optimal transformation Φ for large values of k . Thus, a second option would be to define Φ as a weighted average of the ϕ_k .

$$\Phi := \frac{1}{m} \sum_{k=0}^{m-1} a_k \phi_k, \quad (7.2)$$

where the weights a_k are appropriately chosen non-negative real numbers. We will consider these definitions in more detail when we present our results in Section 8.

7.2

In our second multiscale registration algorithm, we register the k^{th} component of image B with the k^{th} component of image A, for $k = 0, 1, 2, \dots, m-1$, as illustrated in the following schematic:

Let ψ_k denote the optimal transformation produced by the registration algorithm upon registering $C_k(B)$ with $C_k(A)$, $k = 0, 1, \dots, m-1$. As before, we expect that registration of $C_k(B)$ with $C_k(A)$ should give an improvement compared to ordinary registration for the first few values of k . As k increases, however, we expect that eventually the components $C_k(A)$ and $C_k(B)$ will become too noisy to give successful registration. Since this algorithm considers components of both images, we expect that it will be particularly successful in the case in which both images are noisy.

Finally, we define the optimal transformation Ψ that should bring image B into spatial alignment with image A using either an ordinary average:

$$\Psi := \frac{1}{m} \sum_{k=0}^{m-1} \psi_k, \quad (7.3)$$

or a weighted average:

$$\Psi := \frac{1}{m} \sum_{k=0}^{m-1} b_k \psi_k, \quad (7.4)$$

where the weights b_k are appropriately chosen non-negative real numbers.

Fixed Image	Mutual information			Mean squares			Normalized correlation		
	ϕ_X	ϕ_Y	n	ϕ_X	ϕ_Y	n	ϕ_X	ϕ_Y	n
Noisy image $I_{0.70}$	4.57	5.17	200	2.08	1.14	7	4.08	0.24	7
$C_0(I_{0.70})$	12.65	16.36	200	3.08	1.11	12	3.11	0.17	9
$C_1(I_{0.70})$	12.69	16.78	200	2.08	3.08	14	2.13	2.12	12
$C_2(I_{0.70})$	12.56	16.79	200	2.11	3.08	14	2.14	3.11	15
$C_3(I_{0.70})$	12.53	16.76	200	3.08	2.11	14	3.11	2.14	7
$C_4(I_{0.70})$	12.48	16.76	200	24.88	1.16	36	18.86	1.18	30
$C_5(I_{0.70})$	12.46	16.78	200	40.80	1.07	52	0.21	1.18	11
$C_6(I_{0.70})$	12.43	16.80	200	28.86	0.15	46	27.84	2.19	42
$C_7(I_{0.70})$	12.43	16.79	200	-2.87	4.11	15	0.18	3.14	12
$C_8(I_{0.70})$	12.43	16.74	200	25.89	3.12	40	-1.84	4.12	14
$C_9(I_{0.70})$	9.33	9.41	200	6.05	4.12	12	7.99	2.08	16
$C_{10}(I_{0.70})$	8.44	8.32	200	-3.92	8.12	21	4.09	3.15	16
$C_{11}(I_{0.70})$	6.96	6.46	200	8.97	6.13	13	3.65	1.17	27

Table 3: This table illustrates the registration results upon registering the translated image T with the k^{th} component $C_k(I_{0.70})$ of the noisy image $I_{0.70}$ obtained via the multiscale decomposition discussed in Section 6. Here, we use $m = 12$ hierarchical steps to decompose the noisy image, so we perform $m = 12$ registration simulations. The transformation parameters ϕ_X and ϕ_Y are the X- and Y-translation parameters of the optimal transformation ϕ produced by the registration algorithm. Recall that the actual translation values are 13 in X and 17 in Y. The moving image in all simulations is the translated image T. The moving image in each case is the translated image T.

8 Multiscale registration results

8.1 Noisy fixed image

In this section, we use the multiscale registration technique described in Section 7 to register the translated (non-noisy) image T with the noisy image $I_{0.70}$. Recall that $I_{0.70}$ is the image obtained upon adding impulse noise of density 0.70 to the brain proton density slice image I. As before, let $C_k(I_{0.70})$ denote the k^{th} component in the multiscale decomposition of $I_{0.70}$, for $k = 0, 1, \dots, m$, obtained as in Section 7. We perform the multiscale decomposition using $m = 12$ hierarchical steps, $\lambda_0 = 0.01$, and $\lambda_j = \lambda_0 2^j$. In the table below, we present the results of $m = 12$ registration simulations, obtained upon registering T with $C_k(I_{0.70})$, $k = 0, 1, \dots, 11$. For each registration, we let ϕ denote the optimal transformation produced by the registration algorithm, and we let ϕ_X and ϕ_Y the X- and Y-translation parameters of the optimal transformation ϕ . The moving image in each registration is the translated image T. For reference, we also include in the first line of Table 3 the parameters obtained using ordinary registration.

To provide an estimation of the optimal transformation Φ that should bring the translated image T into alignment with the noisy image $I_{0.70}$, we first compute an ordinary average as described in Equation (7.1). Letting Φ_X and Φ_Y denote the corresponding X- and Y-translation parameters of the average Φ , we obtain:

It is clear from the results presented in Table 3, however, that a weighted average as constructed in Equation 7.2 is more appropriate. In particular, we see that the parameters produced by mutual information registration are clustered around 12.5 units in X and 16.8 units in Y for $k = 0, 1, \dots, 8$, but then are significantly different for the remaining values of k . We expected that the multiscale registration

	Mutual information	Mean squares	Normalized correlation
Φ_X	11.45	11.6	6.29
Φ_Y	14.02	3.11	2.05

Table 4: This table gives the translation parameters Φ_X and Φ_Y obtained by computing the ordinary average of the multiscale registration transformations ϕ_k for $k = 0, 1, \dots, 11$, as described in Equation (7.1). Recall that the actual translation values are 13 in X and 13 in Y.

Mutual information	
Φ_X	12.52
Φ_Y	16.73

Table 5: In this table, we compute the weighted average of the multiscale registration transformations ϕ_k for $k = 0, 1, \dots, 11$ for mutual information registration. We thus obtain the corresponding X- and Y-translation parameters of the transformation Φ defined as in Equation (7.1). Recall that the actual translation values are 13 in X and 17 in Y.

results would be an accurate approximation of the actual transformation Φ for small values of k , but then would deviate as k became sufficiently large, because as k becomes large, increasing scales of detail (and hence, noise) appear in the component C_k . Thus, even without knowing the actual values of the X- and Y-translations, it makes sense to consider in the weighted average for mutual information only the parameters corresponding to the first 9 registrations ($k = 0, 1, \dots, 8$). We define the weights $a_k = 1$ for $k = 0, 1, \dots, 8$ and $a_k = 0$ for $k \geq 9$. In Table 5, we give the resulting X- and Y-translation parameters. Since the actual values are 13 in X and 17 in Y, we see that multiscale mutual information registration produced very accurate results in this case, and indeed is a significant improvement compared to ordinary registration as well as to classical denoising followed by registration.

Note that we could use more sophisticated techniques for determining the weights a_k . For example, we could perform a statistical analysis on the parameters given by the ϕ_k , and compute the weights a_k according to the mean and standard deviation. Finally, we see that the parameters produced by the mean squares and normalized correlation registrations, however, do not cluster around a single value. In these cases, the registration algorithm did not produce a meaningful result.

Next, we provide the results obtained upon registering the multiscale components of the translated image T with the multiscale components of the noisy image $I_{0.70}$. Let $C_k(T)$ and $C_k(I_{0.70})$ denote the multiscale components of T and $I_{0.70}$, respectively, obtained via the multiscale decomposition presented in Section 6. As before, we use $m = 12$ hierarchical steps, $\lambda_0 = 0.01$, and $\lambda_j = \lambda_0 2^j$ to perform the decomposition. In Table 6, we present the results of $m = 12$ registration simulations, obtained upon registering $C_k(T)$ with $C_k(I_{0.70})$, $k = 0, 1, \dots, 11$. For each registration, we let ψ denote the optimal transformation produced by the registration algorithm, and we let ψ_X and ψ_Y denote the X- and Y-translation parameters of the optimal transformation ψ . For reference, we also include in the first line of Table 6 the parameters obtained using ordinary registration.

The results in Table 6 indicate that a weighted average as constructed in Equation (7.4) is the most appropriate method for estimating the optimal transform parameters Ψ_X and Ψ_Y . Recall that we expect the multiscale registration algorithm to work well for the first few values of k , and then to eventually become less accurate as increasing levels of detail and noise appear in the k^{th} component C_k . Indeed, for mutual information registration, we see that the parameters ψ_X and ψ_Y are clustered together for $k = 0, 1, \dots, 8$, and then deviate for $k \geq 9$, so we set the weights $a_k = 1$ for $k = 0, 1, \dots, 8$ and $a_k = 0$ for $k \geq 9$. For both mean squares and normalized correlation, we set the weights $b_k = 1$ for $k = 0, 1$ and $b_k = 0$ for $k \geq 1$. In Table 7, we present the X- and Y-translation values corresponding to the weighted average Ψ .

Fixed Image	Moving Image	Mutual information			Mean squares			Normalized correlation		
		ψ_X	ψ_Y	n	ψ_X	ψ_Y	n	ψ_X	ψ_Y	n
$I_{0.70}$	T	4.57	5.18	200	2.08	1.14	13	4.08	0.24	7
$C_0(I_{0.70})$	$C_0(T)$	12.69	16.66	200	12.29	17.72	21	12.96	17.08	17
$C_1(I_{0.70})$	$C_1(T)$	12.67	16.87	200	13.70	17.75	38	12.99	17.67	16
$C_2(I_{0.70})$	$C_2(T)$	12.59	16.86	200	20.77	5.20	38	16.84	4.31	17
$C_3(I_{0.70})$	$C_3(T)$	12.55	16.82	200	3.19	0.31	12	4.20	4.23	11
$C_4(I_{0.70})$	$C_4(T)$	12.52	16.83	200	2.20	2.24	12	26.74	5.18	36
$C_5(I_{0.70})$	$C_5(T)$	12.51	16.84	200	31.65	2.23	42	14.90	6.27	58
$C_6(I_{0.70})$	$C_6(T)$	12.49	16.87	200	30.69	6.16	50	19.87	4.29	28
$C_7(I_{0.70})$	$C_7(T)$	12.48	16.85	200	33.64	3.16	46	29.64	3.32	37
$C_8(I_{0.70})$	$C_8(T)$	12.53	16.71	200	28.81	3.22	45	1.26	1.29	11
$C_9(I_{0.70})$	$C_9(T)$	9.26	9.36	200	2.13	3.13	11	17.93	3.21	71
$C_{10}(I_{0.70})$	$C_{10}(T)$	8.80	8.61	200	2.12	3.12	11	32.63	3.14	39
$C_{11}(I_{0.70})$	$C_{11}(T)$	6.95	6.34	200	34.74	2.10	42	4.13	5.08	17

Table 6: This table illustrates the registration results upon registering the k^{th} multiscale component $C_k(T)$ of the translated image T with the k^{th} multiscale component $C_k(I_{0.70})$ of the noisy image $I_{0.70}$ obtained via the multiscale decomposition discussed in Section 6. Here, we use $m = 12$ hierarchical steps to decompose the noisy image, so we perform $m = 12$ registration simulations. The transformation parameters ψ_X and ψ_Y are the X- and Y-translation parameters of the optimal transformation ψ produced by the registration algorithm. Recall that the actual translation values are 13 in X and 17 in Y.

	Mutual information	Mean squares	Normalized correlation
Ψ_X	12.56	12.99	12.98
Ψ_Y	16.82	17.74	17.37

Table 7: This table gives the translation parameters Ψ_X and Ψ_Y obtained by computing the weighted average of the multiscale registration transformations ψ_k for $k = 0, 1, \dots, 11$, as described in Equation (7.4). Recall that the actual translation values are 13 in X and 17 in Y.

Since the actual translation values are 13 in X and 17 in Y, we see that the component-wise multiscale registration of the translated image T with the noisy image $I_{0.70}$ produces very accurate results for each of the three methods presented here (mean squares, normalized correlation, and mutual information).

8.2 Noisy fixed and moving images

In this section, we consider the registration problem in which both the fixed and moving images are noisy. Consider the noisy images $I_{0.40}$ and $T_{0.40}$, where T, as before, is the result of translating I 13 units in X and 17 units in Y, and A_δ denotes the image obtained by adding impulse noise of density δ to the image A.

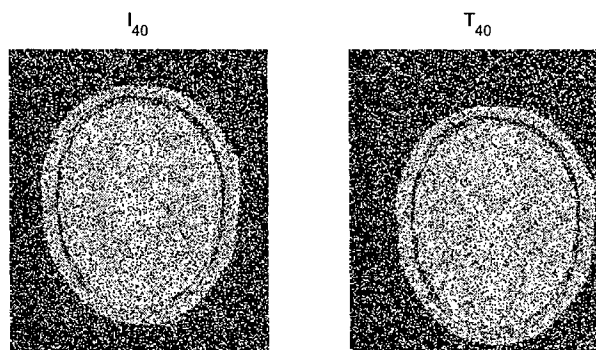


Figure 8: Original image I and translated image T with impulse noise of density $\delta = 0.40$

Before applying our multiscale registration algorithm, we attempt to register the noisy translated image $T_{0.40}$ with the noisy image $I_{0.40}$ using the three registration methods mean squares, normalized correlation, and mutual information. For each registration method, we denote by ϕ the optimal transformation produced by the registration, and we denote by ϕ_X and ϕ_Y the X- and Y-translation parameters of the optimal transformation ϕ . As is seen in the table below, registration of the noisy images fails.

Since ordinary registration of the noisy images fails, we register the images using our multiscale registration technique. First, we perform the multiscale decomposition discussed in Section 6 to both of the noisy images, again using $k = 12$ hierarchical steps, initial scale $\lambda_0 = 0.01$, and $\lambda_j = 2^j \cdot \lambda_0$. Let $C_k(I_{0.40})$ and $C_k(T_{0.40})$ denote the k^{th} component in the multiscale decomposition of $I_{0.40}$ and $T_{0.40}$, respectively. Since both of the images are noisy, we register the k^{th} component $C_k(T_{0.40})$ with the k^{th} component $C_k(I_{0.40})$. For each registration simulation, we denote by ψ the optimal transformation produced by the registration algorithm, and we denote by ψ_X and ψ_Y the corresponding X- and Y-translation parameters of the optimal transformation ψ .

The multiscale registration results in Table 9 indicate that a weighted average as constructed in Equation (7.2) is the most appropriate method for estimating the optimal transform parameters Ψ_X and Ψ_Y . For mutual information, we set the weights $b_k = 1$ for $k = 0, 1, \dots, 6$ and $b_k = 0$ for $k \geq 7$. For mean

Registration Method	ϕ_X	ϕ_Y
Mean Squares	11.02	7.04
Normalized Correlation	3.05	0.99
Mutual Information	5.03	2.54

Table 8: This table illustrates the results upon registering the noisy translated image $T_{0.40}$ with the noisy image $I_{0.40}$ using ordinary mean squares, normalized correlation, and mutual information registration techniques. For each registration, we let ϕ denote the optimal transformation produced by the registration algorithm, and we let ϕ_X and ϕ_Y denote the corresponding X- and Y-translation parameters of the optimal transformation ϕ . Recall that the actual translation values are 13 in X and 17 in Y.

Fixed Image	Moving Image	Mutual information		Mean squares		Normalized correlation	
		ψ_X	ψ_Y	ψ_X	ψ_Y	ψ_X	ψ_Y
$I_{0.40}$	$T_{0.40}$	5.03	2.54	11.02	7.04	3.05	0.99
$C_0(I_{0.40})$	$C_0(T_{0.40})$	13.06	16.92	13.05	16.92	13.05	16.92
$C_1(I_{0.40})$	$C_1(T_{0.40})$	13.05	16.93	13.02	16.22	13.06	16.92
$C_2(I_{0.40})$	$C_2(T_{0.40})$	13.03	16.93	8.11	5.29	13.02	16.27
$C_3(I_{0.40})$	$C_3(T_{0.40})$	13.02	16.94	5.40	12.19	13.02	16.25
$C_4(I_{0.40})$	$C_4(T_{0.40})$	13.02	16.94	2.20	8.00	2.23	5.09
$C_5(I_{0.40})$	$C_5(T_{0.40})$	13.01	16.93	26.76	1.21	1.17	7.00
$C_6(I_{0.40})$	$C_6(T_{0.40})$	12.99	16.81	23.83	4.11	1.22	2.17
$C_7(I_{0.40})$	$C_7(T_{0.40})$	7.05	6.08	0.20	3.15	0.20	4.15
$C_8(I_{0.40})$	$C_8(T_{0.40})$	6.78	5.05	6.04	2.09	6.04	6.05
$C_9(I_{0.40})$	$C_9(T_{0.40})$	3.05	1.02	9.98	1.10	5.06	10.01
$C_{10}(I_{0.40})$	$C_{10}(T_{0.40})$	12.20	14.01	-1.97	0.99	-3.93	3.04
$C_{11}(I_{0.40})$	$C_{11}(T_{0.40})$	4.80	3.19	1.01	5.98	3.91	0.72

Table 9: This table illustrates the registration results upon registering the k^{th} multiscale component $C_k(T_{0.40})$ of the noisy translated image T with the k^{th} multiscale component $C_k(I_{0.40})$ of the noisy image $I_{0.40}$ obtained via the multiscale decomposition discussed in Section 6. Here, we use $m = 12$ hierarchical steps to decompose the noisy image, so we perform $m = 12$ registration simulations. The transformation parameters ψ_X and ψ_Y are the X- and Y-translation parameters of the optimal transformation ψ produced by the component-wise multiscale registration algorithm. Recall that the actual translation values are 13 in X and 17 in Y.

	Mutual information	Mean squares	Normalized correlation
Ψ_X	13.03	13.03	13.04
Ψ_Y	16.92	16.57	16.59

Table 10: This table gives the translation parameters Ψ_X and Ψ_Y obtained by computing the weighted average of the multiscale registration transformations ψ_k for $k = 0, 1, \dots, 11$, as described in Equation (7.4). Recall that the actual translation values are 13 in X and 17 in Y.

squares, we set the weights $b_k = 1$ for $k = 0, 1$ and $b_k = 0$ for $k \geq 2$. Finally, for normalized correlation, we set the weights $b_k = 1$ for $k = 0, 1, 2, 3$ and $b_k = 0$ for $k \geq 4$. In Table 10, we present the X- and Y-translation values corresponding to the weighted average Ψ .

Note that since the actual translation values are 13 in X and 17 in Y, our multiscale registration techniques provides accurate results in the case in which both the fixed and moving images contain significant levels of noise. Since both ordinary registration methods as well as denoising techniques failed to produce acceptable registration results, the success of our multiscale technique is an indication of its general applicability and accuracy, particularly for cases in which other methods fail due to the presence of noise.

9 Computation Time

10 Summary

References

- [1] N.M. ALPERT, J.F. BRADSHAW, D. KENNEDY, AND J.A. CORREIA, *The principal axes transformation - A method for image registration*, Journal of Nuclear Medicine. **31**(10) (1990), pp. 1717-1722.
- [2] M. BRO-NIELSEN AND C. GRAMKOW, *Fast fluid registration of medical images*, Lecture Notes in Computer Science, 1131, 267-276, Springer, Berlin and Heidelberg, 1996.
- [3] C. BROIT, *Optimal Registration of Deformed Images*, Ph.D. thesis, Computer and Information Science, University of Pennsylvania, 1981.
- [4] A. COLLIGNON, D. VADERMEULEN, P. SUTENS, AND G. MARCHAL, *3d multi-modality medical image registration based on information theory*, Computational Imaging and Vision, vol. 3, pp. 263-274, 1995.
- [5] R. DUDA AND P. HART, *Pattern Classification and Scene Analysis*, John Wiley and Sons, New York, 1973.
- [6] , C. L. EPSTEIN, *Introduction to the Mathematics of Medical Imaging*, Pearson Education, Inc., New Jersey, 2003.
- [7] B. FISCHER AND J. MODERSITZKI, *Fast inversion of matrices arising in image processing*, Numerical Algorithms, vol. 22, pp. 1-11, 2001.
- [8] W.A. LIGHT, *Variational methods for interpolation, particularly by radial basis functions*, Numerical Analysis. pp. 94-106, 1995.

- [9] F. MAES, A. COLLIGNON, D. VANDERMEULEN, G. MARCHAL, AND P. SUETENS, *Multimodality image registration by maximization of mutual information*, IEEE Transactions on Medical Imaging, vol. 16, no. 2, pp. 187-198, 1997.
- [10] Y. MEYER, *Oscillating Patterns in Image Processing and Nonlinear Evolution Equations*, University Lecture Series 22, AMS, Providence, RI, 2002.
- [11] J. MODERSITZKI, *Numerical Methods for Image Registration*, Oxford, 2004.
- [12] G. P. PENNEY, J. WEESE, J. A. LITTLE, P. DESMEDT, D.L.G. HILL, AND D.J. HAWKES, *A comparison of similarity measures for use in 2D-3D medical image registration*, IEEE Transactions on Medical Imaging, vol. 4, pp. 586-595, 1999.
- [13] T. M. PETERS, B. L. K. DAVEY, P. MUNGER, R. M. COMEAU, A. EVANS, AND A. OLIVER, *Three-dimensional multi-modal image-guidance for neurosurgery*, IEEE Transactions on Medical Imaging, vol. 15, no. 2, pp. 121-128, 1996.
- [14] J. P. W. PLUIM, J. B. A. MAINTZ, AND M. A. VIERGEVER, *Image registration by maximization of combined mutual information and gradient information*, IEEE Transactions on Medical Imaging, vol. 19, no. 8, pp. 809-814, 2000.
- [15] J. P. W. PLUIM, J. B. A. MAINTZ, AND M. A. VIERGEVER, *Mutual information based registration of medical images: a survey*, IEEE Transactions on Medical Imaging, vol. 22, no. 8, pp. 986-1004, 2003.
- [16] K. ROHR, *Landmark-based image analysis*, Computational Imaging and Vision, Kluwer Academic, Dordrecht, 2001.
- [17] L. RUDIN AND V. CASELLES, *Image recovery via multiscale total variation*, Proceedings of the Second European Conference on Image Processing, Palma, Spain, 1995.
- [18] L. RUDIN, S. OSHER, AND E. FATEMI, *Nonlinear total variation based noise removal algorithms*, Physica D, vol. 60, pp. 259-268, 1992.
- [19] E. TADMOR, S. NEZZAR, AND L. VESE, *A multiscale image representation using hierarchical (BV, L^2) decompositions*, Multiscale Modeling and Simulations, vol. 2, no. 4, pp. 554-579, 2004.
- [20] P. THÉVENAZ AND M. UNSER, *Optimization of mutual information for multiresolution image registration*, IEEE Transactions on Image Processing, vol. 9, no. 12, pp. 2083-2099, 2000.
- [21] P. VIOLA, W. WELLS, H. ATSUMI, S. NAKAJIMA, AND R. KIKINIS, *Multi-modal volume registration by maximization of mutual information*, Medical Image Analysis, vol. 1, no. 1, pp. 35-51, 1995.
- [22] J. WEST, J. M. FITZPATRICK, Y. WANG, B. M. DAWANT, C. R. MAUER, JR., R. M. KESSLER, R. J. MACIUNAS, C. BARILLOT, D. LEMOINE, A. COLLIGNON, F. MAES, P. SUETENS, D. VANDERMEULEN, P. A. VAN DEN ELSSEN, S. NAPEL, T. S. SUMANAWEEERA, B. HARKNESS, P. F. HEMLER, D. L. G. HILL, D. J. HAWKES, C. STUDHOLME, J. B. A. MAINTZ, M. A. VIERGEVER, G. MALANDAIN, X. PENNEC, M. E. NOZ, G. Q. MAGUIRE, JR., M. POLLACK, C. A. PELIZZARI, R. A. ROBB, D. HANSON, AND R. P. WOODS, *Comparison and evaluation of retrospective intermodality brain image registration techniques*, Journal of Computer Assisted Tomography, vol. 21, no. 4, pp. 554-566, 1997.

Overview of Image Guided Radiation Therapy

L. Xing, B. Thorndyke, E. Schreibmann, Y. Yang, T. Li, G.Y. Kim, G.
Luxton, and A. Koong

Department of Radiation Oncology, Stanford University School of Medicine, Stanford,
California 94305-5847

Contact information:

Stanford University School of Medicine
Department of Radiation Oncology
875 Blake Wilbur Drive
Stanford, CA 94305-5847
E-mail: lei@reyes.stanford.edu
Phone: (650) 498 7896
Fax: (650) 498 4015

Invited review for a special issue of Medical Dosimetry on IGRT

1. Introduction

Radiotherapy is an image-guided intervention and imaging is involved in every key step of the process, ranging from patient staging, simulation, treatment planning, and radiation delivery to patient follow up (see figure 1). The evolution of radiation therapy has been strongly correlated with the development of imaging techniques. During the early days when Roentgen first discovered x-rays, two-dimensional (2D) transmission images of the human body provided unprecedented imagery of bony landmarks which allowed radiologists to deduce the location of internal organs. Using planar radiographs, radiologists planned cancer treatments by collimating rectangular fields that circumscribed the presumed tumor location. Additional blocks placed daily to match marks on the patient's skin, and later using low-temperature melting dense alloys. The emergence of computed tomography (CT) in the 1970s revolutionized radiation therapy and allowed us to use image data to build a 3D patient model and design 3D conformal radiation treatment. In general, 3D conformal radiation therapy (3D CRT) is a method of irradiating a tumor target volume defined in a 3D anatomical image of the patient with a set of x-ray beams individually shaped to conform to the 2D beam's eye view (BEV) projection of the target. The reduction in normal tissue irradiation when moving from 2D to 3D should theoretically improve the therapeutic ratio and allow the tumor target volume to be treated to a higher dose, thereby improving the probability of tumor control. Recent technical advances in planning and delivering intensity modulated radiation therapy (IMRT) provide an unprecedented means for producing exquisitely shaped radiation doses that closely conform to the tumor dimensions while sparing sensitive structures¹⁻³. The development of 3D CRT and IMRT places more stringent requirements on the accuracy of beam targeting. In practice, large uncertainties exist in tumor volume delineation and in target localization due to intra- and inter-organ motions. The utility of modern radiation technologies, such as 3D CRT and IMRT, cannot be fully exploited without eliminating or significantly reducing these uncertainties. The need to improve targeting in radiation treatment has recently spurred a flood of research activities in image-guided radiation therapy (IGRT).

While all radiation therapy procedures are image guided *per se*, traditionally, imaging technology has primarily been used in producing 3D scans of the patient's anatomy to identify the location of the tumor prior to treatment. The verification of a treatment plan is typically done at the level of beam portals relative to the patient's bony anatomy before patient treatment. In current literature, the term of IGRT or IG-IMRT is employed loosely to refer to newly emerging radiation planning, patient setup and delivery procedures that integrate cutting-edge image-based tumor definition methods, patient positioning devices and/or radiation delivery guiding tools. These techniques combine new imaging tools, which interface with the radiation delivery system through hardware or software, and state-of-the-art 3D CRT or IMRT, and allow physicians to optimize the accuracy and precision of the radiotherapy by adjusting the radiation beam based on the true position of the target tumor and critical organs. With IGRT, it is also possible to take tumor motion into account during radiation therapy planning and treatment. Because IGRT improves precision, it raises the possibility of shortening the duration of radiation therapy by reducing the number of treatment sessions for some forms of cancer.

The purpose of this article is to highlight the recent developments of various available imaging techniques and present an overview of IGRT. Stanford experience on various aspects of clinical IGRT will also be presented. After reading this article, it is hoped that the readers will have an overall picture of IGRT and find it easier to navigate themselves through the subsequent articles in

this issue, which focus on providing technical details and/or specific clinical applications of the available IGRT tools.

2. Issues in IGRT

In current 3D CRT or IMRT, uncertainties exist in many circumstances, such as tumor target definition, patient immobilization and patient breathing motion, which make it difficult to administer a high radiation dose to the planned location. The exact locations of the boundaries of the tumor target and the adjacent sensitive structures are often not known precisely, and a population- and disease site-based safety margin is used routinely to cope with a problem that is otherwise insoluble. An important task of IGRT is to eliminate or significantly reduce the margins involved in defining the clinical and planning target volume (CTV and PTV, respectively).

Many IGRT solutions have been proposed to attack various aspects of the problem. Briefly, IGRT developments are focused in four major areas: (1) biological imaging tools for better definition of tumor volume; (2) time-resolved (4D) imaging techniques for modeling the intra-fraction organ motion; (3) on-board imaging system or imaging devices registered to the treatment machines for inter-fraction patient localization; and (4) new radiation treatment planning and delivery schemes incorporating the information derived from the new imaging techniques. These are discussed in more detail in the following.

3. Tumor target volume definition

3.1 CT, MRI, and ultrasound (US) imaging techniques

To be able to 'see' the extent of disease more clearly and define the tumor target volume relative to the patient's anatomy have been among the most important issues in radiation oncology. CT has played a pivotal role in the process. Many radiation oncology departments have acquired dedicated CT scanners. A typical patient's 3D CT data set has more than 100 axial slices, each of which contains 512×512 pixels. With 16 bits per pixel, a CT data set can easily run over 50 megabytes. CT has many advantages, including high spatial integrity, high spatial resolution, excellent bony structure depiction, and the ability to provide relative electron density information used for radiation dose calculation. The recent development of ultra-fast multi-slice CT has opened a new dimension to CT technology and allows time-resolved (4D) CT imaging of patient's cardiac and breathing cycles. Using array detectors, multisection CT scanners can acquire multiple slices or sections simultaneously and thereby greatly increase the speed of CT image acquisition. Currently, all manufactures are moving toward 8-, 16- and even 32-slice CT technology. Radiation oncology application of 4D CT will be discussed in Sec. 4.1.

MRI provides superior soft tissue discrimination, especially for CNS structures and within the abdomen and pelvis, and has been widely used in the diagnosis and tumor delineation. MRI is also utilized for virtual simulation of radiation treatment for some specific disease sites. Physically, MRI involves the determination of the bulk magnetization of nuclei within a given voxel through use of radio-frequency (RF) radiation and magnetic fields. In a clinical setting, MRI is typically employed together with CT images with the help of image fusion software to delineate the extent of the malignancy. As with other imaging techniques, MR technology has gone through a series of revolutions in the past three decades. MRI technology is moving toward higher field strengths to further improve the quality of MR images, as evidenced by the installations of 3T scanners in many institutions (9.4 T MRI scanners has been installed in a few institutions). Fast cine MRI is also becoming increasingly available and may offer physicians an alternative for imaging the temporal

process of patient breathing or even heart beating. Figure 2 shows an example of MRI images acquired at two different phases for a liver cancer patient. In addition, the development of some specialized MRI scans has also attracted much attention. These include diffusion and perfusion MRI, dynamic contrast MRI, MR angiography, MR spectroscopic imaging (MRSI) and functional MRI (fMRI). The recent development of diffusion tensor imaging (DTI), for instance, enables diffusion to be measured in multiple directions and the fractional anisotropy in each direction to be calculated for each voxel. fMRI measures signal changes in the brain that are due to changing neural activity. These techniques enable researchers to make axonal and functional maps to examine the structural connectivity of different regions in the brain and may allow better definition of brain tumors and better sparing of sensitive regions⁴.

Ultrasound (US) is another useful imaging modality for radiation therapy. US utilizes high frequency (1~10 MHz) sound waves to generate anatomical images which have high spatial resolution and tissue characterization discrimination power through image texture analysis. In radiation therapy, it has been particularly useful in prostate imaging. Transrectal US permits an examination/localization of the prostate gland⁵⁻⁸ and is the imaging modality of choice in guiding the prostate seed implant procedure.

3.2 Biological imaging

Regardless of the course of therapy, current standard imaging modalities such as CT and MRI do not always provide an accurate picture of the tumor extent, especially in the zone of infiltration that may be the limiting factor in an attempt of a radical treatment approach. This has been shown to be the case for gliomas before surgical intervention^{9, 10}. It is also true when attempting to determine the volume of residual tumor for additional therapy owing to problems in differentiating post-therapy changes from residual tumor. Indeed, the above-mentioned imaging modalities are anatomic in nature, i.e., they provide snapshot of a patient's anatomy without biological information of various organs or structures. Biological imaging, defined as the *in vivo* characterization and measurement of biological processes at the cellular and molecular level, is an emerging multidisciplinary field resulting from the developments of molecular biology and diagnostic imaging and shows significant promise to revolutionize cancer detection, staging/re-staging, treatment decision-making, and assessment of therapeutic response. MRSI and positron emission tomography (PET) are two valuable modalities for radiation therapy planning. ¹H MRSI combines the advantages of obtaining biochemical data by water-suppressed ¹H MR spectroscopy with the spatial localization of that data. MR spectroscopy is useful in characterization of brain and prostate tumors. In the brain, for example, malignant tumors have an increased rate of membrane turnover (increased level of choline) and a decreased concentration of neurons. Furthermore, spectroscopy allows for the non-invasive monitoring of the response of residual tumor to therapy and for differentiating tumor recurrence from tissue necrosis. Recently, Pirzkall et al^{11, 12} have applied multi-voxel MRSI to assess the impact of MRSI on the target volumes used for radiation therapy treatment planning for high-grade gliomas. It was found that, although T₂-weighted MRI estimated the region at risk of microscopic disease as being as much as 50% greater than by MRSI, metabolically active tumor tissue still extended outside the T₂ region in 88% of patients by as much as 28mm. In addition, T₁-weighted MRI suggested a lesser volume and different location of active disease compared to MRSI. The discordance of high grade glioma target volumes resulting from MRI was also observed in other functional imaging modalities such as PET and SPECT.

While there is a growing body of evidence now indicating that *in vivo* MRSI provides unique information on metabolism that will ultimately affect clinical diagnosis, choice and monitoring of

therapies, and treatment planning, in reality, MRSI has been mainly remained a research tool confined to a small number of academic institutions¹³⁻¹⁸. PET, on the other hand, is more widely used and has been harnessed into the planning process in many clinics. In general, PET has lower image resolutions than CT images and, with commonly used FDG tracer, contains no anatomic information about normal structures. Information derived from PET needs to be fused with the corresponding CT images for treatment planning. The fusion of PET and CT images are simplified with the use of the hybrid PET/CT scanner^{19, 20}. Figure 3 shows the data flow of a typical PET/CT scanner. Hybrid PET/CT systems have several positive features that are absent in stand-alone PET and CT units. PET/CT is a hardware-based image-fusion technology that virtually eliminates the uncertainty and inconvenience of currently available software fusion of separate PET and CT images, which are often acquired with patients in different positions. It should be emphasized that the PET/CT unit is not simply a PET and CT combination: Not from the perspective of system design, nor the practical utility. Other than the fact that one does not have to go through the cumbersome and time consuming software fusion process, it has the advantages of simultaneous availability of the fused images, convenience to the patient and the physician, increased physician confidence in interpreting the image findings, and ~30% of reduction in PET scanning time due to the use of CT data for PET attenuation correction.

3.3 Integration of biological imaging techniques and *multimodality image fusion*

FDG-PET provides a means to study metabolic activity of tumors *in vivo*. Initial studies incorporating FDG-PET into treatment planning have been reported²¹⁻²⁴. Bradley et al^{23, 24} have carried out a prospective study to determine the impact of functional imaging with FDG-PET on target volumes among non-small cell lung cancer (NSCLC) patients being considered for definitive radiation therapy. They found that radiation targeting with fused FDG-PET and CT images resulted in alterations in radiation therapy planning in over 50% of patients by comparison with CT targeting. The changes included the alterations in the AJCC TNM stage (31% of the patients studied) and modification of target volume (58% of the patients studied). In a separate study, MacManus *et al.*²² reported that 30% of patients with locally advanced NSCLC became ineligible for curative radiotherapy because of detection of either distant metastatic disease or intrathoracic disease too extensive for radical radiation. Recently, Howard et al²⁵ have studied the value of FDG-PET/CT for esophagus cancer and similar findings were reported.

3.4 *Emerging PET tracers for oncologic imaging*

While FDG-PET has been shown to be effective for a number of malignancies, imaging of many other neoplasms, such as breast cancer and prostate cancer, with FDG has shown less success.²⁶⁻²⁹ Many pitfalls have previously been described with FDG-PET imaging. The FDG tracer can be non-specifically taken up by several benign conditions such as inflammatory disease, pneumonia, brown fat, muscle, bowel uptake, and granulomatous disease. Also, slow growing indolent tumors may exhibit only a mild increase in glucose metabolism and therefore be missed by FDG-PET³⁰⁻³⁴. Thus FDG-PET is only minimally useful for the evaluation of indolent tumors such as organ-confined prostate cancer. The recent development of [¹⁸F]fluorothymidine (FLT)^{35, 36} provided a new opportunity to improve the sensitivity and specificity of PET imaging of cancer. Because there is upregulation of thymidine transport into malignant cells due to accelerated deoxyribonucleic acid synthesis, either ¹¹C or ¹⁸F-labeled thymidine radiotracers can be used to determine cellular proliferation. Several studies have shown that the accumulation of FLT correlates better with proliferation in comparison with the commonly used FDG tracer^{35, 36 37}. Recently, Smyczek-Gargya

*et al.*³⁸ have reported FLT-PET imaging experiments involving 12 patients with 14 primary breast cancer lesions (T2-T4). Thirteen of the 14 primary tumors demonstrated focally increased FLT uptake. The study showed that FLT-PET is suitable for the diagnosis of primary breast cancer and locoregional metastases and the high image contrast of the technique may facilitate the detection of small foci.

Agents, such as antisense molecules, aptamers, antibodies, and antibody fragments, can be aimed at molecular targets for biological imaging. Tumor receptors and certain cellular physiologic activities, including metabolism, hypoxia, proliferation, apoptosis, angiogenesis, and infection, provide such targets. In addition to FLT, there are several other new nuclide imaging tracers under clinical or laboratory investigations^{30, 39-46}, which include, to name a few, ¹¹C-Acetate⁴⁷⁻⁵⁰, ¹⁸F-choline^{51, 52}, ¹¹C-choline⁵³⁻⁵⁵, ⁶⁴Cu-DOTA-[Lys3]Bombesin⁵⁶, ¹⁸F-FMISO⁵⁷⁻⁵⁹, ¹⁸F-FAZA⁶⁰, ⁶⁴Cu-ATSM⁶¹. For example, carcinogenesis is often characterized by enhanced cell proliferation and transformation and elevated levels of choline and choline kinase activity in certain neoplastic diseases have motivated the development of positron-labeled choline analogs for noninvasive detection of cancer using PET^{53, 62}. Choline acts as a precursor for the biosynthesis of phospholipids, e.g. phosphatidylcholine, the major components of cell membrane⁶³. Several preliminary studies have demonstrated the potential of the new tracer for prostate cancer and many other cancers^{49, 53, 55, 62, 64, 65}.

3.5 Biologically conformal radiation therapy (BCRT)

The current 3D CRT or IMRT inverse planning is typically aimed at producing a homogeneous target dose under the assumption of uniform biology within the target volume. In reality, it is well known that the spatial biology distribution (e.g., clonogen density, radiosensitivity, tumor proliferation rate, functional importance) in most tumors and sensitive structures is heterogeneous. Recent progress in biological imaging is making the mapping of this distribution increasingly possible. This new development opens a new avenue of research, coined BCRT⁶⁶⁻⁷⁰. The goal of BCRT is to take the inhomogeneous biological information derived from biological imaging into account and to produce customized nonuniform dose distributions on a patient specific basis. The simultaneous integrated boost (SIB) to elective volumes recently appearing in the literature represents a simple example of BCRT.

To establish BCRT, three major aspects must be addressed: (i) Determination of the distribution of biological properties of the tumor and critical structures; (ii) Prescription of the desired dose distribution for inverse planning; and (iii) Inverse planning to generate most faithfully the prescribed nonuniform dose distribution. While the development of molecular imaging techniques is critically important in mapping out biology distributions, the successful integration of this information into IMRT planning through steps (ii) and (iii) is also indispensable to fully exploit the obtained biology information to improve patient care. With the optimistic assumption that spatial biology distributions within a patient can be reliably determined using biological imaging in the future, Yang and Xing⁷⁰ have established a theoretical framework to quantitatively incorporate the spatial biology data into IMRT inverse planning. In order to implement this method, they first derived a general formula for determining the desired dose to each tumor voxel for a known biology distribution of the tumor based on a linear-quadratic (LQ) model. By maximizing the *TCP* under the constraint of constant integral target dose, they obtained

$$D_0^T(i) = \frac{\alpha'_{ref}}{\alpha'_i} D_{ref} - \frac{1}{\alpha'_i} (\gamma_{ref} - \gamma_i) \Delta T - \frac{1}{\alpha'_i} \ln \left(\frac{\alpha'_{ref} \rho_{ref}}{\alpha'_i \rho_i} \right), \quad (1)$$

where $D_0^T(i)$ is the desirable prescription dose at the voxel i with the tumor cell density, radiosensitivity and proliferation rate given by $(\rho_i, \alpha_i, \gamma_i)$, and D_{ref} is the reference dose for the voxel with reference radiobiological parameters $(\rho_{ref}, \alpha_{ref}, \gamma_{ref})$. For a given disease site, the radiation dose used in current clinical practice with “intent to cure” can be used as a good starting point in selecting the value of D_{ref} . The relation is quite general and can be used as prescription dose to guide an arbitrary inverse planning objective function aimed at producing a customized dose distribution in accordance with the spatial biology information.

4 Intra-fraction organ motion: managing the respiratory motion

Components affecting the reproducibility of target position during and between subsequent fractions of radiation therapy include the displacement of internal organs between fractions and internal organ motion within a fraction. Depending on the disease site, these components contribute differently to the margins that are to be added around the CTV to ensure adequate coverage. In the thorax and abdomen, intra-fraction internal anatomy motion due to respiration is a principal cause for large safety margins. Motion can distort target volumes and result in positioning errors as different parts of the tumor move in and out of the image window with the patient’s breathing cycle. Several studies, conducted to examine the extent of diaphragm excursion due to normal respiration, reported the range of motion from ~0.5 to 4.0 cm in the superiorinferior direction. As a consequence of a significant margin added around the CTV, a large amount of normal tissue surrounding the CTV is irradiated. Accounting for such motion during treatment has the potential to reduce margins, leading to reduced radiation toxicity and risk of treatment-induced complications, and yielding room for dose escalation.

A complete solution compensating for respiratory motion should ideally start at the simulation stage. There have been several studies to characterize the amplitude, phase and periodicity of organ motion⁷¹⁻⁷⁵ using fluoroscopic x-rays, ultrasound^{76, 77}, and magnetic or RF markers^{78, 79}. The development and deployment of spiral and multi-detector CT scanners have made practical the acquisition of time-resolved or 4D CT images. The reconstructed images acquired with patients in treatment positions provide 4D models upon which geometric as well as dosimetric computations can be performed. 4D PET is also becoming clinically available⁸⁰⁻⁸². Treatment-wise, respiratory gating technology and tumor tracking techniques to synchronize delivery of radiation with the patient’s own respiratory cycle are under intensive investigations.

4.1 4D CT Imaging

A 4D CT can be either prospective or retrospective. In the former case, the scanner collects images at only one of the breathing phases of the patient instead of scanning continuously. The retrospective 4D CT scan results in multiple image sets, corresponding to different breathing phases of the patient, and consists of three relatively orthogonal processes⁸³⁻⁸⁷: Recording of respiratory signal(s), acquisition of time-dependent CT projection data, and construction of a 4D image from these data. The first objective can be achieved by tracking a surrogate of respiration-related organ and tumor motion, such as tidal volume measured with a spirometer^{85, 88}, chest expansion monitored by a pneumatic bellows⁸⁹, or a reflecting external marker placed on the abdomen and tracked with a camera⁸³. Time-dependent CT data can be acquired by oversampling in either helical or cine mode, and constructing several CT slices over the full respiratory cycle at each axial location^{86, 90}. Finally, the respiratory signal and CT data must be combined into a 4D series, providing a CT volume at several points throughout the respiratory cycle. In this section, we will focus primarily on the implementation of

4D CT provided by the Varian Real-time Position Management (RPM) camera/software and the GE Discovery ST multislice PET/CT scanner.

4D CT patient setup proceeds along the same lines as a standard 3D CT exam. The patient is immobilized on the scanner bed, and aligned using room and scanner lasers. Sagittal and coronal scout images are used to verify patient positioning, and the setup is adjusted as necessary. At this stage of the setup, the 4D procedure begins to diverge from the 3D exam.

The RPM system consists of an infrared source, CCD camera, and a reflecting block. The block is attached to the patient's abdomen, typically just inferior to the xiphoid process, and the anteroposterior motion of the block is captured by the camera. This motion is analyzed in real-time by Varian software on a computer connected to the RPM camera. The breathing pattern is recorded for the duration of the scan, and is referred to as the "respiratory trace." Once the scan has finished, the software retrospectively computes the phase at each point of the respiratory trace by determining the location of the peaks at end-inspiration, and assigning percentages to interpeak points based on a linear interpolation of the peak-to-peak distance. For example, under this scheme, end-inspiration occurs at 0%, while end-expiration typically appears near 50 – 60%. The peak-to-peak distance can vary between respiratory cycles, as can the position of end-expiration with respect to end-inspiration.

Irregularities in a patient's respiratory pattern can often be reduced by encouraging the patient to breathe calmly and consistently, and then relying on the patient's compliance during the scan. If this free-breathing approach is insufficient, the RPM software can provide audio coaching in the form of a "breathe in, breathe out" recording, which is manually or automatically timed to the patient's natural rhythm. Some groups have used video feedback either alone or concurrently with audio instructions⁹¹. While audio and video coaching can help by stabilizing the respiratory period, amplitude and baseline, they can complicate matters for patients with compromised respiratory function, who find it difficult or impossible to maintain a regular rhythm. Another solution is active breath control (ABC)⁹²⁻⁹⁴, which uses modified ventilator equipment to control the airflow, albeit at the (possibly significant) expense of patient comfort.

Once a sufficiently regular breathing pattern has been established, the CT data is acquired in "cine" mode. This is a step-and-shoot technique, whereby the gantry rotates several times at each bed position in order to acquire data over the full respiratory cycle. The raw data is partitioned into bins corresponding to a user-selected time interval (typically less than 1/10th the average cycle), and CT slices are automatically reconstructed from these bins. Because several respiratory points are sampled at each bed position, a 4D CT scan can take several times as long as a corresponding 3D CT, resulting in typically 1500 – 3000 CT slices for a 20 – 40 cm axial FOV.

The respiratory and scan data are combined at a separate computer, the Advantage Workstation (AW) (GE Medical Systems), which uses the respiratory trace to sort the oversampled CT slices according to their phase. The AW does perform the phase calculations, but rather relies on the phase stamp computed by the RPM during the creation of the respiratory trace file. Missing phases for any couch position are replaced with their nearest neighbor, providing a sorted image without any phase gaps. The user can navigate through the data in each axial direction, similar to standard viewing software, but can also scroll through the respiratory phases from end-inspiration to end-expiration. Individual phases can be subsequently extracted, or combined into averaged or minimum/maximum intensity projections, and exported to planning software in the form of standard DICOM series. These exported image series form the basis of 4D treatment planning.

4.2 Unresolved issues in 4D CT

The AW sorts the data by phase rather than amplitude. If the breathing were perfectly regular from

cycle to cycle, then phase- and amplitude-based sorting would give very similar results. The problem arises when there is variation in amplitude, period, or baseline, or when the onset of end-expiration does not occur at the same point each cycle. When these inconsistencies arise, the sorted CT images may contain mismatch artifacts at the interface between bed positions (see Fig. 4). Recent studies have investigated amplitude-based binning as an alternative to the phase-based approach, and it appears that amplitude sorting can improve image quality in many cases⁹⁵⁻⁹⁷. Other researchers have matched adjacent CT slices without using a respiratory trace, by maximizing the continuity of CT units integrated over regions of interest⁹⁰. Yet another promising approach involves interpolating the CT data continuously between end-cycle peaks using deformable models⁹⁸.

A second issue arises in the correlation between external fiducial movement and tumor/organ motion. Amplitude ratios between fiducial and tumor displacement may vary from cycle to cycle, and thoracic and abdominal points may involve relative phase shifts^{71, 99}. These shifts may be especially crucial for tumors near the lung, where hysteresis is prevalent. Finally, larger organs such as the liver can experience substantial deformation during inspiration and expiration, which may not be adequately captured by rigid-body interpolation between points in the respiratory cycle¹⁰⁰.

Finally, even if the 4D CT images have been acquired without problem, there remains the issue of reproducibility at treatment¹⁰¹. If treatment planning and delivery are based on 4D CT, there is an implicit assumption that anatomic motion during treatment will match the tumor and organ motion observed during setup. This assumption can be checked to some degree through frequent gated or breath-hold portal imaging¹⁰². On the other hand, it is reasonable to assume the patient will relax over time, so that their breathing becomes shallower or changes tempo. Indeed, studies have demonstrated that some patients exhibit systematic respiratory changes over a several-week course of radiation therapy, even with visual and audio coaching¹⁰³. These issues strike at the heart of IGRT, and provide a fertile ground for research.

4D CT usually delivers more radiation dose than the standard 3D CT, since multiple scans at each couch position are required in order to provide the temporal information. We have developed a method to perform 4D CT scans at relatively low current, hence reducing the radiation exposure of patients⁸⁷. To deal with the increased statistical noise caused by the low current, we proposed a novel 4D penalized weighted least square (4D-PWLS) smoothing method, which can incorporate both spatial and phase information. The 4D images at different phases are registered to the same phase via a deformable model, whereby a regularization term combining temporal and spatial neighbors is designed. The proposed method was tested with phantom experiment (see figure 5 for an example) and patient study, and superior noise suppression and resolution preservation were observed.

4.3 4D PET and related issues

4D PET poses a problem distinct from 4D CT, in that signal is inherently limited by the tolerable patient dose. The result is that any PET scan requires a significant amount of time per bed position (usually a few minutes) in order to acquire sufficient data to produce a good image. This limitation makes it difficult to partition PET data with the same time resolution possible in 4D CT, but nonetheless acquisition methods are clinically available to obtain PET images at end-inspiration or end-expiration. The most common solution is to gate the PET scan at the desired respiratory endpoint, and reconstruct a single bin of gated data¹⁰⁴⁻¹⁰⁶.

Patient setup proceeds in the same manner as an ungated PET scan, and a CT image is acquired for attenuation correction just prior to the PET. At this point, the RPM system monitors patient breathing by tracking the reflecting block, and the acquisition trigger is set by the user to occur at some given point (say, end-inspiration) in the cycle. Each time the RPM camera determines that the

reflecting block (and, by extension, the patient's respiration) reaches this point in the respiratory cycle, a trigger is sent to the scanner, and data accumulation is initiated. Gated PET differs fundamentally from the 4D CT protocol, by elevating the RPM system to this active role in data acquisition.

In gated mode, the user is able to select both the width of the acquisition window and the number of sequential bins to record each respiratory cycle. The bin width directly affects image quality, since the signal-to-noise ratio within an image asymptotically approaches the square root of the signal level¹⁰⁷. Multiple bin acquisition allows the capture of the full respiratory cycle in several bins, offering the possibility of retrospectively sorting into two or more respiratory phases. Each time the RPM trigger is received, data is directed to the initial bin, and then to the remaining bins sequentially until the next trigger. This process continues for the duration of the scan. Ideally the scan duration would be chosen such that the first bin (the respiratory point of most interest) would accumulate as many data points as a comparable ungated scan (i.e., divide the bin width by the duty cycle). In reality, since this would lengthen the typical PET scan by a factor of 4 or 5, practical clinical considerations may require the gated scan to be shortened, with corresponding image degradation.

Once the scan has finished, it is possible to associate each bin (beyond the first bin) with a corresponding point in the respiratory cycle. Since the respiratory trace is recorded by the RPM, it is a relatively simple matter to analyze the respiratory motion offline and make this correspondence. It is also possible to retrospectively combine multiple bins into a single bin, merging all the data to create an effectively ungated scan. However, these methods are not yet available from the vendor as a clinical tool, and must be performed by the user in the context of research efforts. Once the desired bin has been selected, its data can be reconstructed using the vendor-supplied filtered backprojection or OS-EM algorithms. The image results can subsequently be exported to treatment planning systems for review, similar to ungated PET series.

A salient point in the PET reconstruction process is the specification of the attenuation correction map. The current clinical design uses the CT scan acquired just prior to the PET specifically for this purpose. This attenuation correction CT can be acquired during either free breathing or breath-hold. Some research has indicated that PET reconstructions can be quite sensitive to distortions in the attenuation correction map¹⁰⁸⁻¹¹⁰, and investigations are ongoing into the use of 4D CT or other models to accurately account for attenuation^{80, 111}. On the Varian/GE system, this requires selecting the appropriate images from the 4D CT on the AW, sending these series back to the scanner, generating the attenuation correction maps for each 4D PET bin, and then reconstructing each bin separately. Once again, this is a research solution, and not yet available from the vendor for clinical use.

4.4 Combining 4D PET with 4D CT and enhancement of the performance of 4D PET with post-acquisition data processing

Once the 4D PET has been acquired (either a single phase, or perhaps several), it is possible to create a 4D PET/CT⁸⁰. This involves manually selecting the PET and CT images with corresponding respiratory phases (or amplitudes), and fusing them on viewing/planning software. We have recently developed a 4D-4D image registration algorithm, which allows us to automate the process. If the CT and PET scans are acquired with the same patient position on the same exam, then the process is a particularly simple hardware-based registration. On the Eclipse treatment planning system, for example, two images (not just PET/CT, but other modalities as well) can be automatically fused if they share the same DICOM coordinates. If the DICOM coordinates are not identical, the registration

is more difficult, requiring manual or automated shifts and rotations to match anatomical landmarks or fiducials. Fusion may be additionally complicated by organ deformation^{112, 113} (see Sec. 6). At the present time, PET/CT hardware fusion for ungated scans is well established and readily available within the clinical setting^{19, 20}. 4D PET/CT registration, however, remains primarily within the research domain.

The major issue in 4D PET is the lack of statistics. Since the collected photons are divided into several frames, the quality of each reconstructed frame is decreased with increasing number of frames. The increased noise in each frame heavily degrades the quantitative accuracy of the PET imaging. We have recently developed two corrective methods to enhance the performance of 4D PET. The first method, coined "retrospective" stacking (RS)^{81, 82, 114}, combines retrospective amplitude-based binning of data acquired in small time intervals, with rigid or deformable image registration methods. Unlike gating techniques, RS uses data along the entire respiratory cycle, thereby minimizing the need for lengthened scans while providing a four-dimensional view of the region of interest^{81, 82}. In the second approach¹¹⁴, we reconstruct each frame with all acquired 4D data by incorporating an organ motion model derived from 4D-CT images by modifying the well-known maximum-likelihood expectation-maximization (ML-EM) algorithm. During the processes of forward- and backward-projection in the ML-EM iterations, all projection data acquired at different phases are combined together to update the emission map with the aid of the deformable model, the statistics are therefore greatly improved. Both phantom and patient studies have indicated promising potential of the two methods.

4.5 Radiation treatment planning based on 4D information

How to maximally utilize the time-resolved image information derived from 4D CT or PET/CT represents one of the challenges in IGRT. In reality, the information can be integrated into radiation treatment planning and delivery at different levels. At the lowest level, the 4D images can be employed to determine the extent of tumor movement on a patient specific basis and the information can then be used to design the CTV margin and the radiation portals to accommodate the motion. Figure 6 shows an example of lung patient, in which tumor boundaries at three distinct respiratory phases are plotted. We have referred to this type of treatment as "3.5-dimensional" radiation therapy. The 4D information can also be used for guiding breath-hold or gated radiation therapy. There is also strong interest in using the 4D data to establish a 4D patient model and then to carry out a 4D radiation therapy plan. These are the subjects of the following two sub-sections.

4.6 Breath-hold and respiratory gating

Various methods have been worked out to counteract respiratory motion artifacts in radiotherapy imaging. Among them are breath-hold, respiration gating, and 4D or tumor-tracking techniques^{73, 74, 92, 94, 115}. Breath-hold techniques either actively or passively suspend the patient's respiration and treat the patient during this interval. Deep inspiration breath-hold, active breathing control (ABC) (which forces shallow breathing and thereby 'freezes' the tumor motion for a small part of the treatment time⁹²), and self-held breath-hold are suitable for different types of therapy targeting different cancers. Different types of equipment, such as stereotactic frames, fiducial tracking systems, timers, respirometer, RPM, or interlocks, may be needed depending on the method of breath-hold.

Respiration-gating methods involve tracking the patient's natural breathing cycle and periodically turning the beam on when the patient's respiration signal is in a certain phase of the breathing cycle (generally end-inhale or end-exhale). The patient's respiration is continuously monitored and the beam switches off as the tumor moves out of the target range. Gated radiation

therapy can offset some of the motion but requires specific patient participation and active compliance. In gated treatment it is required that the CT images used for treatment planning faithfully represent the actual treatment situation. While gated CT acquisition at the treatment respiratory phase is possible, our gating protocol proceeds by picking up the CT data at an appropriate phase from the patient's 4D CT acquired using the method described above. The gating interval is typically centered at end-expiration because of the increased reproducibility at this point, and spans 20-30% of the breathing period in order to provide a reasonable duty cycle. Treatment plans are optimized for this phase range by planning on an averaged composite of the scans within the interval, and using maximum- and minimum-intensity pixel views to incorporate intra-gate margins. The averaged, maximum-intensity and minimum-intensity composites for a lung patient are displayed in Figure 7.

4.7 Tumor tracking

Similar to the establishment of a 3D geometric modeling based on traditional CT data, the availability of 4D imaging information makes it possible to build a patient specific 4D model. Figure 8 shows the 4D models for three different patients⁹⁸. In obtaining the models, a BSpline deformable registration technique (see Sec. 6) was used to register different phases of the 4D CT. Ideally, organ motion represented by the 4D model can be incorporated into the radiation treatment plan optimization to overcome the adverse effect of respiratory motion on IMRT delivery¹¹⁶. A few groups¹¹⁵⁻¹²⁰ have explored the feasibility of MLC-based tumor tracking. However, the interplay between different phases has been ignored during the plan optimization in most of these studies. Webb has presented a technique to model the dosimetric effect of elastic tissue movement when modulated beams are delivered¹²¹. In general, the quadratic inverse planning objective function becomes

$$F = \sum_k \sum_i w_k [d_p^k - \int_t d_i^k(\vec{r}, t)]^2 \quad (2)$$

where d_p^k is prescribed dose for k th structure, w_k is the importance factor and $d_i^k(\vec{r}, t)$ is the calculated dose in voxel i at time t , and the summation over t represents the integral dose to i th voxel. For 4D planning it is necessary to know the path of each material coordinate during the treatment, which involves registering the voxels in different respiratory phases. This can be achieved by using a deformable registration algorithm. The optimization of the above objective function or alike^{115, 122-126} can proceed in a similar fashion as conventional 3D inverse planning to derive the optimal trajectories of the movements of the MLC leaves. An aperture-based optimization¹²⁷⁻¹²⁹ seems to be more adequate for dealing with the organ motion¹¹⁶.

4D methods propose to track the tumor with the radiation beam as the tumor moves during the respiration cycle. These techniques require acquisition of some form of respiration signal (infrared reflective markers, spirometry, strain gauges, video tracking of chest outlines and fluoroscopic tracking of implanted markers are some of the techniques employed to date), which is assumed to be correlated with internal anatomy motion. Fluoroscopy and the cine model electronic-portal-imaging device (EPID) have been proposed as a means for real-time guidance¹³⁰⁻¹³⁵. While tumor tracking seems to be the ultimate goal of 4D radiation therapy, the real challenge is clarifying whether the 4D model is repeatable at the time of fractionated treatments, and determining how to correctly synchronize the MLC movements with the patient breathing. Real-time imaging and/or adaptive approaches will likely play a role in this aspect and the issue will surely need more research for many years to come.

5 Inter-fraction organ movement

5.1 Current techniques in dealing with inter-fraction organ movement

Uncertainty in patient setup has long been known as a limiting factor to conformal radiation therapy. Currently, the accuracy of patient setup is verified by megavoltage (MV) radiograph acquired with either radiographic film or EPID¹³⁶⁻¹³⁸. The patient's bony landmarks are used to guide patient alignment. Poor soft tissue contrast and often unclear projection of the bony anatomy are major problems of the approach. To improve the situation, planar kV x-ray imaging has been implemented in a variety of forms¹³⁰⁻¹³⁵. While these systems show significantly increased contrast for bony structure differentiation, observing soft-tissue detail remains problematic and correction of daily organ motion is still challenging. Attempts have been made to use CT imaging to facilitate the patient setup process. Along this line, the offline adaptive-radiation-therapy (ART) strategy^{139, 140} and in-room CT approach¹⁴¹ have been studied. The former method aims to partially compensate for organ motion by carrying out multiple CT scans in consecutive days in the first week of treatment. The image data are then employed to construct a patient specific PTV model from the composite of the CTVs with inclusion of statistical variations of the observed motions. While beneficial, the approach is hardly an ideal solution for dealing with the inter-fraction organ motion. It relies on establishing a statistical ensemble of all possible setup scenarios under a strong assumption that a limited number of off-line CT scans can adequately describe the inherently complex, often unpredictable inter-fraction organ motion. Even when it is achievable, the ART margin is not optimized on a daily basis and there is still room for further improvement. An integrated CT/LINAC combination, in which the CT scanner is located inside the radiation therapy treatment room and the same patient couch is used for CT scanning and treatment (after a 180-degree couch rotation), should allow more accurate correction of interfractional setup errors. Some major radiotherapy vendors provide options to install a CT scanner in the treatment room. The overall precision of EXaCT TargetingTM from Varian has been evaluated by Court et al¹⁴¹. However, the approach assumes a fixed relationship between the LINAC isocenter and the CT images and relies heavily on the mechanical integrity of the two otherwise independent systems. Increased capital cost and prolonged imaging and treatment are other concerns.

Other patient localization techniques available include ultrasound-based methods, video-based surface tracking, on-board cone-beam CT or kV x-ray imaging, CyberKnife and Tomotherapy, etc. For prostate radiation therapy, on-line ultrasound imaging has gained substantial interest¹⁴²⁻¹⁴⁴ but in practice has been found susceptible to subtle sources of error and inter-user variability. On-board CBCT holds promise to become a robust integrated on-line imaging technology that can yield unambiguous soft-tissue detail at the time of treatment. Furthermore, CT numbers correlate directly with electron density, thereby providing the potential for reconstruction of the actual dose delivered on a daily basis, in addition to simple anatomic structure alignment. The details of emerging CBCT will be presented in the next section. The robotic CyberKnifeTM from Accuray Inc. represents another promising technology. The system has a feedback mechanism in which motion of the CTV, determined through the Accutrak infrared-x-ray-correlated imaging system, can be fed back to the robot to track the CTV¹⁴⁵. However, while this improves the duty cycle, there is a finite time between measuring tumor position and arranging the compensation for motion. Helical tomotherapy is an alternative means of delivering IMRT using a device that combines features of a linear accelerator and a helical CT scanner¹⁴⁶. The commercial version, the HI-ART IITM, can generate CT images using the same MV radiation beam that is used for treatment. Since the unit uses the actual treatment beam as the x-ray source for image acquisition, no surrogate telemetry systems are required to register image space to treatment space. Objective measures of noise, uniformity, contrast, linearity, and

spatial resolution, and comparison with that of a commonly utilized CT simulator have recently performed by Meeks et al ¹⁴⁷.

5.2 CBCT for patient localization

CBCT based upon flat-panel technology integrated with a medical linear accelerator has recently become available from linac vendors for therapy guidance. The volumetric images may be used to verify and correct the planning patient setup in the linac coordinates by comparing with the patient position defined in treatment plan. Both kV and MV beams have been utilized for the application. The former typically consists of a kV-source and flat-panel combination mounted on the drum of a medical accelerator ¹⁴⁸, with the kV imaging axis orthogonal to that of MV therapy beam. The fan-beam and cone-beam MV CT in clinical applications have been reported by Meeks et al ¹⁴⁷ and Poulliot et al ¹⁴⁹, respectively. It appears that the MV images contain sufficient resolution of bone and air cavities to register them to structures in the planning CT with millimeter precision ^{148 149}.

Currently, CBCT is primarily used for guiding the patient setup ^{150, 151}. The procedure is not much different from the current patient treatment, other than the fact that the AP/LAT portal images are replaced by volumetric data. In figure 9 we show 3D CBCT images of a prostate case in one of the fractional treatments along with the patient's planning CT image. It is seen that soft-tissue structures and boundaries are visible to varying degrees in the CBCT images. The patient has implanted fiducials, which show up on both CBCT and planning CT. Our experience indicates that the cone beam data can clearly reveal setup error, as well as the anatomical deformations and other physiological changes. During the patient setup process, the 3D CBCT images are registered with the planning CT data through the use of either manual or automated 3D image registration software that calculates shifts in x-, y- and z-directions (depending on the manufacturer, rotations can also be included). The movements determined during the registration represent the required setup corrections that should be applied to the patient. Both phantom and patient studies from our group have shown that the volumetric imaging is superior to the conventional MV or kV AP/LAT patient setup procedure. We note that, if only translational shifts are permissible, the level of improvement is generally within 2mm as compared with kV AP/LAT setup procedure (2D/2D match). However, CBCT can readily detect rotational errors which otherwise be missed by the 2D/2D match. In figure 10 we show the localization image for a head phantom with kV/kV 2D/2D match and 3D/3D match (CBCT/planning CT). The latter approach was found to be sensitive enough to identify a rotational error as small as 2°.

In practice, much effort is needed to improve the robustness and efficiency of the volumetric image registration process. Furthermore, in order to fully utilize the volumetric data, a new paradigm with seamlessly integrated simulation, planning, verification, and delivery procedure is urgently needed. Until this is realized clinically, the volumetric imaging is nothing but an expensive extension of the already functional planar verification approach. The capital cost and other related overheads do not seem to justify the marginal benefit if the volumetric data is simply used for determining the patient shift in the space. However, one should not underestimate the potential of the volumetric imaging for the future of radiation therapy, as it opens a new avenue (perhaps the only avenue), for us to realize the planned dose distribution with high confidence in clinical settings.

A few groups are working on deformable model based segmentation and patient setup procedures ^{113, 150-152}. When deformable registration is used, there are a few options to achieve the registration depending on whether the primary aim is to match soft-tissue, or to align 3D bony structures. In figure 11 we show a patient's CBCT and planning CT registration results using different registration schemes. The multiple choices result from the fact that the dimensionality of the patient data is much greater than that in the patient setup procedure and suggest that deformable

registration is not the ultimate solution to volumetric image-guided radiation therapy. Nonetheless, the technique improves the current method¹⁵¹ since it partially takes into account organ deformation by achieving the closest overlay match possible between the planning and CBCT data sets according to our clinical objective, and serves as a useful interim solution before a better integrated approach becomes available.

5.3 CBCT-based dose verification

Another important application of on-board volumetric imaging is verification of dose delivery. We have recently evaluated the accuracy of CBCT-based dose calculation and examined if current CBCT is suitable for the daily dose verification of patient treatment^{153, 154}. A CT-calibration phantom was first used to calibrate both conventional CT and CBCT. CT and CBCT images of the calibration phantom, an anthropomorphic phantom and two patients (a lung and a prostate case) were then acquired for this study. Our results indicated that the imperfect quality of CBCT images has minimal impact (<3%) on the dosimetric accuracy when the intra-fractional organ motion is small. When intra-fractional organ motion is large and motion artifacts is severe (e.g., in the case of lung cancer), the dosimetric discrepancy due to the poor image quality of current CBCT was found to be clinically significant. Furthermore, in the latter case, we found that it is possible to use a deformable registration algorithm to map the corresponding electron density information from planning CT to CBCT and then to proceed with conventional dose calculation.

5.4 Respiratory motion artifacts in CBCT

Superior to the common approaches based on two orthogonal images, CBCT can provide high-resolution 3D information of the patient in the treatment position, and thus has great potential for improved target localization and irradiation dose verification. In reality, however, scatter and organ motion are two major factors limiting the quality of current CBCT. When CBCT is used in imaging thorax or upper abdomen of a patient, respiration induced artifacts such as blurring, doubling, streaking, and distortion are observed, which heavily degrade the image quality, and affect the target localization ability, as well as the accuracy of dose verification. These artifacts are much more severe than those found in conventional CT exams, in which each rotation of the scan can be completed within a second. On the contrary, in CBCT scan, the gantry rotation speed is much slower, typically 40 seconds to 1 minute for a full 360-degree scan in acquiring the projection data, which is more than 10 breathing cycles for most patients. In figure 12 we show the influence of the same motion on a regular "fast" CT scanner and CBCT for a motion phantom, where it is clearly seen that the motion artifacts are much greater than that in a fast scanner.

In the last decade considerable effort has been devoted to finding solutions to remove motion artifacts and to obtain time-resolved medical images. Wang and Vannier¹⁵⁵ presented a patient-motion estimation and compensation technique for helical CT systems. Willis and Bresler¹⁵⁶ cast the motion artifact problem as a time-varying tomography problem and required special-purpose hardware to optimally sample the spatially and temporally band-limited CT signal space. A parametric model for the respiratory motion was used in MRI, and the motion artifacts were successfully reduced by modifying the reconstruction algorithm¹⁵⁷. Crawford *et al*¹⁵⁸ brought the concept into CT imaging, and derived an exact reconstruction formula for motion compensation for CT scans. Generally, motion correction algorithms that assume a motion model work well when the motion conforms to the model, but have limited success when it does not. As described in Sec. 4.1, 4D CT has been developed in radiation oncology application in order to explicitly account for the respiratory motion. The 4D CT can be used to derive a patient-specific deformation field and then

incorporated into the CBCT filtered-backprojection (FBP) image reconstruction process¹⁵⁹. The algorithm was tested with simulations at different settings corresponding to conventional CT and CBCT scan protocols, with translational motion and more complex motion, and with and without Gaussian noise. In figure 13 we show the result for the motion phantom depicted in figure 12.¹⁵⁹ Since the motion model is directly derived from the patient images, it should be more accurate than other artificial modeling, and therefore more efficient motion correction is expected. In addition to this approach, Sonke et al¹⁶⁰ developed a CBCT procedure consisting of retrospective sorting in projection space, similar to that used in 4D CT (Sec. 4.1). The subsets of projection data are then reconstructed into 4D CBCT dataset. To achieve a sufficient temporal resolution, however, this will require slowing down the gantry rotation. The assumption of periodicity of the respiratory motion is also necessary. Zeng et al¹⁶¹ proposed a method to estimate the parameters of a non-rigid, free-breathing motion model from a set of projections of thorax that are acquired using a slow rotating CBCT scanner.

6. Rigid and deformable image registration

Development of an effective image registration technique has been one of the most important research areas. Depending on the mathematical nature of the transformation, image registration is divided into rigid and deformable registrations. In rigid transformations, it is assumed that the geometry of the object is identical in the two input images and no distortion occurs in the image acquisition process. A rigid transformation consists of six degrees of freedom: three displacement parameters and three rotational parameters. Deformable registration, on the other hand, is more complicated and entails the modeling of voxel dependent distortion. Clinically, the need for a robust image registration algorithm to compare/fuse images representing the same structures imaged under different conditions or on different modalities is ever increasing because of the extensive use of multi-modality imaging and the emergence of new imaging techniques and methods.

Computer-based rigid image registration has gained widespread popularity in the last decade and is used in routine clinical practice. In this approach, the matching of the two input images is formulated into an optimization problem and the best registration of the two images is obtained by iteratively comparing various possible matches until no better registration can be found. The search for the optimal match of the two input images is usually gauged by a ranking function constructed based on some physical considerations. Depending on the nature of the input images, the formulation of the problem can be highly complicated. Court and Dong¹⁶² used a rigid transformation for the correction of tissue displacement. A deformable procedure based on the finite element model (FEM), in which images are described as blocks of elastic materials on which forces apply, was proposed by Bharath *et al*¹⁶³ and Brock et al.¹⁶⁴ In this approach, the parameters that control the behavior of the elastic material and are responsible for the conversion of forces into local deformations of the elastic material are Young's elastic modulus and Poisson's ratio. Although powerful, the model has the drawback that values of the elasticity and density constant for various tissues are not readily available and have to be found by a trial and error procedure. The method also relies on using complicated software to generate a FEM mesh and masks of the involved structures. Schreibmann and Xing have proposed a general narrow-band approach for deformable registration¹¹³. Depending on the problem, modeling of individual voxel movement can also be made using either B-splines⁹⁸, thinplate splines^{165, 166}, optical flow algorithms¹⁶⁷, or fluid flow algorithms¹⁶⁸. Spline interpolation is a relatively simple approach and our experience with the algorithm suggested that the free-form registration is stable and accurate for dealing with IGRT image registration problems¹⁶⁹. An improvement to this

method can be achieved by using a spline model with the smoothness of the deformation field assured by the interpolation between a grid of fixed control points. A simple method along this line is to deduce the spline coefficients from a set of user-defined control points, as was done by Fei *et al.*¹⁷⁰ and Lian *et al.*¹⁶⁶ in warping and registration of MR volumes. Coselmon *et al.*¹⁷¹ used a similar technique to study the accuracy of mutual-information-based CT registration of the lung at exhale and inhale respiratory states.

To facilitate the computer decision-making process, image pre-processing or user interaction may be required, especially when dealing with a deformable image registration. The use of homologous anatomic landmark pairs on the two input images or the control points is an example of this. In reality, the user must have a detailed understanding of the patient anatomy and the characteristics of the two modalities in order to accurately identify the control points on both images. The point pairs are usually obtained interactively with the user repetitively exploring the input image sets and each time trying to locate a point in both of them. Due to the 3D nature, the process is rather tedious and difficult to perform. Schreiber and Xing¹⁷² have developed a general method to facilitate the selection of control points for both rigid and deformable image registrations. Instead of relying on the interactive selection of homologous control point pairs on both model and reference images, in the proposed approach the user needs only to identify some small control volumes on the model image in a somewhat arbitrary fashion. This new way of image registration eliminates the need for the manual placement of the homologous control points and allows us to register the two images accurately and efficiently. The method was applied to both rigid and non-rigid image registration problems and our results indicated that the registration is reliable and provides a valuable tool for intra- or inter-modality image registration. In figure 14 we show the registration result of a rectal cancer patient who has undergone both CT and FLT-PET scans. The increased robustness and confidence in the registration and the increased speed of calculation, especially in the case of the deformable registration, are important features of the new technique. Compared to the manual rigid registration, this method eliminates the nuisance of the control point pair selection and removes a potential source of error in registration. Compared to the automated method, the technique is more intuitive and robust, especially in the presence of image artifacts.

7. Clinical experience with IGRT

Clinically implemented IGRT techniques at Stanford include 4D CT, 4D PET, Varian OBI (both planar and CBCT), gating, and Accuray CyberKnife. Several image-guided clinical protocols are under investigation. 4D CT/PET information are used in about 40% of the thorax and upper abdomen cases for patient specific tumor margin definition in 3.5D radiation therapy or for treatment planning of gated radiation therapy. CBCT is mainly applied for patient setup in the treatment of head and neck, prostate and other pelvic diseases. For these sites, the CBCT image quality is reasonable to visualize soft tissues, but the quality is generally notably inferior to that of the state-of-the-art multi-slice fan beam CT scanner. Scan truncation artifacts because the patient shadow does not fit on the detector and/or organ motion often cause Hounsfield unit calibration problems. While this does not seem to influence the image registration, the use of CBCT for dose calculation should proceed with caution. Our initial experience indicates that, when compared with traditional CT-based calculation, the dosimetric error is typically less than 3% for prostate or head and neck cases but could be significantly greater in the thoracic region. Comparison between cone beam data and portal image derived setup errors show only slight differences (<2 mm). However, we should note that the differences are derived purely based on the use of manufacturer-provided image-fusion software,

which often emphasizes the high intensity voxels in bony structures. The next step is to implement soft-tissue based setup corrections clinically. In reality, volumetric data contain much more information compared to planar images, and CBCT promises to be more useful in the future when it is better integrated with treatment planning and delivery systems. An ideal integration would be to use volumetric image-derived information to "tweak" or re-optimize the treatment plan. This work is still in progress at Stanford.

As another example of IGRT treatment, we describe our phase I and II pancreatic tumor dose escalation protocol. The aim is to use CyberKnife to target pancreatic tumors more precisely and to limit the toxicities associated with treatment. In a phase I study, we treated patients with a single fraction of 15, 20, and 25 Gy to unresectable pancreatic tumors using the Cyberknife stereotactic radiosurgery (SRS) system (Accuray Inc, Sunnyvale, CA)¹⁷³. To track tumor movement, we implant fiducial seeds percutaneously into the pancreatic tumor. Using the Accuray Synchrony platform, a model in which the position of the internal fiducials is correlated with the patient's respiratory motion is developed. The Cyberknife is able to make real time corrections to compensate for tumor movement during respiration. Prior to treatment, patients underwent 4D planning CT scans. Using this dataset, we are able to visualize how the pancreatic tumor moves/deforms through respiration and compensate for these dynamic changes¹⁷⁴. Minimal acute gastrointestinal toxicity was observed even at the highest dose. All patients who received 25 Gy had no further local progression of their tumor until death. In a follow up phase II study, a cohort of 19 patients were treated with 45 Gy conventionally fractionated radiation therapy using IMRT to the pancreas and regional lymph nodes followed by a 25 Gy Cyberknife stereotactic radiosurgery boost to the primary tumor¹⁷⁵. An excellent rate of local control with this therapy was confirmed. Because of the rapid progression of systemic disease, we did not observe a significant improvement in overall survival as compared to historic controls. However, most patients had a clinical benefit (decreased pain, increased activity) and decreased serum tumor marker for pancreatic cancer (CA-19-9) following therapy. To document that SRS truly resulted in an anti-tumor effect, we routinely obtain FDG-PET/CT scans before and after treatment. Figure 15 is an example of one such study. There was intense metabolic activity of the pancreatic tumor prior to therapy with a near complete resolution of FDG uptake in this patient 4 weeks following therapy. The technological challenge for IGRT to minimize toxicity in this clinical scenario is the precision delivery of high dose radiotherapy. This cannot be accomplished without taking into account the respiratory associated motion of pancreatic tumors. This movement takes place in multiple planes and can result in tumor displacement of up to 1-2 cm. Furthermore, tumor and organ deformation during respiration must also be compensated for during therapy.

8. Summary

With the development of IMRT during the 1990s, radiation therapy entered a new era. This new process of treatment planning and delivery shows significant potential for improving the therapeutic ratio and offers a valuable tool for dose escalation and/or radiation toxicity reduction. The improved dose conformity and steep dose gradients necessitate enhanced precision and accuracy in patient localization and spawn the development of IGRT, in which various metabolic and anatomical imaging techniques are integrated into the radiation therapy process. The overall goal of IGRT is to target tumors more accurately while better sparing the normal tissues. Much recent effort is focused on removing the uncertainty in the definition of the target volume and in the determination of the position of mobile and often deformable organs. Biological imaging described in this article will allow us not only to delineate the boundary of the tumor volume based on the tumors' biological characteristics but also to map out the biology distribution of the cancer cells, affording a significant

opportunity for BCRT treatment in the future. Developments of effective 4D CT/PET techniques will provide effective means for us to understand the temporal dependence of the involved structures and design the best possible strategy for targeting the moving tumor. Integration of various imaging tools for off-line and on-line application is also of paramount importance, enabling us to ensure the planned dose distributions can be realized in the clinical setting. With the newly available IGRT tools, physicians will be able to optimize radiotherapy accuracy and precision by adjusting the radiation beam based on the actual positions of the target tumor and critical organs during radiation therapy planning and treatment. We should mentioned that IGRT is still in its infancy and many technical issues remain to be resolved, such as the establishment of a robust deformable registration method, auto-mapping of the contours outlined on the planning CT to CBCT or to different phases of 4D CT, and management of the sheer volume of acquired image sets (both 4D CT/PET and CBCT). However, it is believed that much of these technical hurdles will be resolved with time, and that IGRT will become the standard of practice in the future through the effort of researchers around the world.

Acknowledgement

We wish to thank the following individuals for their input and help: Drs. S. Hancock, C. King, B. Loo, K. Goodman, Q. Le, K. Horse, A. Boyer, D., P. Maxim, A. Hsu, T. Pawlicki, Spielman, S. Gambhir, A. Quon, D. Levy from Stanford University, and S. Johnson, R. Morse, P. Munro, C. Zancowski, R. Wicha, M. Svatos, and R. Stark from Varian Medical Systems, G. Chen from Massachusetts General Hospital, and G. Mageras from Memorial Sloan Kettering Cancer Center. This work is supported in part by a research grants from the National Cancer Institute (5R01 CA98523-01), Department of Defense (PC040282), the American Cancer Society (RSG-01-022-01-CCE), and Varian Medical Systems.

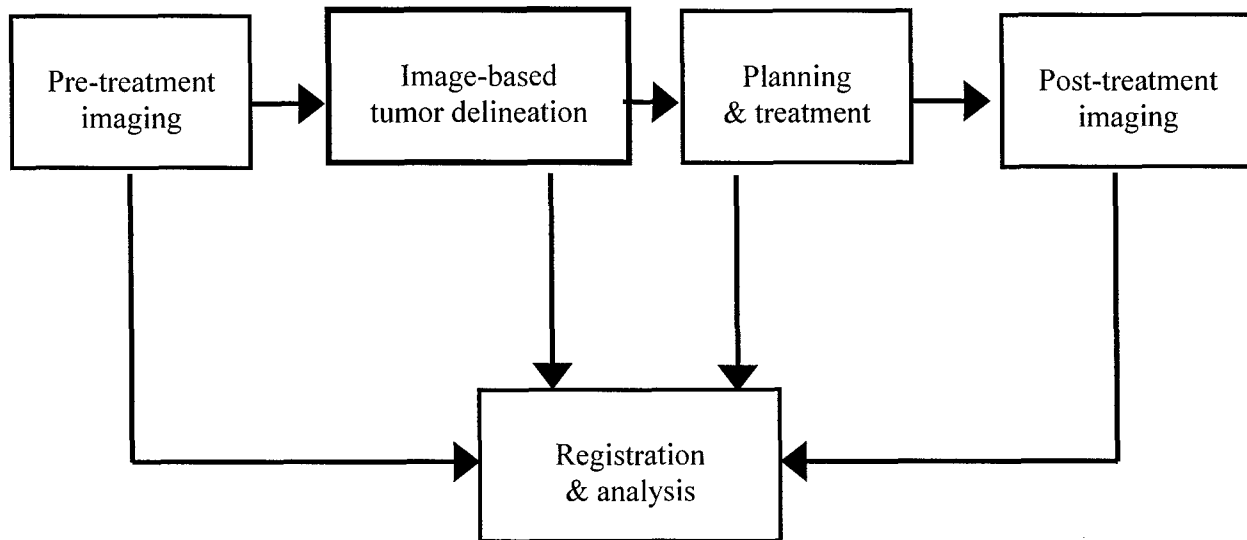


Figure 1 Role of imaging in radiation oncology practice.



Figure 2 Cine MR images at two different phases for a liver cancer patient.

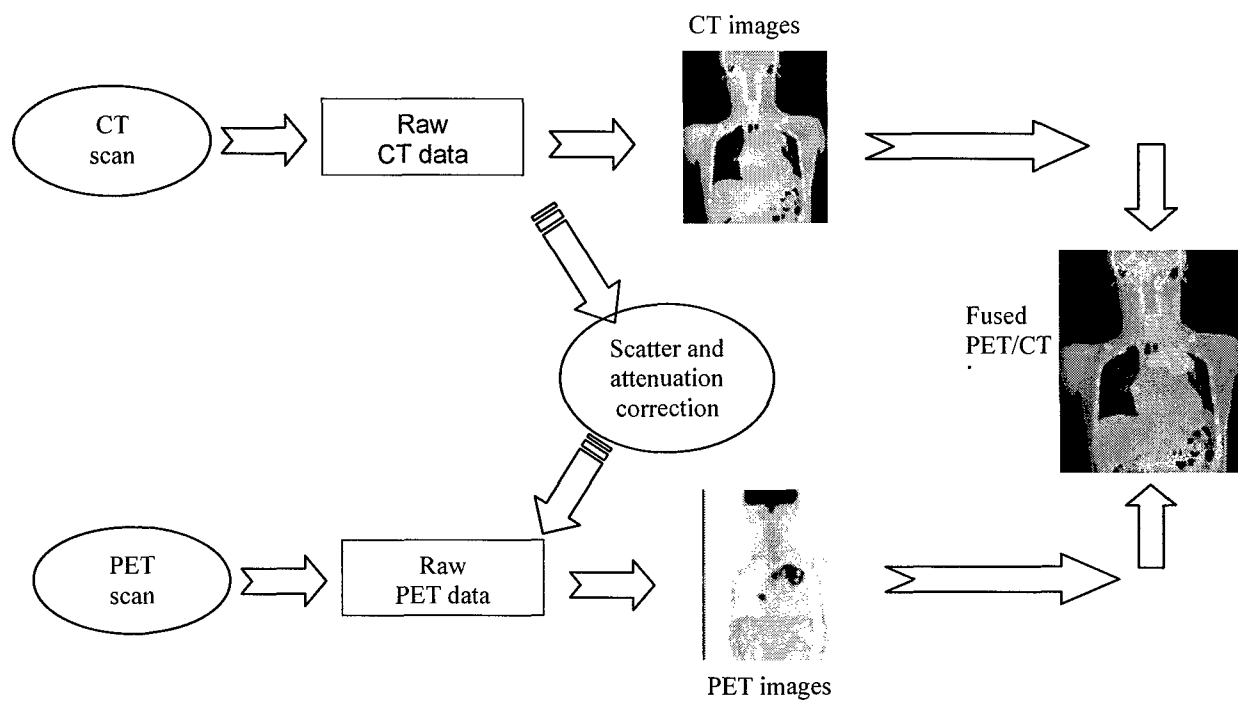


Figure 3 A schematic drawing of the data flow in a hybrid PET/CT.



Figure 4: Example of 4D CT where respiratory cycle irregularities have produced significant interbed mismatches near the base of the lung.

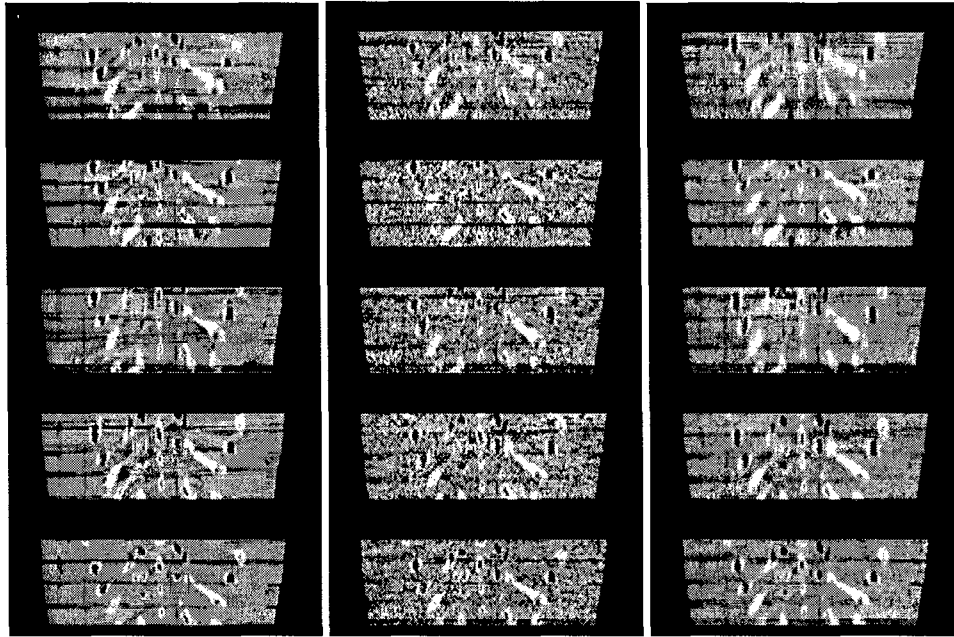


Figure 5. Motion phantom study for the 4D-PWLS method with the thorax phantom. The left and middle columns are the original phases obtained from the GE Advantage Workstation, for 100 mA and 10 mA, respectively; the right column shows the 10 mA phases after 4D-PWLS processing. From top to bottom are phase 0%, 20%, 40%, 60%, 80%, respectively. The red rectangles represent the selected ROI for calculation of SNRs, each of which contains 5x5x5 voxels. PWLS Smoothed 10-mA scan resulted more than two-fold increase in the SNR for every phase of the periodically moving phantom. Similar results were obtained in a patient 4D CT study.

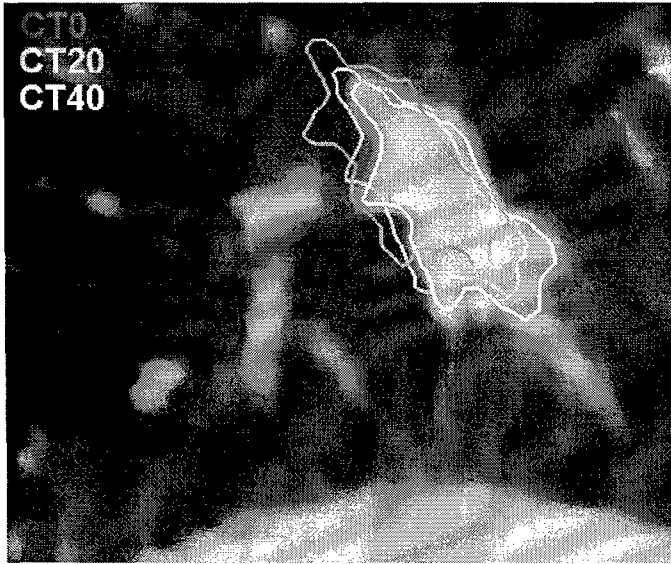
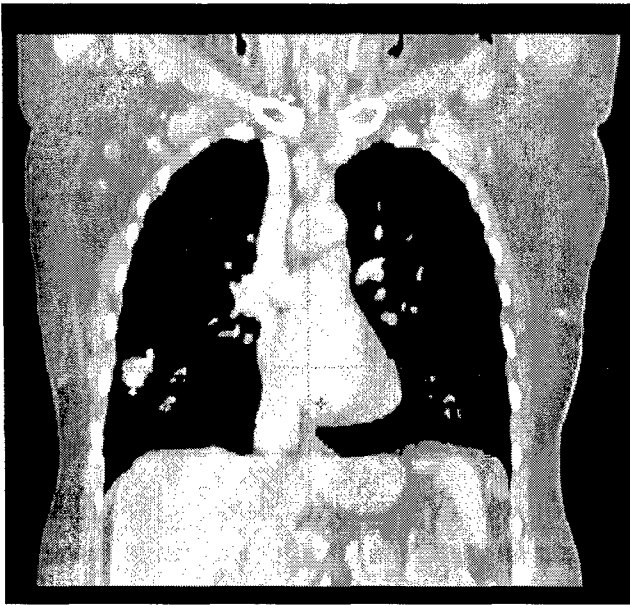


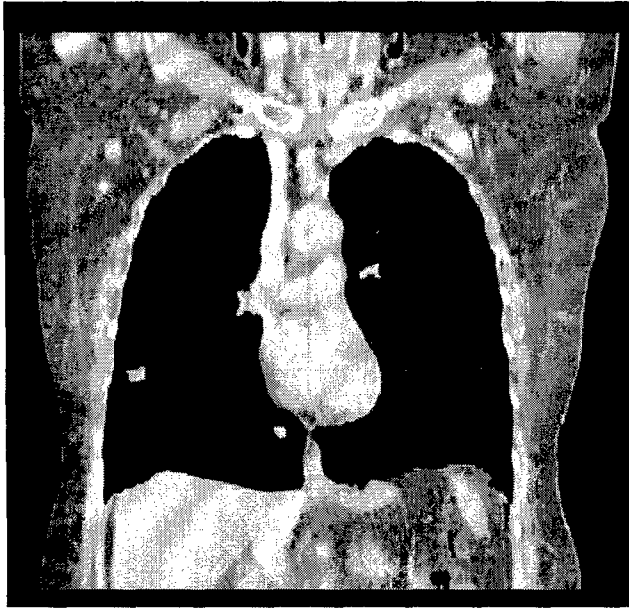
Figure 6 Tumor contours for three breathing phases. The contours labeled as CT20 and CT 40 were produced by applying the deformation field on the tumor contours delineated in CT0.



(a)



(b)



(c)

Figure 7. Composite scans of a 4D CT lung patient. (a) Average pixel; (b) Maximum-intensity pixel; (c) Minimum-intensity pixel. The maximum-intensity pixel composite reveals the motion extent of hyperdense tissue (e.g., lung tumor), while the minimum-intensity pixel view provides the motion range of hypodense regions (e.g., lung air volume).

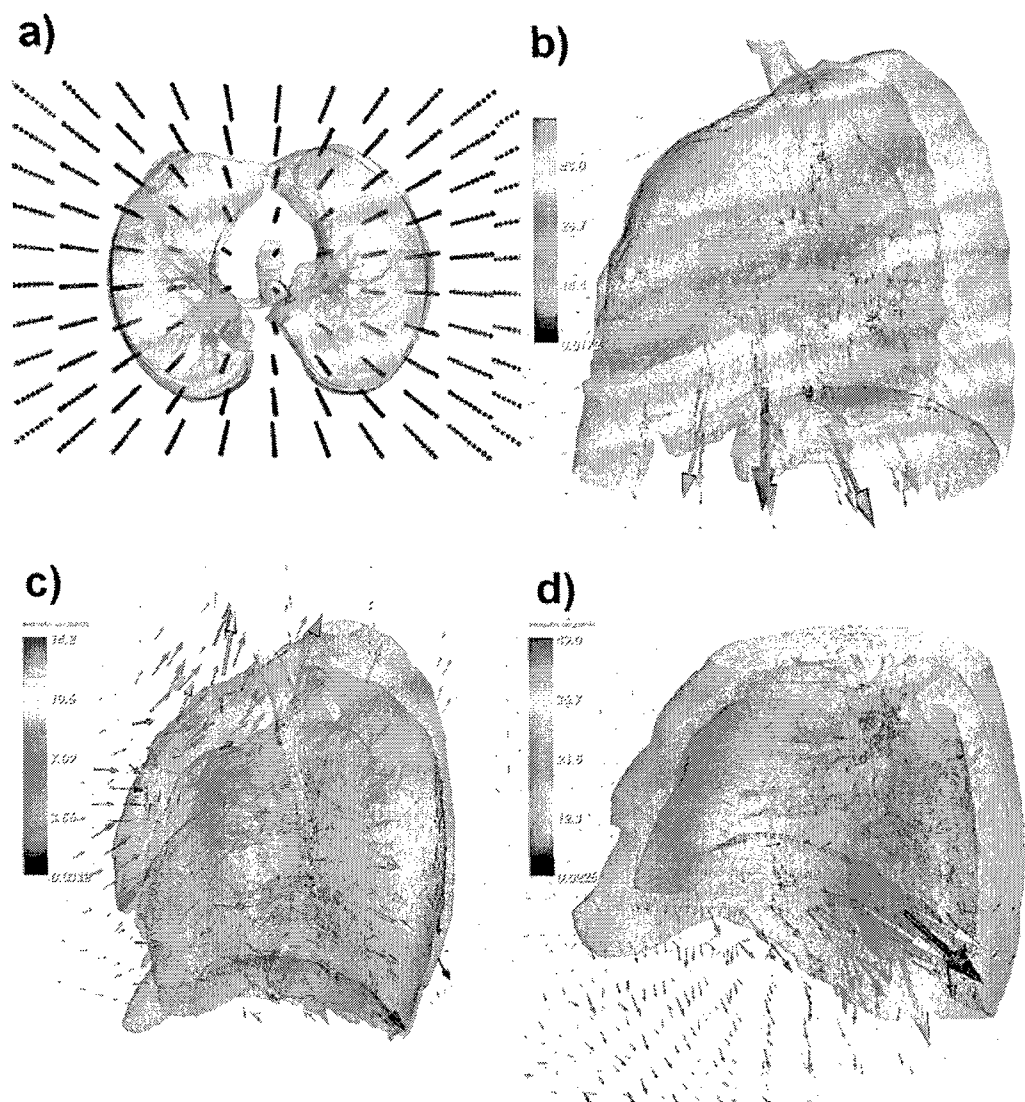
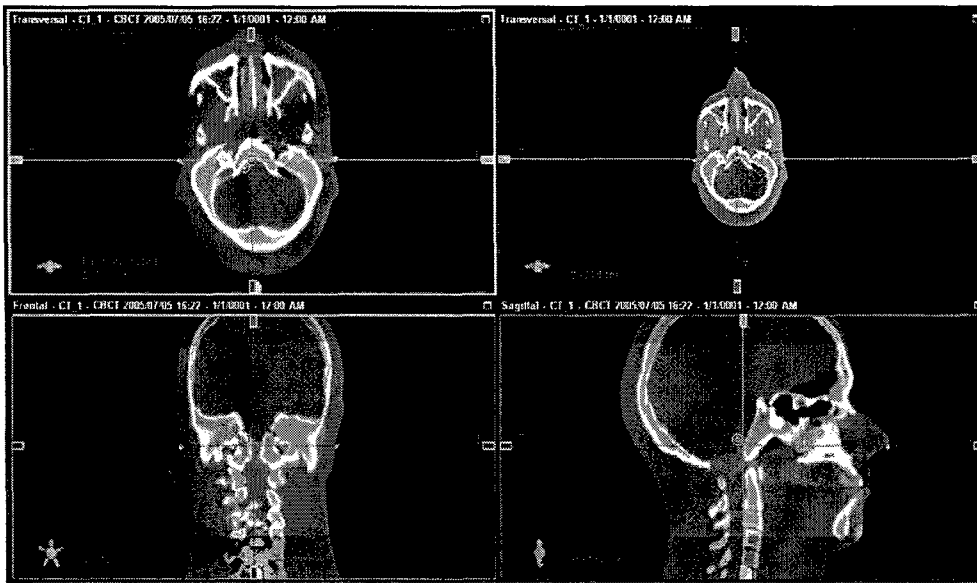
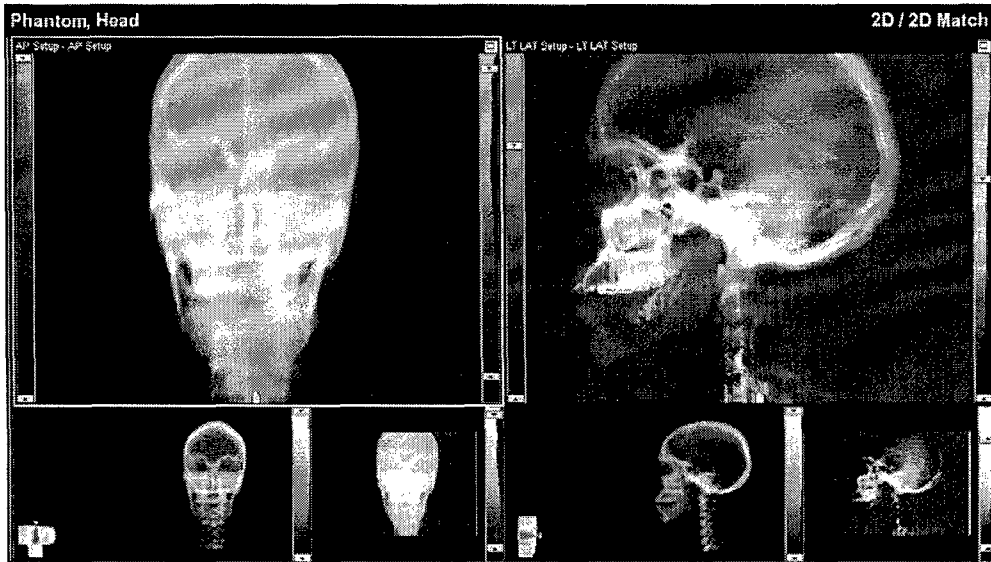


Figure 8. (a): The BSpline grid superimposed on lung contours (b): On each node, deformation is represented by arrows, where arrow length is proportional to the deformation. (c) and (d): Same analysis for two additional patients.





Figure 9 CBCT (top) and planning CT (middle) for a prostate case. The fusion of the two types of CT images is shown in the bottom panel.



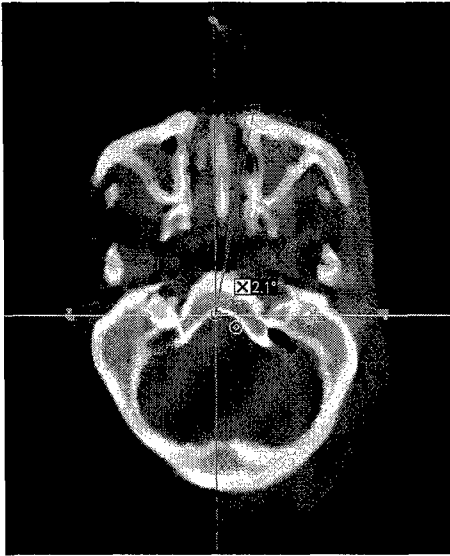
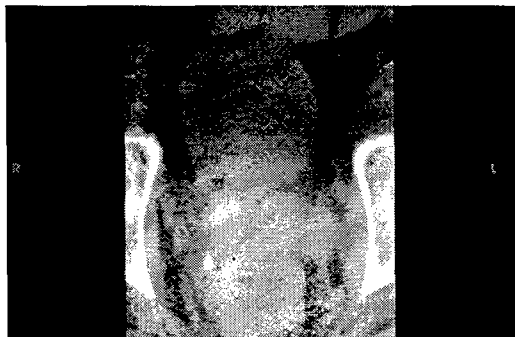


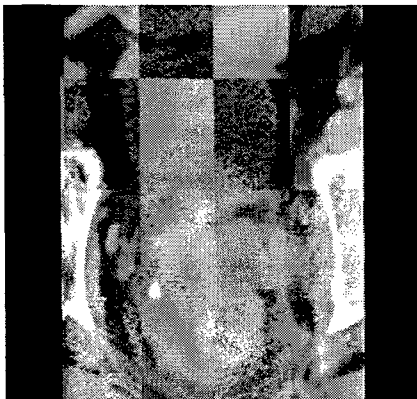
Figure 10. Setup localization image for head phantom with kV/kV 2D/2D match (top) and 3D/3D CBCT match (middle). The image shown in the bottom panel illustrate that the CBCT is a sensitive technique capable of picking up a 2° rotational miss-match between the planning CT and CBCT.



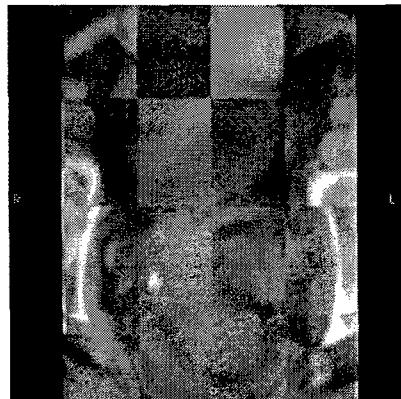
CBCT



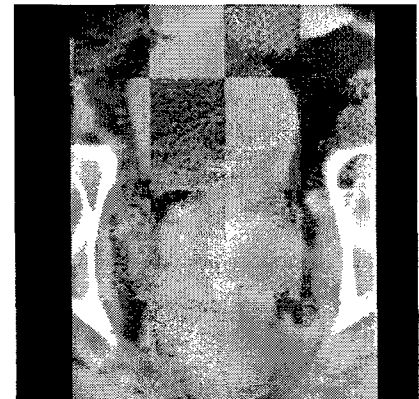
CT



Match bony structure

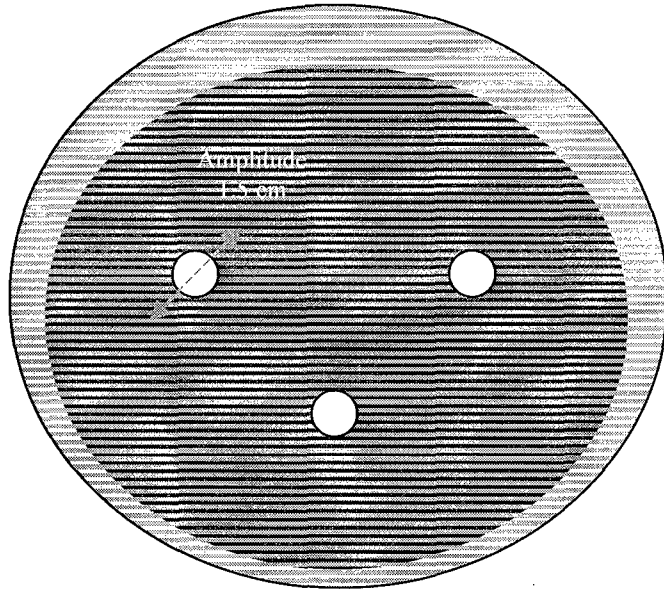


Match soft tissue

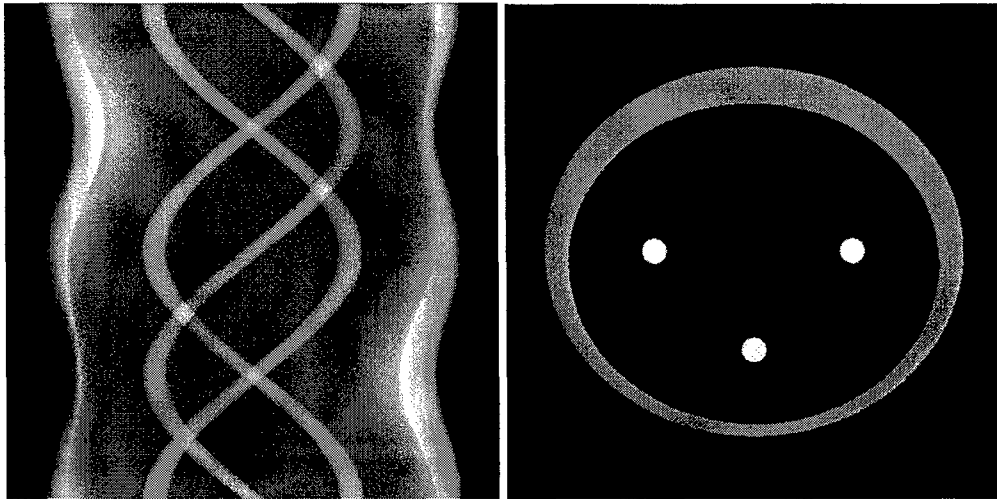


**deformable
registration**

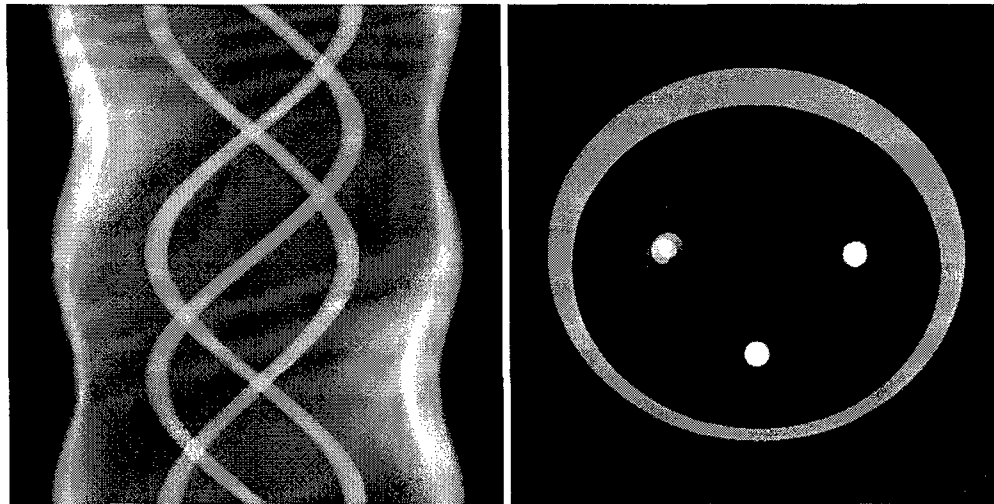
Figure 11 Image registration of CBCT and planning CT based on bony structure matching, soft tissue matching and deformable registration.



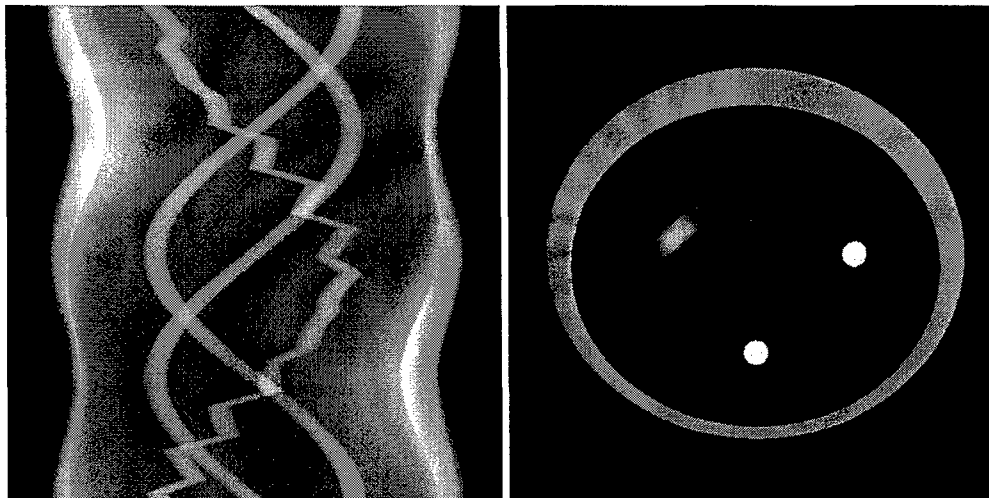
(a)



(b)



(c)



(d)

Figure 12 (a) Motion phantom for CT and CBCT simulation study. The left circle moves diagonally with an amplitude of 1.5 cm and a period of 3.52 sec. (b) Simulated sinograms and their corresponding reconstructed images with standard FBP algorithm when the circles are stationary. (c) and (d) show the sinograms and their corresponding reconstructed images for 1sec/rotation acquisition (conventional CT scan speed) and 40sec/rotation acquisition (on-board CBCT scan speed), respectively.

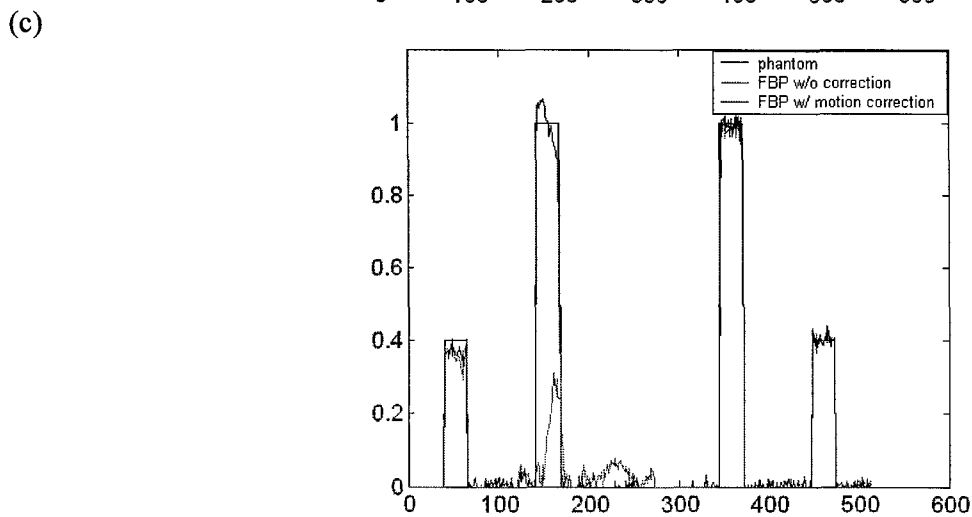
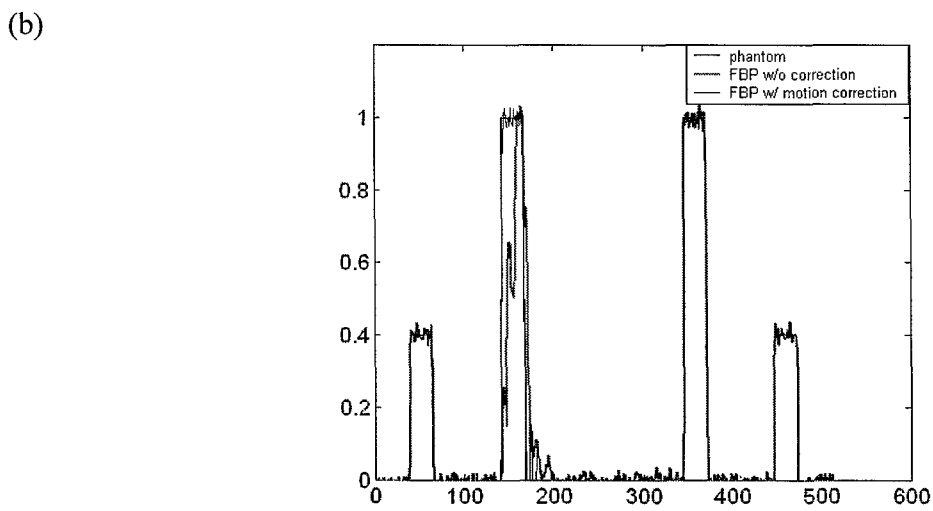
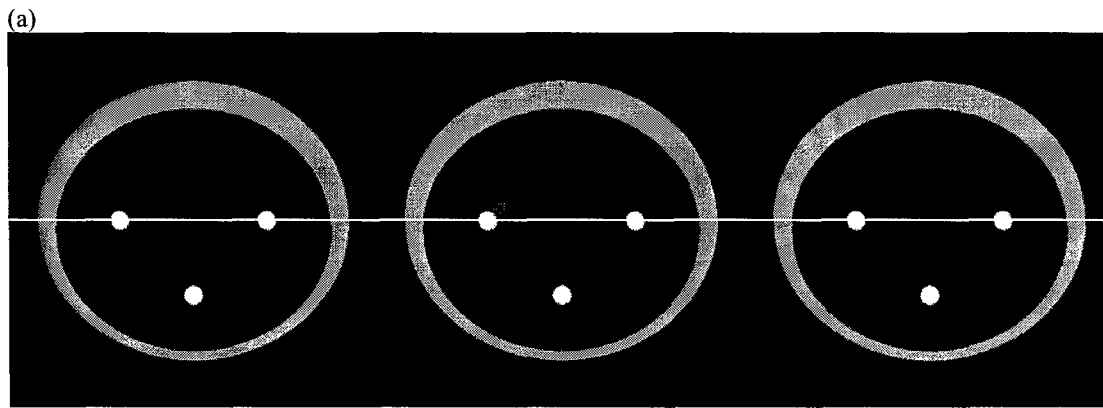


Figure 13 (a) Phantom and images reconstructed with motion correction for CT and CBCT settings. The three images represent the reconstructed image of stationary phantom (left), the conventional “fast” CT (middle), and the CBCT (right). (b) and (c) Horizontal profiles through the moving circle for the images shown in the middle and right panels (blue curves). For comparison, the profiles for the stationary phantom (left panel) and images reconstructed without motion artifacts removal mechanism are also plotted (black and red curves, respectively).

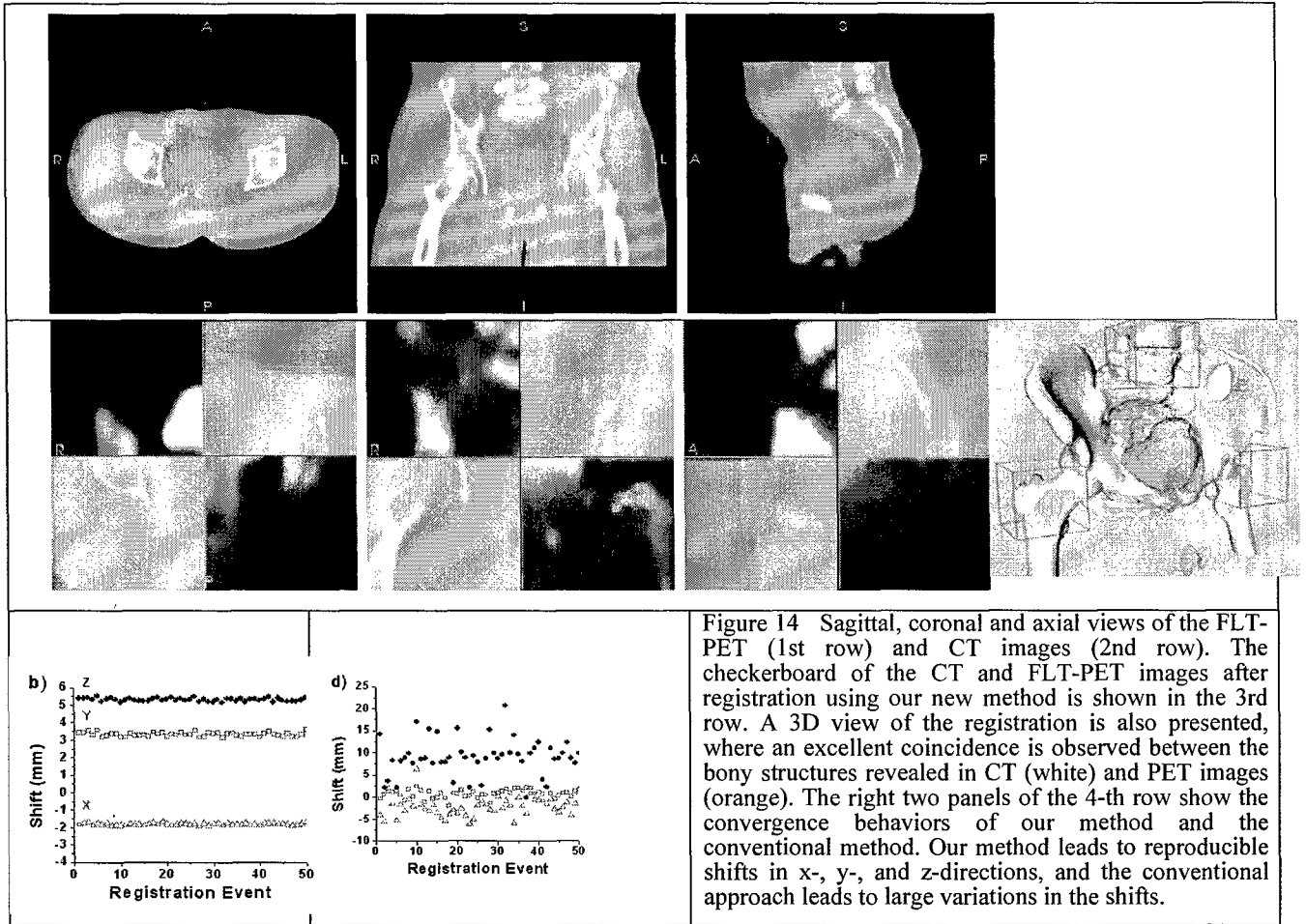


Figure 14 Sagittal, coronal and axial views of the FLT-PET (1st row) and CT images (2nd row). The checkerboard of the CT and FLT-PET images after registration using our new method is shown in the 3rd row. A 3D view of the registration is also presented, where an excellent coincidence is observed between the bony structures revealed in CT (white) and PET images (orange). The right two panels of the 4-th row show the convergence behaviors of our method and the conventional method. Our method leads to reproducible shifts in x-, y-, and z-directions, and the conventional approach leads to large variations in the shifts.

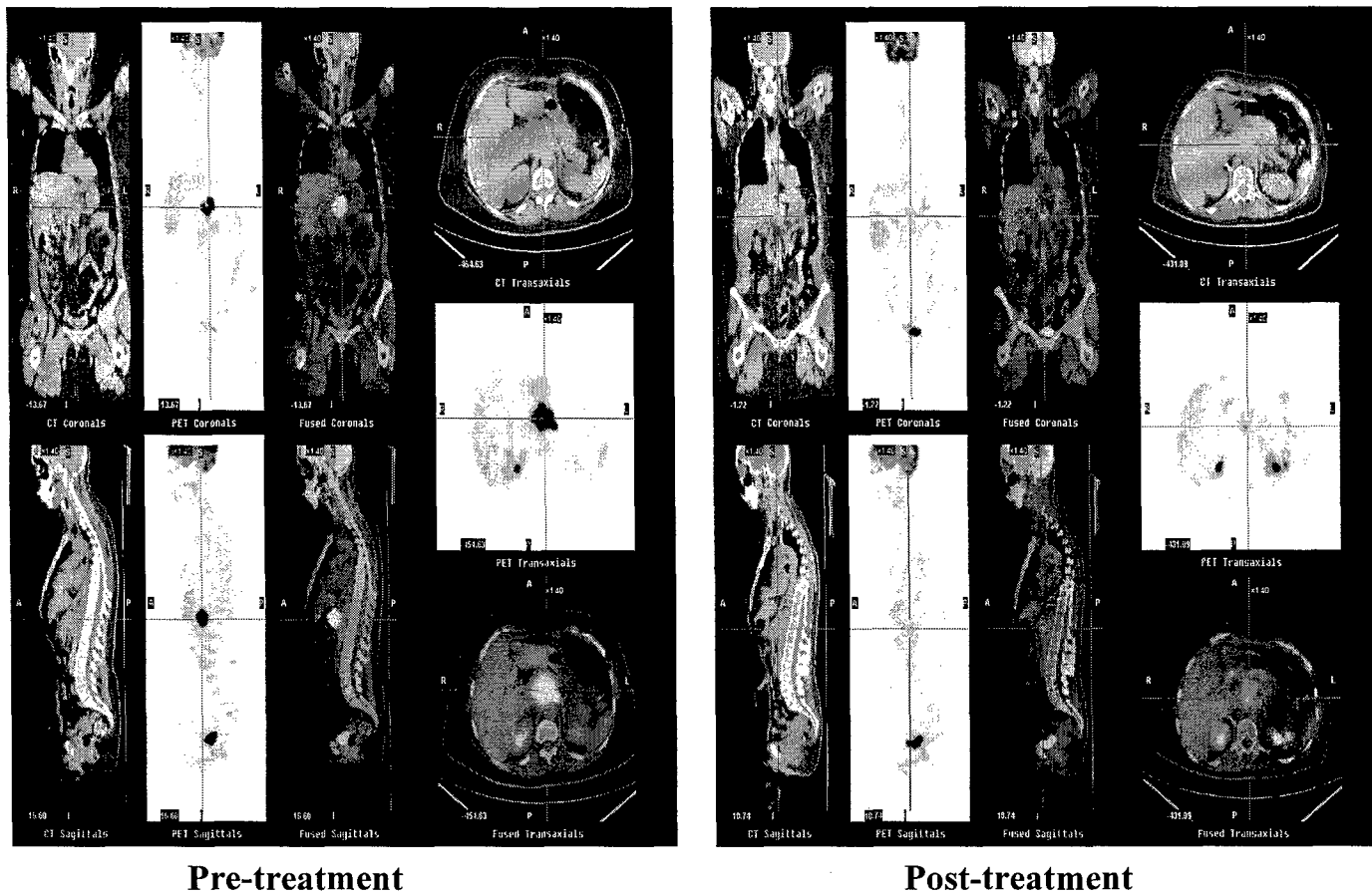


Figure 15 FDG-Pet images of a pancreatic patient before and after radiation therapy.

1. IMRT Collaborative Working Group, Intensity-modulated radiotherapy: current status and issues of interest. *International Journal of Radiation Oncology, Biology, Physics* **2001**, 51, (4), 880-914.
2. Ezzell, G. A.; Galvin, J. M.; Low, D.; Palta, J. R.; Rosen, I.; Sharpe, M. B.; Xia, P.; Xiao, Y.; Xing, L.; Yu, C. X., Guidance document on delivery, treatment planning, and clinical implementation of IMRT: report of the IMRT Subcommittee of the AAPM Radiation Therapy Committee. *Med Phys* **2003**, 30, (8), 2089-115.
3. Galvin, J. M.; Ezzell, G.; Eisbrauch, A.; Yu, C.; Butler, B.; Xiao, Y.; Rosen, I.; Rosenman, J.; Sharpe, M.; Xing, L.; Xia, P.; Lomax, T.; Low, D. A.; Palta, J., Implementing IMRT in clinical practice: a joint document of the American Society for Therapeutic Radiology and Oncology and the American Association of Physicists in Medicine. *Int J Radiat Oncol Biol Phys* **2004**, 58, (5), 1616-34.
4. Hamilton, R. J.; Sweeney, P. J.; Pelizzari, C. A.; Yetkin, F. Z.; Holman, B. L.; Garada, B.; Weichselbaum, R. R.; Chen, G. T., Functional imaging in treatment planning of brain lesions. *Int J Radiat Oncol Biol Phys* **1997**, 37, (1), 181-8.
5. Sawada, A.; Yoda, K.; Kokubo, M.; Kunieda, T.; Nagata, Y.; Hiraoka, M., A technique for noninvasive respiratory gated radiation treatment system based on a real time 3D ultrasound image correlation: a phantom study. *Med Phys* **2004**, 31, (2), 245-50.
6. Molloy, J. A.; Srivastava, S.; Schneider, B. F., A method to compare supra-pubic ultrasound and CT images of the prostate: technique and early clinical results. *Med Phys* **2004**, 31, (3), 433-42.
7. Chen, Y.; Boyer, A. L.; Xing, L., A dose-volume histogram based optimization algorithm for ultrasound guided prostate implants. *Medical Physics* **2000**, 27, (10), 2286-92.
8. Yu, Y.; Anderson, L. L.; Li, Z.; Mellenberg, D. E.; Nath, R.; Schell, M. C.; Waterman, F. M.; Wu, A.; Blasko, J. C., Permanent prostate seed implant brachytherapy: report of the American Association of Physicists in Medicine Task Group No. 64. *Medical Physics* **1999**, 26, (10), 2054-76.
9. Liang, B. C.; Thornton, A. F., Jr.; Sandler, H. M.; Greenberg, H. S., Malignant astrocytomas: focal tumor recurrence after focal external beam radiation therapy. *J Neurosurg* **1991**, 75, (4), 559-63.
10. Wallner, K. E.; Galicich, J. H.; Malkin, M. G.; Arbit, E.; Krol, G.; Rosenblum, M. K., Inability of computed tomography appearance of recurrent malignant astrocytoma to predict survival following reoperation. *J Clin Oncol* **1989**, 7, (10), 1492-6.
11. Pirzkall, A.; McKnight, T. R.; Graves, E. E.; Carol, M. P.; Sneed, P. K.; Wara, W. W.; Nelson, S. J.; Verhey, L. J.; Larson, D. A., MR-spectroscopy guided target delineation for high-grade gliomas. *International Journal of Radiation Oncology, Biology, Physics* **2001**, 50, (4), 915-28.
12. Nelson, S. J.; Graves, E.; Pirtzall, A.; Li, X.; Chan, A. A.; Vigneron, D. B.; McKnight, T. R., In Vivo Molecular Imaging for Planning Radiation Therapy of Gliomas: an Application of 1H MRSI. *Journal of Magnetic Resonance Imaging* **2002**, 16, 464-476.
13. Nelson, S. J.; Henry, R. G.; Day, M. R.; Wald, L. L.; Star-Lack, J.; Vigneron, D. B.; Noworolski, S. M., High spatial resolution 1H-MRSI and segmented MRI of cortical gray matter and subcortical white matter in three regions of the human brain. *Magnetic Resonance in Medicine* **1999**, 41, (1), 21-9.
14. Kurhanewicz, J.; Hricak, H.; Sokolov, D. L.; Huang, L. R.; Nelson, S. J.; Vigneron, D. B.; Scheidler, J., Prostate cancer: localization with three-dimensional proton MR spectroscopic imaging--clinicopathologic study. *Radiology* **1998**, 206, (3), 785-90.
15. DiBiase, S. J.; Hosseinzadeh, K.; Gullapalli, R. P.; Jacobs, S. C.; Naslund, M. J.; Sklar, G. N.; Alexander, R. B.; Yu, C., Magnetic resonance spectroscopic imaging-guided brachytherapy for localized prostate cancer. *Int J Radiat Oncol Biol Phys* **2002**, 52, (2), 429-38.
16. Kim, D. H.; Margolis, D.; Xing, L.; Daniel, B.; Spielman, D., In vivo prostate magnetic resonance spectroscopic imaging using two-dimensional J-resolved PRESS at 3 T. *Magn Reson Med* **2005**, 53, 1177-82.
17. Zaider, M.; Zelefsky, M. J.; Lee, E. K.; Zakian, K. L.; Amols, H. I.; Dyke, J.; Cohen, G.; Hu, Y.; Endi, A. K.; Chui, C.; Koutcher, J. A., Treatment planning for prostate implants using magnetic-resonance spectroscopy imaging. *International Journal of Radiation Oncology, Biology, Physics* **2000**, 47, (4), 1085-96.

18. Hunjan, S.; Gibbs, I.; Spielman, D. M.; Adalsteinsson, E.; Xing, L., Validating Magnetic Resonance Spectroscopic Imaging for Radiation Therapy Guidance. *International Journal of Radiation Oncology, Biology, Physics* **2002**, *54*, (2), 29.
19. Townsend, D. W.; Carney, J. P.; Yap, J. T.; Hall, N. C., PET/CT Today and Tomorrow. *The Journal of Nuclear Medicine* **2004**, *45*, 4S-14S.
20. Czernin, J.; Schelbert, H., PET/CT Imaging, Facts, Options, Hopes, and Questions. *The Journal of Nuclear Medicine* **2004**, *45*, 1S-3S.
21. Hicks, R. J.; Kalff, V.; MacManus, M. P.; Ware, R. E.; Hogg, A.; McKenzie, A. F.; Matthews, J. P.; Ball, D. L., (18)F-FDG PET provides high-impact and powerful prognostic stratification in staging newly diagnosed non-small cell lung cancer. *Journal of Nuclear Medicine* **2001**, *42*, (11), 1596-604.
22. Mac Manus, M. P.; Hicks, R. J.; Ball, D. L.; Kalff, V.; Matthews, J. P.; Salminen, E.; Khaw, P.; Wirth, A.; Rischin, D.; McKenzie, A., F-18 fluorodeoxyglucose positron emission tomography staging in radical radiotherapy candidates with nonsmall cell lung carcinoma: powerful correlation with survival and high impact on treatment. *Cancer* **2001**, *92*, (4), 886-95.
23. Bradley, J. D.; Dehdashti, F.; Mintun, M. A.; Govindan, R.; Trinkaus, K.; Siegel, B. A.; Welsh, J. S., Positron emission tomography in limited-stage small-cell lung cancer: a prospective study. *Journal of Clinical Oncology* **2004**, *22*, (16), 3248-54.
24. Bradley, K.; Ruchala, K. J.; Mackie, T. R.; Manon, R.; Patel, R.; Wiederholt, P.; Lock, M.; Hui, S.; Mehta, M. P.; Bradley, J., Impact of FDG-PET on radiation therapy volume delineation in non-small-cell lung cancer.[see comment]. *Clinical Lung Cancer* **2004**, *5*, (5), 303-6.
25. Howard, A.; Mehta, M. P.; Ritter, M. A.; Bradley, K. A.; Tome, W. A.; Chappell, R. J.; Manon, R. R.; Allen, G. W., The value of PET/CT in gross tumor volume delineation in lung and esophagus cancer. *International Journal of Radiation Oncology, Biology, Physics* **2004**, *60*, S536-537.
26. Effert, P. J.; Bares, R.; Handt, S.; Wolff, J. M.; Bèull, U.; Jakse, G., Metabolic imaging of untreated prostate cancer by positron emission tomography with 18fluorine-labeled deoxyglucose. *J Urol* **1996**, *155*, (3), 994-8.
27. Hofer, C.; Laubenbacher, C.; Block, T.; Breul, J.; Hartung, R.; Schwaiger, M., Fluorine-18-fluorodeoxyglucose positron emission tomography is useless for the detection of local recurrence after radical prostatectomy. *Eur Urol* **1999**, *36*, (1), 31-5.
28. Liu, I. J.; Zafar, M. B.; Lai, Y. H.; Segall, G. M.; Terris, M. K., Fluorodeoxyglucose positron emission tomography studies in diagnosis and staging of clinically organ-confined prostate cancer. *Urology* **2001**, *57*, (1), 108-11.
29. Hoh, C. K.; Seltzer, M. A.; Franklin, J.; deKernion, J. B.; Phelps, M. E.; Belldegrun, A., Positron emission tomography in urological oncology. *J Urol* **1998**, *159*, (2), 347-56.
30. Gambhir, S. S.; Srinivasan, A.; Banerjee, P. K.; Hoh, C. K.; Cherry, S. R.; Sharfstein, S.; Barrio, J. R.; Herschman, H. R.; Phelps, M. E., PET in oncology: will it replace the other modalities? *Journal of Nuclear Medicine* **1998**, *39*, (4), 729-34.
31. Czernin, J.; Phelps, M. E., Positron emission tomography scanning: current and future applications. *Annu Rev Med* **2002**, *53*, 89-112.
32. Gambhir, S. S., Molecular imaging of cancer with positron emission tomography. *Nat Rev Cancer* **2002**, *2*, (9), 683-93.
33. Thornbury, J. R.; Ornstein, D. K.; Choyke, P. L.; Langlotz, C. P.; Weinreb, J. C., Prostate cancer: what is the future role for imaging? *AJR Am J Roentgenol* **2001**, *176*, (1), 17-22.
34. Schèoder, H.; Larson, S. M., Positron emission tomography for prostate, bladder, and renal cancer. *Semin Nucl Med* **2004**, *34*, (4), 274-92.
35. Shields, A. F.; Grierson, J. R.; Dohmen, B. M.; Machulla, H. J.; Stayanoff, J. C.; Lawhorn-Crews, J. M.; Obradovich, J. E.; Muzik, O.; Mangner, T. J., Imaging proliferation in vivo with [F-18]FLT and positron emission tomography. *Nature Medicine* **1998**, *4*, (11), 1334-6.
36. Buck, A. K.; Schirrmeister, H.; Hetzel, M.; Von Der Heide, M.; Halter, G.; Glatting, G.; Mattfeldt, T.; Liewald, F.; Reske, S. N.; Neumaier, B., 3-deoxy-3-[(18)F]fluorothymidine-positron emission tomography for noninvasive assessment of proliferation in pulmonary nodules. *Cancer Research* **2002**, *62*, (12), 3331-4.

37. Buck, A. K.; Halter, G.; Schirrmeister, H.; Kotzerke, J.; Wurziger, I.; Glatting, G.; Mattfeldt, T.; Neumaier, B.; Reske, S. N.; Hetzel, M., Imaging proliferation in lung tumors with PET: 18F-FLT versus 18F-FDG. *Journal of Nuclear Medicine* **2003**, *44*, (9), 1426-31.
38. Smyczek-Gargya, B.; Fersis, N.; Dittmann, H.; Vogel, U.; Reischl, G.; Machulla, H. J.; Wallwiener, D.; Bares, R.; Dohmen, B. M., PET with [18F]fluorothymidine for imaging of primary breast cancer: a pilot study. *European Journal of Nuclear Medicine and Molecular Imaging* **31**, (5), 720-724.
39. Shreve, P. D.; Gross, M. D., Imaging of the pancreas and related diseases with PET carbon-11-acetate. *Journal of nuclear medicine* **1997**, *38*(8), 1305-10.
40. Seltzer, M. A.; Jahan, S. A.; Sparks, R.; Stout, D. B.; Satyamurthy, N.; Dahlbom, M.; Phelps, M. E.; Barrio, J. R.; DeJesus, O. T., Radiation dose estimates in humans for (11)C-acetate whole-body PET. *Journal of nuclear medicine: official publication, Society of Nuclear Medicine*. **2004**, *45*(7), 1233-6.
41. Jager, P. L.; Que, T. H.; Vaalburg, W.; Pruim, J.; Elsinga, P.; Plukker, J. T.; Pet Centre, G. U. H. P. O. B. R. B. G. T. N. p. l. j. n. a. n., Carbon-11 choline or FDG-PET for staging of oesophageal cancer? *European journal of nuclear medicine*. **2001**, *28*(12), 1845-9.
42. Ishiwata, K.; Kasahara, C.; Hatano, K.; Ishii, S.; Senda, M., Carbon-11 labeled ethionine and propionine as tumor detecting agents. *Annals of nuclear medicine*. **1997**, *11*(2), 115-22.
43. Iozzo, P.; Osman, S.; Glaser, M.; Knickmeier, M.; Ferrannini, E.; Pike, V. W.; Camici, P. G.; Law, M. P., In vivo imaging of insulin receptors by PET: preclinical evaluation of iodine-125 and iodine-124 labelled human insulin. *Nuclear medicine and biology*. **2002**, *29*(1), 73-82.
44. Herlin, G.; Persson, B.; Bergström, M.; Lêangström, B.; Aspelin, P., 11C-harmine as a potential PET tracer for ductal pancreas cancer: in vitro studies. *European radiology*. **2003**, *13*(4), 729-33.
45. Brown, W. D.; Oakes, T. R.; DeJesus, O. T.; Taylor, M. D.; Roberts, A. D.; Nickles, R. J.; Holden, J. E., Fluorine-18-fluoro-L-DOPA dosimetry with carbidopa pretreatment. *Journal of nuclear medicine* **1998**, *39*(11), 1884-91.
46. Blankenberg, F. G.; Strauss, H. W., Nuclear medicine applications in molecular imaging. *Journal of Magnetic Resonance Imaging* **2002**, *16*, (4), 352-61.
47. Oyama, N.; Akino, H.; Kanamaru, H.; Suzuki, Y.; Muramoto, S.; Yonekura, Y.; Sadato, N.; Yamamoto, K.; Okada, K., 11C-acetate PET imaging of prostate cancer. *J Nucl Med* **2002**, *43*, (2), 181-6.
48. Oyama, N.; Miller, T. R.; Dehdashti, F.; Siegel, B. A.; Fischer, K. C.; Michalski, J. M.; Kibel, A. S.; Andriole, G. L.; Picus, J.; Welch, M. J., 11C-acetate PET imaging of prostate cancer: detection of recurrent disease at PSA relapse. *J Nucl Med* **2003**, *44*, (4), 549-55.
49. Kotzerke, J.; Volkmer, B. G.; Glatting, G.; van den Hoff, J.; Gschwend, J. E.; Messer, P.; Reske, S. N.; Neumaier, B., Intraindividual comparison of [11C]acetate and [11C]choline PET for detection of metastases of prostate cancer. *Nuklearmedizin* **2003**, *42*, (1), 25-30.
50. Mathews, D.; Oz, O. K., Positron emission tomography in prostate and renal cell carcinoma. *Curr Opin Urol* **2002**, *12*, (5), 381-5.
51. DeGrado, T. R.; Baldwin, S. W.; Wang, S.; Orr, M. D.; Liao, R. P.; Friedman, H. S.; Reiman, R.; Price, D. T.; Coleman, R. E., Synthesis and evaluation of (18)F-labeled choline analogs as oncologic PET tracers. *J Nucl Med* **2001**, *42*, (12), 1805-14.
52. Hara, T.; Kosaka, N.; Kishi, H., Development of (18)F-fluoroethylcholine for cancer imaging with PET: synthesis, biochemistry, and prostate cancer imaging. *J Nucl Med* **2002**, *43*, (2), 187-99.
53. Hara, T.; Kosaka, N.; Kishi, H., PET imaging of prostate cancer using carbon-11-choline. *J Nucl Med* **1998**, *39*, (6), 990-5.
54. Kotzerke, J.; Prang, J.; Neumaier, B.; Volkmer, B.; Guhlmann, A.; Kleinschmidt, K.; Hautmann, R.; Reske, S. N., Experience with carbon-11 choline positron emission tomography in prostate carcinoma. *Eur J Nucl Med* **2000**, *27*, (9), 1415-9.
55. Sutinen, E.; Nurmi, M.; Roivainen, A.; Varpula, M.; Tolvanen, T.; Lehtikoinen, P.; Minn, H., Kinetics of [(11)C]choline uptake in prostate cancer: a PET study. *Eur J Nucl Med Mol Imaging* **2004**, *31*, (3), 317-24.
56. Chen, X.; Park, R.; Hou, Y.; Tohme, M.; Shahinian, A. H.; Bading, J. R.; Conti, P. S., microPET and autoradiographic imaging of GRP receptor expression with 64Cu-DOTA-[Lys3]bombesin in human prostate adenocarcinoma xenografts. *J Nucl Med* **2004**, *45*, (8), 1390-7.

57. Rasey, J. S.; Koh, W. J.; Evans, M. L.; Peterson, L. M.; Lewellen, T. K.; Graham, M. M.; Krohn, K. A., Quantifying regional hypoxia in human tumors with positron emission tomography of [¹⁸F]fluoromisonidazole: a pretherapy study of 37 patients. *Int J Radiat Oncol Biol Phys* **1996**, *36*, (2), 417-28.
58. Rajendran, J. G.; Wilson, D. C.; Conrad, E. U.; Peterson, L. M.; Bruckner, J. D.; Rasey, J. S.; Chin, L. K.; Hofstrand, P. D.; Grierson, J. R.; Eary, J. F.; Krohn, K. A., [(¹⁸F)]FMISO and [(¹⁸F)]FDG PET imaging in soft tissue sarcomas: correlation of hypoxia, metabolism and VEGF expression. *Eur J Nucl Med Mol Imaging* **2003**, *30*, (5), 695-704.
59. O'Donoghue, J. A.; Zanzonico, P.; Pugachev, A.; Wen, B.; Smith-Jones, P.; Cai, S.; Burnazi, E.; Finn, R. D.; Burgman, P.; Ruan, S.; Lewis, J. S.; Welch, M. J.; Ling, C. C.; Humm, J. L., Assessment of regional tumor hypoxia using ¹⁸F-fluoromisonidazole and ⁶⁴Cu(II)-diacetyl-bis(N4-methylthiosemicarbazone) positron emission tomography: Comparative study featuring microPET imaging, Po₂ probe measurement, autoradiography, and fluorescent microscopy in the R3327-AT and FaDu rat tumor models. *Int J Radiat Oncol Biol Phys* **2005**, *61*, (5), 1493-502.
60. Piert, M.; Machulla, H. J.; Picchio, M.; Reischl, G.; Ziegler, S.; Kumar, P.; Wester, H. J.; Beck, R.; McEwan, A. J.; Wiebe, L. I.; Schwaiger, M., Hypoxia-specific tumor imaging with ¹⁸F-fluoroazomycin arabinoside. *J Nucl Med* **2005**, *46*, (1), 106-13.
61. Chao, K. S.; Mutic, S.; Gerber, R. L.; Perez, C. A.; Purdy, J. A., A novel approach to overcome hypoxic tumor resistance: Cu-ATSM-guided intensity-modulated radiation therapy. *International Journal of Radiation Oncology, Biology, Physics* **2001**, *49*, (3), 1171-82.
62. Hara, T., ¹¹C-choline and 2-deoxy-2-[¹⁸F]fluoro-D-glucose in tumor imaging with positron emission tomography. *Mol Imaging Biol* **2002**, *4*, (4), 267-73.
63. Zeisel, S. H., Dietary choline: biochemistry, physiology, and pharmacology. *Annu Rev Nutr* **1981**, *1*, 95-121.
64. de Jong, I. J.; Pruim, J.; Elsinga, P. H.; Vaalburg, W.; Mensink, H. J., ¹¹C-choline positron emission tomography for the evaluation after treatment of localized prostate cancer. *Eur Urol* **2003**, *44*, (1), 32-8; discussion 38-9.
65. Kotzerke, J.; Gschwend, J. E.; Neumaier, B., PET for prostate cancer imaging: still a quandary or the ultimate solution? *J Nucl Med* **2002**, *43*, (2), 200-2.
66. Ling, C. C.; Humm, J.; Larson, S.; Amols, H.; Fuks, Z.; Leibel, S.; Koutcher, J. A., Towards multidimensional radiotherapy (MD-CRT): biological imaging and biological conformality. *International Journal of Radiation Oncology, Biology, Physics* **2000**, *47*, (3), 551-560.
67. Brahme, A., Individualizing cancer treatment: biological optimization models in treatment planning and delivery. *International Journal of Radiation Oncology, Biology, Physics* **2001**, *49*, (2), 327-37.
68. Xing, L.; Cotrutz, C.; Hunjan, S.; Boyer, A. L.; Adalsteinsson, E.; Spielman, D. M., Inverse Planning for Functional Image-Guided IMRT. *Physics in Medicine & Biology* **2002**, *47*, (10), 3567-3578.
69. Alber, M.; Paulsen, F.; Eschman, S. M.; Machulla, H. J., On biologically conformal boost dose optimization. *Physics in Medicine & Biology* **2003**, *48*, (10), N31-N35.
70. Yang, Y.; Xing, L., Towards biologically conformal radiation therapy (BCRT): Selective IMRT dose escalation under the guidance of spatial biology distribution. *Medical Physics* **2005**, *32*, 1473-1484.
71. Seppenwoolde, Y.; Shirato, H.; Kitamura, K.; Shimizu, S.; van Herk, M.; Lebesque, J. V.; Miyasaka, K., Precise and real-time measurement of 3D tumor motion in lung due to breathing and heartbeat, measured during radiotherapy. *International journal of radiation oncology, biology, physics* **2002**, *53*, (4), 822.
72. Shirato, H.; Shimizu, S.; Kunieda, T.; Kitamura, K.; van Herk, M.; Kagei, K.; Nishioka, T.; Hashimoto, S.; Fujita, K.; Aoyama, H.; Tsuchiya, K.; Kudo, K.; Miyasaka, K., Physical aspects of a real-time tumor-tracking system for gated radiotherapy. *Int J Radiat Oncol Biol Phys* **2000**, *48*, (4), 1187-95.
73. Shirato, H.; Seppenwoolde, Y.; Kitamura, K.; Onimura, R.; Shimizu, S., Intrafractional tumor motion: lung and liver. *Semin Radiat Oncol* **2004**, *14*, (1), 10-8.
74. Shimizu, S.; Shirato, H.; Ogura, S.; Akita-Dosaka, H.; Kitamura, K.; Nishioka, T.; Kagei, K.; Nishimura, M.; Miyasaka, K., Detection of lung tumor movement in real-time tumor-tracking radiotherapy. *Int J Radiat Oncol Biol Phys* **2001**, *51*, (2), 304-10.

75. Shimizu, S.; Shirato, H.; Kagei, K.; Nishioka, T.; Bo, X.; Dosaka-Akita, H.; Hashimoto, S.; Aoyama, H.; Tsuchiya, K.; Miyasaka, K., Impact of respiratory movement on the computed tomographic images of small lung tumors in three-dimensional (3D) radiotherapy. *Int J Radiat Oncol Biol Phys* **2000**, *46*, (5), 1127-33.
76. Xu, Q.; Hamilton, R., Novel Respiratory Gating Method Based On Automated Analysis of Ultrasonic Diaphragm Motion. *Medical Physics* **2005**, *32*, 2124.
77. Huang, M. H.; Lin, Y. S.; Lee, C. L.; Yang, R. C., Use of ultrasound to increase effectiveness of isokinetic exercise for knee osteoarthritis. *Arch Phys Med Rehabil* **2005**, *86*, (8), 1545-51.
78. Seiler, P. G.; Blattmann, H.; Kirsch, S.; Muench, R. K.; Schilling, C., A novel tracking technique for the continuous precise measurement of tumour positions in conformal radiotherapy. *Phys Med Biol* **2000**, *45*, (9), N103-10.
79. Balter, J. M.; Wright, J. N.; Newell, L. J.; Friemel, B.; Dimmer, S.; Cheng, Y.; Wong, J.; Vertatschitsch, E.; Mate, T. P., Accuracy of a wireless localization system for radiotherapy. *Int J Radiat Oncol Biol Phys* **2005**, *61*, (3), 933-7.
80. Nehmeh, S. A.; Erdi, Y. E.; Pan, T.; Pevsner, A.; Rosenzweig, K. E.; Yorke, E.; Mageras, G. S.; Schoder, H.; Vernon, P.; Squire, O.; Mostafavi, H.; Larson, S. M.; Humm, J. L., Four-dimensional (4D) PET/CT imaging of the thorax. *Medical physics* **2004**, *31*, (12), 3179.
81. Thorndyke, B.; Schreiber, E.; Maxim, P.; Loo, B.; Boyer, A.; A., K.; Xing, L. In *Enhancing 4D PET through retrospective stacking*, Oral presentation in 2005 Annual Meeting of American Association of Physicists in Medicine, Seattle, WA, 2005, 2005; Seattle, WA, 2005.
82. Thorndyke, B.; Schreiber, E.; Koong, A.; Xing, L., Reducing motion artifacts in PET through retrospective stacking. *Int J Radiat Oncol Biol Phys* **2005**, submitted.
83. Vedam, S. S.; Keall, P. J.; Kini, V. R.; Mostafavi, H.; Shukla, H. P.; Mohan, R., Acquiring a four-dimensional computed tomography dataset using an external respiratory signal. *Physics in Medicine and Biology* **2003**, *48*, (1), 45.
84. Keall, P. J.; Starkschall, G.; Shukla, H.; Forster, K. M.; Ortiz, V.; Stevens, C. W.; Vedam, S. S.; George, R.; Guerrero, T.; Mohan, R., Acquiring 4D thoracic CT scans using a multislice helical method. *Phys Med Biol* **2004**, *49*, (10), 2053-67.
85. Low, D. A.; Nystrom, M.; Kalinin, E.; Parikh, P.; Dempsey, J. F.; Bradley, J. D.; Mutic, S.; Wahab, S. H.; Islam, T.; Christensen, G.; Polite, D. G.; Whiting, B. R., A method for the reconstruction of four-dimensional synchronized CT scans acquired during free breathing. *Med Phys* **2003**, *30*, (6), 1254-63.
86. Rietzel, E.; Pan, T.; Chen, G. T. Y., Four-dimensional computed tomography: Image formation and clinical protocol. *Medical Physics* **2005**, *32*, (4), 874.
87. Li, T.; schreiber, E.; Thorndyke, B.; Xing, L., Radiation dose reduction in 4D CT. *Medical Physics* **2005**, submitted.
88. Kubo, H. D.; Len, P. M.; Minohara, S.; Mostafavi, H., Breathing-synchronized radiotherapy program at the University of California Davis Cancer Center. *Medical physics* **2000**, *27*, (2), 346.
89. Rueckert, D.; Sonoda, L. I.; Hayes, C.; Hill, D. L.; Leach, M. O.; Hawkes, D. J., Nonrigid registration using free-form deformations: application to breast MR images. *IEEE Trans Med Imaging* **1999**, *18*, 712-21.
90. Pan, T.; Lee, T.-Y.; Rietzel, E.; Chen, G. T. Y., 4D-CT imaging of a volume influenced by respiratory motion on multi-slice CT. *Medical Physics* **2004**, *31*, (2), 333.
91. Kini, V. R.; Vedam, S. S.; Keall, P. J.; Patil, S.; Chen, C.; Mohan, R., Patient training in respiratory-gated radiotherapy. *Medical Dosimetry* **2003**, *28*, (1), 7.
92. Wong, J. W.; Sharpe, M. B.; Jaffray, D. A.; Kini, V. R.; Robertson, J. M.; Stromberg, J. S.; Martinez, A. A., The use of active breathing control (ABC) to reduce margin for breathing motion. *International journal of radiation oncology, biology, physics* **1999**, *44*, (4), 911.
93. Frazier, R. C.; Vicini, F. A.; Sharpe, M. B.; Yan, D.; Fayad, J.; Baglan, K. L.; Kestin, L. L.; Remouchamps, V. M.; Martinez, A. A.; Wong, J. W., Impact of breathing motion on whole breast radiotherapy: a dosimetric analysis using active breathing control. *Int J Radiat Oncol Biol Phys* **2004**, *58*, (4), 1041-7.

94. Dawson, L. A.; Brock, K. K.; Kazanjian, S.; Fitch, D.; McGinn, C. J.; Lawrence, T. S.; Ten Haken, R. K.; Balter, J., The reproducibility of organ position using active breathing control (ABC) during liver radiotherapy. *Int J Radiat Oncol Biol Phys* **2001**, 51, (5), 1410-21.
95. Starkschall, G.; Himanshu, S.; Keall, P. J.; Antolak, J. A.; Mohan, R. In *Displacement-based Binning of 4-D CT Image Data Sets*, XIVth ICCR, 2004; 2004; p 53.
96. Thorndyke, B.; Schreibmann, E.; Li, T.; Boyer, A.; Xing, L., A Comparison of Amplitude- and Phase-Based 4D CT. *Medical Physics* **2005**, 32, (6), 1919.
97. Lu, W.; Parikh, P.; Bradley, J.; Low, D., TU-D-J-6C-01: A Comparison Between Amplitude Sorting and Phase Sorting Using External Respiratory Measurements for 4D CT. *Medical Physics* **2005**, 32, (6), 2094.
98. Schreibmann, E.; Chen, G. T. Y.; Xing, L., Image Interpolation in 4D CT Using a BSpline Deformable Registration Model. *International journal of radiation oncology, biology, physics* **2005**.
99. Schweikard, A.; Shiomi, H.; Fisseler, J.; Dötter, M.; Berlinger, K.; Gehl, H. B.; Adler, J., Fiducial-Less Respiration Tracking in Radiosurgery. *LNCS* **2004**, 3217, 992 - 999.
100. Rohlfing, T.; Maurer, C. R., Jr.; O'Dell, W. G.; Zhong, J., Modeling liver motion and deformation during the respiratory cycle using intensity-based nonrigid registration of gated MR images. *Med Phys* **2004**, 31, (3), 427-32.
101. Vedam, S. S.; Kini, V. R.; Keall, P. J.; Ramakrishnan, V.; Mostafavi, H.; Mohan, R., Quantifying the predictability of diaphragm motion during respiration with a noninvasive external marker. *Medical Physics* **2003**, 30, (4), 505.
102. Ford, E. C.; Mageras, G. S.; Yorke, E.; Rosenzweig, K. E.; Wagman, R.; Ling, C. C., Evaluation of respiratory movement during gated radiotherapy using film and electronic portal imaging. *International journal of radiation oncology, biology, physics* **2002**, 52, (2), 522.
103. Yorke, E.; Rosenzweig, K. E.; Wagman, R.; Mageras, G. S., Interfractional anatomic variation in patients treated with respiration-gated radiotherapy. *J.Appl.Clin.Med.Phys.* **2005**, 6, (2), 19.
104. Klein, G. J.; Reutter, B. W.; Ho, M. H.; Reed, J. H.; Huesman, R. H., Real-time system for respiratory-cardiac gating in positron tomography. *IEEE Transactions on Nuclear Science* **1998**, 45, (4), 2139.
105. Nehmeh, S. A.; Erdi, Y. E.; Ling, C. C.; Rosenzweig, K. E.; Schoder, H.; Larson, S. M.; Macapinlac, H. A.; Squire, O. D.; Humm, J. L., Effect of respiratory gating on quantifying PET images of lung cancer. *J Nucl Med* **2002**, 43, (7), 876-81.
106. Nehmeh, S. A.; Erdi, Y. E.; Rosenzweig, K. E.; Schoder, H.; Larson, S. M.; Squire, O. D.; Humm, J. L., Reduction of respiratory motion artifacts in PET imaging of lung cancer by respiratory correlated dynamic PET: methodology and comparison with respiratory gated PET. *Journal of nuclear medicine* **2003**, 44, 1644.
107. Cherry, S. R.; Dahlborn, M., Physics, Instrumentation and Scanners. In *PET: Molecular Imaging and Its Biological Applications*, Springer-Verlag: 2004.
108. Sarikaya, I.; Yeung, H. W.; Erdi, Y.; Larson, S. M., Respiratory artifact causing malpositioning of liver dome lesion in right lower lung. *Clinical nuclear medicine* **2003**, 28, (11), 943.
109. Erdi, Y. E.; Nehmeh, S. A.; Pan, T.; Pevsner, A.; Rosenzweig, K. E.; Mageras, G.; Yorke, E. D.; Schoder, H.; Hsiao, W.; Squire, O. D.; Vernon, P.; Ashman, J. B.; Mostafavi, H.; Larson, S. M.; Humm, J. L., The CT motion quantitation of lung lesions and its impact on PET-measured SUVs. *Journal of nuclear medicine: official publication, Society of Nuclear Medicine* **2004**, 45, (8), 1287.
110. Pevsner, A.; Nehmeh, S. A.; Humm, J. L.; Mageras, G. S.; Erdi, Y. E., Effect of motion on tracer activity determination in CT attenuation corrected PET images: A lung phantom study. *Medical Physics* **2005**, 32, (7), 2358.
111. Nehmeh, S. A.; Erdi, Y. E.; Pan, T.; Yorke, E.; Mageras, G. S.; Rosenzweig, K. E.; Schoder, H.; Mostafavi, H.; Squire, O.; Pevsner, A.; Larson, S. M.; Humm, J. L., Quantitation of respiratory motion during 4D-PET/CT acquisition. *Med Phys* **2004**, 31, (6), 1333-8.
112. Mattes, D.; Haynor, R. D.; Vesselle, H.; Lewellen, K. T.; Eubank, W., PET-CT image registration in the chest using free-form deformations. *IEEE Trans Med Imag* **2003**, 22, (1), 120-128.
113. Schreibmann, E.; Xing, L., Narrow Band Deformable Registration of Prostate MRI/MRSI and CT studies. *International Journal of Radiation Oncology, Biology, Physics* **2005**, 62, 595-605.

114. Li, T.; Thorndyke, B.; schreibmann, E.; Yang, Y.; Xing, L., Model-Based Image Reconstruction for Four-Dimensional PET. *Medical Physics* **2005**, submitted.
115. Trofimov, A.; Rietzel, E.; Lu, H. M.; Martin, B.; Jiang, S.; Chen, G. T.; Bortfeld, T., Temporo-spatial IMRT optimization: concepts, implementation and initial results. *Phys Med Biol* **2005**, 50, (12), 2779-98.
116. Armbruster, B.; Yang, Y.; Schreibmann, E.; Levy, D.; Xing, L. *Inverse planning for time-resolved aperture modulated radiation therapy*, 2005 Annual Meeting of ASTRO, Denver, CO, 2005.
117. Bortfeld, T.; Jiang, S. B.; Rietzel, E., Effects of motion on the total dose distribution. *Seminars in radiation oncology*. **2004**, 14(1), 41-51.
118. Jiang, S. B.; Pope, C.; Al Jarrah, K. M.; Kung, J. H.; Bortfeld, T.; Chen, G., An experimental investigation on intra-fractional organ motion effects in lung IMRT treatments. *Phys Med Biol* **2003**, 48, 1773-84.
119. Rietzel, E.; Chen, G. T.; Choi, N. C.; Willet, C. G., Four-dimensional image-based treatment planning: Target volume segmentation and dose calculation in the presence of respiratory motion. *International journal of radiation oncology, biology, physics* **2005**, 61, (5), 1535.
120. Keall, P. J.; Joshi, S.; Vedam, S. S.; Siebers, J. V.; Kini, V. R.; Mohan, R., Four-dimensional radiotherapy planning for DMLC-based respiratory motion tracking. *Med Phys* **2005**, 32, (4), 942-51.
121. Webb, S., The effect on IMRT conformality of elastic tissue movement and a practical suggestion for movement compensation via the modified dMLC technique. *Phys Med Biol* **2005**, 50, (6), 1163-90.
122. Yang, Y.; Xing, L., Clinical knowledge-based inverse treatment planning. *Phys Med Biol* **2004**, 49, (22), 5101-17.
123. Yang, Y.; Xing, L., Inverse treatment planning with adaptively evolving voxel-dependent penalty scheme. *Med Phys* **2004**, 31, (10), 2839-44.
124. Wu, Q.; Mohan, R.; Niemierko, A.; Schmidt-Ullrich, R., Optimization of intensity-modulated radiotherapy plans based on the equivalent uniform dose. *International Journal of Radiation Oncology, Biology, Physics* **2002**, 52, (1), 224-35.
125. Olivera, G. H.; Shepard, D. M.; Reckwerdt, P. J.; Ruchala, K.; Zachman, J.; Fitchard, E. E.; Mackie, T. R., Maximum likelihood as a common computational framework in tomotherapy. *Physics in Medicine & Biology* **1998**, 43, (11), 3277-94.
126. Lee, E. K.; Gallagher, R. J.; Silvern, D.; Wu, C. S.; Zaider, M., Treatment planning for brachytherapy: an integer programming model, two computational approaches and experiments with permanent prostate implant planning. *Physics in Medicine & Biology* **1999**, 44, (1), 145-65.
127. Shepard, D. M.; Earl, M. A.; Li, X. A.; Naqvi, S.; Yu, C., Direct aperture optimization: a turnkey solution for step-and-shoot IMRT. *Medical Physics* **2002**, 29, (6), 1007-18.
128. Bednarz, G.; Michalski, D.; Houser, C.; Huq, M. S.; Xiao, Y.; Anne, P. R.; Galvin, J. M., The use of mixed-integer programming for inverse treatment planning with pre-defined field segments. *Physics in Medicine & Biology* **2002**, 47, (13), 2235-45.
129. Cotrutz, C.; Xing, L., Segment-Based Dose Optimization Using a Genetic Algorithm. *Physics in Medicine & Biology* **2003**, 48, 2987-2998.
130. Murphy, M. J.; Adler, J., Jr; Bodduluri, M.; Dooley, J.; Forster, K.; Hai, J.; Le, Q.; Luxton, G.; Martin, D.; Poen, J., Image-guided radiosurgery for the spine and pancreas. *Comput Aided Surg* **2000**, 5, 278-88.
131. Murphy, M. J., Tracking moving organs in real time. *Semin Radiat Oncol* **2004**, 14, (1), 91-100.
132. Sharp, G. C.; Jiang, S. B.; Shimizu, S.; Shirato, H., Prediction of respiratory tumour motion for real-time image-guided radiotherapy. *Phys Med Biol* **2004**, 49, (3), 425-40.
133. Sharp, G. C.; Jiang, S. B.; Shimizu, S.; Shirato, H., Tracking errors in a prototype real-time tumour tracking system. *Phys Med Biol* **2004**, 49, (23), 5347-56.
134. Berbeco, R. I.; Neicu, T.; Rietzel, E.; Chen, G. T.; Jiang, S. B., A technique for respiratory-gated radiotherapy treatment verification with an EPID in cine mode. *Phys Med Biol* **2005**, 50, (16), 3669-79.
135. Berbeco, R. I.; Jiang, S. B.; Sharp, G. C.; Chen, G. T.; Mostafavi, H.; Shirato, H., Integrated radiotherapy imaging system (IRIS): design considerations of tumour tracking with linac gantry-mounted diagnostic x-ray systems with flat-panel detectors. *Phys Med Biol* **2004**, 49, (2), 243-55.
136. Boyer, A. L.; Antonuk, L.; Fenster, A.; Van Herk, M.; Meertens, H.; Munro, P.; Reinstein, L. E.; Wong, J., A review of electronic portal imaging devices (EPIDs). *Medical Physics* **1992**, 19, (1), 1-16.

137. Herman, M. G.; Balter, J. M.; Jaffray, D. A.; McGee, K. P.; Munro, P.; Shalev, S.; Van Herk, M.; Wong, J. W., Clinical use of electronic portal imaging: report of AAPM Radiation Therapy Committee Task Group 58. *Med Phys* **2001**, 28, (5), 712-37.
138. Yang, Y.; Xing, L., Quantitative Measurement of MLC Leaf Displacements Using an Electronic Portal Image Device. *Physics in Medicine and Biology* **2003**, 48.
139. Yan, D.; Wong, J.; Vicini, F.; Michalski, J.; Pan, C.; Frazier, A.; Horwitz, E.; Martinez, A., Adaptive modification of treatment planning to minimize the deleterious effects of treatment setup errors. *Int J Radiat Oncol Biol Phys* **1997**, 38, (1), 197-206.
140. Yan, D.; Ziaja, E.; Jaffray, D.; Wong, J.; Brabbins, D.; Vicini, F.; Martinez, A., The use of adaptive radiation therapy to reduce setup error: a prospective clinical study. *Int J Radiat Oncol Biol Phys* **1998**, 41, 715-20.
141. Court, L. E.; Dong, L.; Taylor, N.; Ballo, M.; Kitamura, K.; Lee, A. K.; O'Daniel, J.; White, R. A.; Cheung, R.; Kuban, D., Evaluation of a contour-alignment technique for CT-guided prostate radiotherapy: an intra- and interobserver study. *Int J Radiat Oncol Biol Phys* **2004**, 59, (2), 412-8.
142. Orton, N. P.; Tome, W. A., The impact of daily shifts on prostate IMRT dose distributions. *Med Phys* **2004**, 31, (10), 2845-8.
143. Fuss, M.; Salter, B. J.; Cavanaugh, S. X.; Fuss, C.; Sadeghi, A.; Fuller, C. D.; Ameduri, A.; Hevezi, J. M.; Herman, T. S.; Thomas, C. R., Jr., Daily ultrasound-based image-guided targeting for radiotherapy of upper abdominal malignancies. *Int J Radiat Oncol Biol Phys* **2004**, 59, (4), 1245-56.
144. Saw, C. B.; Ayyangar, K. M.; Zhen, W.; Yoe-Sein, M.; Pillai, S.; Enke, C. A., Clinical implementation of intensity-modulated radiation therapy. *Med Dosim* **2002**, 27, (2), 161-9.
145. Schweikard, A.; Glosser, G.; Bodduluri, M.; Murphy, M. J.; Adler, J. R., Robotic motion compensation for respiratory movement during radiosurgery. *Comput Aided Surg* **2000**, 5, (4), 263-77.
146. Mackie, T. R.; Balog, J.; Ruchala, K.; Shepard, D.; Aldridge, S.; Fitchard, E.; Reckwerdt, P.; Olivera, G.; McNutt, T.; Mehta, M., Tomotherapy. *Seminars in Radiation Oncology* **1999**, 9, (1), 108-17.
147. Meeks, S.; Harmon, J. J.; Langen, K.; R., W. T.; Wagner, T. H.; Kupelian, P., Performance characterization of megavoltage computed tomography imaging on a helical tomotherapy unit. *Medical Physics* **2005**, 32, 2673-2681.
148. Jaffray, D. A.; Siewerdsen, J. H.; Wong, J. W.; Martinez, A. A., Flat-panel cone-beam computed tomography for image-guided radiation therapy. *Int J Radiat Oncol Biol Phys* **2002**, 53, (5), 1337-49.
149. Pouliot, J.; Bani-Hashemi, A.; Chen, J.; Svatos, M.; Ghelmansarai, F.; Mitschke, M.; Aubin, M.; Xia, P.; Morin, O.; Bucci, K.; Roach, M., 3rd; Hernandez, P.; Zheng, Z.; Hristov, D.; Verhey, L., Low-dose megavoltage cone-beam CT for radiation therapy. *Int J Radiat Oncol Biol Phys* **2005**, 61, (2), 552-60.
150. Oldham, M.; Letourneau, D.; Watt, L.; Hugo, G.; Yan, D.; Lockman, D.; Kim, L. H.; Chen, P. Y.; Martinez, A.; Wong, J. W., Cone-beam-CT guided radiation therapy: A model for on-line application. *Radiother Oncol* **2005**, 75, (3), 271 E1-8.
151. Li, T.; Yang, Y.; Schreiber, E.; Xing, L. A new cone-beam CT reposition technique through deformable registration, Annual Meeting of American Association of Physicists in Medicine, Seattle, WA, 2005, 2005.
152. Mohan, R.; Zhang, X.; Wang, H.; Kang, Y.; Wang, X.; Liu, H.; Ang, K. K.; Kuban, D.; Dong, L., Use of deformed intensity distributions for on-line modification of image-guided IMRT to account for interfractional anatomic changes. *Int J Radiat Oncol Biol Phys* **2005**, 61, (4), 1258-66.
153. Yang, Y.; Li, T.; Schreiber, E.; Boyer, A. L.; Xing, L. *Is cone beam CT suitable for dose verification?* Annual Meeting of American Association of Physicists in Medicine, Seattle, WA, 2005.
154. Yang, Y.; Li, T.; Schreiber, E.; Xing, L., Mapping electron density distribution from planning CT to cone-beam CT (CBCT): a novel strategy for accurate dose calculation based on CBCT. *Medical Physics* **2005**, submitted.
155. Wang, G.; Vannier, M. W., Preliminary study on helical CT algorithms for patient motion estimation and compensation. *IEEE Trans. Med. Imaging* **1995**, 14, (10), 205-211.
156. Willis, N. P.; Bresler, Y., Optimal scan for time-varying tomography I: Theoretical analysis and fundamental limitations. *IEEE Trans. Med. Imaging* **1995**, 14, 642-653.

157. Atalar, E.; Onural, L., A respiratory motion artifact reduction method in magnetic resonance imaging of the chest. *IEEE Trans. Med. Imaging* **1991**, *10*, 11-24.
158. Crawford, C.; King, K. F.; Ritchie, C. J.; Godwin, J. D., Respiratory compensation in projection imaging using a magnification and displacement model. *IEEE Trans. Med. Imaging* **1996**, *15*, 327-332.
159. Li, T.; schreibmann, E.; Yang, Y.; Xing, L., Respiratory Motion Correction with Deformation Field for Improved On-Board Imaging with Cone-Beam CT. *Physics in Medicine and Biology* **2005**, submitted.
160. Sonke, J. J.; Zijp, L.; Remeijer, P.; van Herk, M., Respiratory correlated cone beam CT. *Med Phys* **2005**, *32*, (4), 1176-86.
161. Zeng, R.; Fessler, J. A.; Balter, J. M., Respiratory motion estimation from slowly rotating x-ray projections: theory and simulation. *Med Phys* **2005**, *32*, (4), 984-91.
162. Court, L. E.; Dong, L., Automatic registration of the prostate for computed-tomography-guided radiotherapy. *Medical Physics* **2003**, *30*, (10), 2750-2757.
163. Bharath, A.; Hirose, M.; Hata, N.; Warfield, S. K.; Ferrant, M.; Zou, K. H.; Suarez-Santan, E.; Ruiz-Alzola, J.; D'Amico, A.; Cormack, R. A.; Kikinis, R.; Jolesz, F. A.; Tempany, C. M., Evaluation of three-dimensional finite element-based deformable registration of pre- and intraoperative prostate imaging. *Medical Physics* **2001**, *28*, (12), 2551-60.
164. Brock, K. K.; McShan, D. L.; Balter, J. M., A comparison of computer-controlled versus manual on-line patient setup adjustment. *J Appl Clin Med Phys* **2002**, *3*, (3), 241-7.
165. Bookstein, F. L., Thin plate splines and the decomposition of deformations. *IEEE Trans. Pattern Anal. Mach. Intell.* **1989**, *11*, 567-585.
166. Lian, J.; Xing, L.; Hunjan, S.; Dumoulin, C.; Levin, J.; Lo, A.; Watkins, R.; Rohling, R. K.; Giaquinto, R.; Kim, D.; Spielman, S.; Daniel, B., Mapping of the Prostate in Endorectal Coil-Based MRI/MRSI and CT: a Deformable Registration and Validation Study. *Medical Physics* **2003**, *31*, in press.
167. Guerrero, T.; Zhang, G.; Huang, T. C.; Lin, K. P.; Giraud, P.; De Rycke, Y.; Dubray, B.; Helfre, S.; Voican, D.; Guo, L.; Rosenwald, J. C.; Keraudy, K.; Housset, M.; Touboul, E.; Cosset, J. M., Intrathoracic tumour motion estimation from CT imaging using the 3D optical flow method. *Phys Med Biol* **2004**, *49*, (17), 4147-61.
168. Mageras, G. S.; Pevsner, A.; Yorke, E. D.; Rosenzweig, K. E.; Ford, E. C.; Hertanto, A.; Larson, S. M.; Lovelock, D. M.; Erdi, Y. E.; Nehmeh, S. A.; Humm, J. L.; Ling, C. C., Measurement of lung tumor motion using respiration-correlated CT. *Int J Radiat Oncol Biol Phys* **2004**, *60*, (3), 933-41.
169. Schwartz, D. L.; Ford, E. C.; Rajendran, J.; Yueh, B.; Coltrera, M. D.; Virgin, J.; Anzai, Y.; Haynor, D.; Lewellen, B.; Mattes, D.; Kinahan, P.; Meyer, J.; Phillips, M.; Leblanc, M.; Krohn, K.; Eary, J.; Laramore, G. E., FDG-PET/CT-guided intensity modulated head and neck radiotherapy: A pilot investigation. *Head Neck* **2005**.
170. Fei, B.; Wheaton, A.; Lee, Z.; Duerk, J. L.; Wilson, D. L., Automatic MR volume registration and its evaluation for the pelvis and prostate. *Physics in Medicine and Biology* **2002**, *47*, (47), 823-838.
171. Coselmon, M. M.; Balter, J. M.; McShan, D. L.; Kessler, M. L., Mutual information based CT registration of the lung at exhale and inhale breathing states using thin-plate splines. *Med Phys* **2004**, *31*, (11), 2942-2948.
172. Schreibmann, E.; Xing, L., Image registration with auto-mapped control volumes. *Medical Physics* **2005**, submitted.
173. Koong, A. C.; Le, Q. T.; Ho, A.; Fong, B.; Fisher, G.; Cho, C.; Ford, J.; Poen, J.; Gibbs, I. C.; Mehta, V. K.; Kee, S.; Trueblood, W.; Yang, G.; Bastidas, J. A., Phase I study of stereotactic radiosurgery in patients with locally advanced pancreatic cancer. *Int J Radiat Oncol Biol Phys* **2004**, *58*, (4), 1017-21.
174. Loo, B.; Thorndyke, B.; Maxim, P.; Ho, A.; Goodman, K.; Xing, L.; Koong, A., *Determining margin for target deformation and rotation in respiratory motion-tracked stereotactic radiosurgery of pancreatic cancer*, Annual Meeting of ASTRO, Denver, CO, 2005.
175. Koong, A. C.; Le, Q. T.; Ho, A.; Fong, B.; Fisher, G.; Cho, C.; Ford, J.; Poen, J.; Gibbs, I. C.; Mehta, V. K.; Kee, S.; Trueblood, W.; Yang, G.; Bastidas, J. A., Phase II study of stereotactic radiosurgery in patients with locally advanced pancreatic cancer. *Int J Radiat Oncol Biol Phys* **2005**, in press.